Study of Contaminants in Plasmas during Decommissioning Processes

by

Nicholas SOMER

A Thesis Submitted in Partial Fulfillment
of the Requirements for the Degree of

Master's of Applied Science in Nuclear Engineering
in
The Faculty Energy Systems and Nuclear Science

University of Ontario Institute of Technology (Ontario Tech University)

Oshawa, Ontario, Canada

December 2020

Study of contaminants in plasmas during Decommissioning Processes

Submitted by Nicholas Somer

Master's of Applied Science in Nuclear Engineering

An oral defense of this thesis took place on December 21, 2020 in front of the following examining committee:

Examining Committee

Chair of Examining Committee	Dr. Jennifer McKellar
Research Supervisor	Dr. Glenn Harvel
Examining Committee Member	Dr. Ed Waller
Examining Committee Member	Dr. Brian Ikeda
External Examiner	Dr. Anatoli Chkrebtii

The above committee determined that the thesis is acceptable in form and content and that a satisfactory knowledge of the field covered by the thesis was demonstrated by the candidate during an oral examination. A signed copy of the Certificate of Approval is available from the School of Graduate and Postdoctoral Studies.

Abstract

With the intention of eventual development of on-site radionuclide capture technologies, methods to simulate radionuclide behaviour when contaminated components are subjected to plasma-based decommissioning processes are developed. Two parallel plasma systems are developed and investigated. A better-understood argon plasma based system has temperature measurement methods developed, along with an exploration of the resultant behavior when non-radioactive isotopes of cesium iodide contaminants are introduced. This plasma system produces traces of ionic species of cesium and iodide, as well as space-dependent deposition patterns: both of which are relevant towards understanding behaviour of contaminants in environments undergoing decommissioning processes. A physical simulation of a cutting process of a contaminated component is completed using an commercial plasma torch by cutting cesium iodide contaminated samples. This process produces some of the same ionic species as in the controlled experiment, proving a controlled argon plasma can be used to simulate plasma environments in decommissioning scenarios.

Keywords: Nuclear Decommissioning, Plasma, Plasma Chemistry, Decommissioning, Plasma Cutting, Radionuclide Capture, Radionuclides, Nuclear Dismantlement

Declaration of Authorship

I, Nicholas SOMER, declare that this thesis titled, "Study of Contaminants in Plasmas during Decommissioning Processes" and the work presented in it are my own. I confirm that:

- I hereby declare that this thesis consists of original work of which I have authored. This is a true copy of the thesis, including any required final revisions, as accepted by my examiners.
- I authorize the University of Ontario Institute of Technology to lend this thesis to other institutions or individuals for the purpose of scholarly research. I further authorize University of Ontario Institute of Technology to reproduce this thesis by photocopying or by other means, in total or in part, at the request of other institutions or individuals for the purpose of scholarly research. I understand that my thesis will be made electronically available to the public.

Signed:

_____

Date:

_____

Statement of Contributions

This work is supported by an OPG/UNENE/NSERC CRD grant on Nuclear Decommissioning. This work has also been supported by an NSERC Discovery Grant. Related works on this thesis have been presented or published:

- A report titled "On the Production of Argon Plasma Temperature by Microwaves" co-written with Professor Takeyoshi Sunagawa at Fukui University, Fukui Japan. Report submitted to Wakasa Wan Energy Research Center as part of a visiting student researcher program.
- Paper and presentation to the fourth *International Symposium on New Plasma and Electrical Discharge Applications; and on Dielectric Materials*, titled "Investigation of Vapour Iodine Produced by Plasma", October 7th-10th 2019, Corsica, France.
- Poster presentation to University Network of Excellence in Nuclear Engineering titled "The Characterization of Cutting Torch Plasmas for the Purposes of Radionuclide Capture during Nuclear Decommissioning", on December 16th 2019.
- Poster Presentation to University Network of Excellence in Nuclear Engineering titled "The Characterization of Cutting Torch Plasmas for the Purposes of Radionuclide Capture during Nuclear Decommissioning", on December 14th, 2020.

Dedicated to the barn cat down
the road...

"*I swear by my life and my love of it that I will never live for the sake of another man, nor ask another man to live for mine.*"

John Galt, *Atlas Shrugged*

"*God hates us and doesn't want us to know things.*"

Anonymous

Acknowledgements

The following individuals and groups are acknowledged:

- Dr. Harvel: for his endless patience, wealth of knowledge, advice, and cute cats.
- Dr. Takeyoshi Sunagawa: for his mentorship, lessons, and for being superbly accomodating during my time in Japan.
- Dr. Karthik Sankaranarayanan: for the generous donation of equipment, and his straight-shooting advice.
- Ms. Marta Kocemba: for being a wonderful friend and sounding board.
- Mr. Roger Kurmi: for being a great colleague, verbal sparring partner, and for providing sound music suggestions.
- Mr. Vajran Sarvendran for his humour and help.
- Ms. Margarita Tzivaki: for being my first friend in Ontario, for introducing me to many others...
- Mr. Haseeb Bukhari: for his assistance in fleshing out part of my literature review.
- My family and band friends for their long-distance support.

Contents

List of Figures

List of Tables

Chapter 1

Introduction

During the lifetime of a nuclear plant, leaks, spills, and other events may result in the release of radionuclides from the reactor core into the surroundings of the nuclear plant. When the plant reaches its end of operational life, decommissioning processes such as the dismantling of components often-times results in the dispersal and/or transformation of these localized contaminants into airborne ones. Many demolition tools, such as grinders and cutting torches, are used to break apart on-site material into manageable sizes for waste management, transport, and storage. These tools also produce aerosols as secondary waste. Aerosols are the primary means of contaminants to become airborne.

If a component that is being dismantled is contaminated with radionuclides, there is a risk posed to workers who are involved in the dismantling process as well as the public as aerosolized radionuclides may be easily transported by drafts and breezes. There is an additional risk of contamination of the areas where the dismantlement processes take place, which may result in additional hazards as well as material and time costs due to the additional precautions necessary when working in an environment that contains sources of radioactivity. As a result, there is interest in developing technologies that capture these aerosols as they are produced.

There are many techniques for dismantling that will produce aerosols such as gasoline-oxygen cutting, diamond saws, plasma torch cutters, and plasma arc saws. This work will consider the standard plasma torch as an example of a dismantlement technology that produces airborne releases and aerosols.

Plasma torches cut through metal due to the high temperature of the plasmas

that they produce: the plasma effectively melt through the metal due to their high temperature. These cutting processes produce airborne releases. If the metallic components are contaminated with radionuclides, there is now a radiation hazard being spread in the air. An understanding of the physical nature of the releases as they are produced is required in order to choose and/or develop technology to capture these aerosols from their source.

The purpose of this work is to understand the physical nature of the contaminants when exposed to torch plasmas. To do so, controlled and well-characterized experiments that simulate the plasmas and the cutting processes are required.

1.1 Problem Statement

Aerosol production by plasma cutting is dependent on a wide variety of parameters. This includes size and composition of the component being cut, and the characteristics of the plasma, such as its temperature and density. In addition, there is a wide array of plasma torches available on the market that have different characteristics such as the gas used, the temperature and density of the plasma, and so on. As a result, the cutting process is difficult to model directly. It is necessary to achieve the capacity to simulate and investigate these different conditions in a controlled system. The approach of this work is to attempt to simulate the plasma cutting conditions in dismantling processes. The simulation of these cutting processes would include the usage of non-radioactive equivalents of some radioisotopes that are of concern during decommissioning processes. The work in this thesis has two main themes.

1. Characterize and generate a controlled plasma which is simpler to control, understand, and model than a plasma torch. Investigate the behaviour of simulated contaminants when introduced to said plasma.

2. Simulate the cutting of contaminated components using a mock-up setup with a commercial plasma torch, and investigate the behavior of the simulated contaminants.

1.1.1 Theme #1: Microwave Plasma System

This work outlines the production of a controlled plasma using a microwave waveguide system. The waveguide system is capable of directing microwaves produced by magnetron into a column of gas contained within glass tubing. The gas is heated and ignites into a plasma. The transparency of the tube allows for spectroscopic measurements, which may be used to infer characteristics of the plasma such as its contents, temperature, and so on. There is a relatively high degree of control over the amount of microwave power delivered to the gas column. For this work, the gas used is argon. Argon is a noble gas that essentially does not form any stable chemical compounds, simplifying the process of analysis.

Non-radioactive equivalents of contaminants are added to the plasma in various forms. The contaminants react with the plasma species and produce emissions that are spectroscopically measurable. The resultant emission spectra that is produced is analyzed for contaminant presence in the plasma as atomic species. Changing the characteristics of the plasma in a precise manner, such as varying its temperature, can provide insight into what reactions occur inside the plasma as a function of its temperature. The temperature and other characteristics of the plasma and contaminants are analyzed spectroscopically.

1.1.2 Theme #2: Plasma Torch

A plasma torch is used to simulate the cutting of contaminated metallic components. The emission spectra of the torch plasma is measured using spectroscopic equipment. Its parameters such as temperature along with the spectra produced by the cutting process can be determined and subsequently compared to that of the controlled plasma in Theme # 1. Metallic components that are coated with non-radioactive chemical equivalents to the radionuclides in question can be cut with the same torch. The atomic forms the contaminants take (i.e. neutral,ionized, etc.) can then be determined using spectroscopic methods.

1.2 Objectives

1. Produce a controlled argon plasma as generated by a microwave system.
2. Characterize an uncontrolled plasma as generated by a plasma torch system.
3. Characterize the argon plasma, and explore methods of estimating its temperature.
4. Introduce non-radioactive equivalents of radionuclide contaminants into the controlled plasma and explore the resultant behaviour.
5. Explore methods of how to simulate the dismantlement of a contaminated component using an off-the-shelf plasma torch.

1.2.1 Application of Objectives to Problem Statement

The first, third, and fourth objectives have to do with producing and characterizing a controlled plasma while introducing contaminants that may be encountered during decommissioning scenarios into the plasma. These contaminants are expected to physically react with and inside the plasma. This system acts as the "control".

The second and fifth objectives address the need to obtain a more precise understanding of the plasma torch and cutting processes. They focus on the observations of the byproducts of the cutting process and measurement of the torch plasma spectrum. These objectives also focus on well as the cutting of mock-contaminated metal samples whose spectra are investigated for the presence of contaminants.

1.3 Thesis Structure

Chapter 2 begins with a literature review on relevant topics, including an overview of aerosols and physical theory behind plasma production and the measurement of plasma temperature. Chapter 3 describes the materials and methods used in this work. It also includes the procedures for the experiments performed to fulfill the

goals of this work. Chapter 4 includes the quantitative and qualitative observations made in experiments. Chapter 5 discusses the validity of the results as well as their relation to decommissioning activities and Chapter 6 provides a summary of the conclusions obtained and discusses future work.

There are several appendices included which include important information and support for the work performed in this thesis. Appendix A tabulates atomic emission line data for the identification of species and other spectroscopic methods used in this work. Appendix B describes how spectroscopic measurement data is processed to perform plasma temperature calculations. Appendix C features heat transfer calculations to ensure sufficient coolant is being supplied to the microwave systems. Appendix D outlines how the microwave power measurement components are re-calibrated.

Chapter 2

Literature Review

2.1 Introduction

This work is primarily motivated by the intent to understand the mechanisms of aerosol production during the cutting of metallic components by plasma torches in the context of nuclear decommissioning. For this to be better understood, aerosols and the radionuclides that may be contained within have to be investigated to some degree. This also necessitates an exploration of plasma physics, which describe the behaviour of plasma as well as their expected emission spectra. This overview of plasma physics will primarily focus on the types of plasmas expected to be observed in this work. The emission spectra are often used in methods which describe plasma parameters, which can be viewed to summarize plasma behaviour. These parameters, if well-characterized, may help inform how contaminant aerosols react when introduced to a plasma. An overview of emission spectroscopy will be made to justify the spectroscopic methods used to characterize the plasma that are described later on in this work.

2.2 Nuclear Decommissioning

Nuclear decommissioning is a process of removing a nuclear facility from the site and includes several stages such as fuel removal, de-watering of systems, decontamination of components, dismantling of systems, and removal of material from the site [1]. The optimization of the scope may be difficult due to lack of knowledge of contamination (type and level), the potential for the spread of

contamination, and the generation of secondary wastes as part of the processes used [2]. These issues lead to concerns over whether a component should be decontaminated before or after dismantlement or disposed of as is. This is partially due to decisions being made based on clearance level regulations [2]. Ultimately, radioactive materials must be disposed of away or at the site in a manner that is safe to the environment and that is approved of by the public. Many parts of nuclear plants, especially those that interact closely with the reactor core, are likely to be contaminated with radioactive compounds: fission products and neutron activation products. Fission products may be transported by the coolant and deposited into other regions of the heat transport system in the case of fuel failure. Even after a core has been de-fueled and drained of its coolant, some radioactive isotopes may remain. When dismantlement of these components takes place, there is a hazard for those involved in the work, and an inherent probability of spreading radionuclides due to the aerosolization and breakdown of solid waste. This hazard is generally a function of the dismantlement processes, how long they take to complete, as well as the type, location, and concentration of radionuclides. All radioactive work is regulated with the intent of minimizing dose to the worker, public, and the environment. The additional protections that are required are often cumbersome and interfere with the flow of work. For instance, additional personal protective equipment may have to be worn, special work areas may be required, and so on. This section provides an overview of nuclear dismantlement, of aerosol behaviour, and of radionuclides that are of interest specifically to the Pickering Nuclear Generation Station in Ontario, Canada.

2.2.1 Nuclear Dismantlement

The dismantlement process of nuclear sites is one step of many in the decommissioning process. It involves the planned safe deconstruction of site components until the desired end-state is achieved. Many of the components and the sites' foundations consist of multiple material types, such as metals, composites, and fluids. The metals and composites oftentimes have to be cut into pieces for easier disposal. In the process of breaking down these materials,

secondary waste may be released in the form of aerosols or smaller solids [3]. The characteristics of this waste depends on the types of dismantlement techniques, which are discussed later in this section. If this material is contaminated, the radionuclides may be atomized and/or released into the air in the form of aerosols [4]. These aerosols may come in various forms. One method of component dismantlement, plasma cutting, consists of cutting metal using a plasma at high temperatures. These high temperatures can generate aerosols by melting and vaporizing metal, but the aerosol characteristics as a function of the plasma characteristics are not well-understood. Different filtration (capture) techniques may be used depending on the characteristics of these aerosols, and would be dependent on their characteristics such as their size and speed.

2.2.2 Overview of Dismantlement Techniques

There is a wide array of dismantlement technologies available. Two families of technologies are mechanical and thermal dismantlement techniques. Examples of mechanical techniques include saws, drills, and shavers. These can break apart solids such as concrete (and metal in some cases) which can allow for their removal and transportation to a waste storage site [3, 5, 6]. Thermal techniques consist of flame and plasma cutting techniques [3]. These technologies are primarily used with the cutting of metal, where the high temperature of the plasmas or flames produced can cut the metal. These include plasma torches, arc saws, and oxygen burners [6].Some of these processes have advantages over others. These advantages are based on measurements of dismantlement rates, the costs, and the production of secondary waste [6]. Whether the techniques are performed under water or in open air, sludges, dusts and even contaminated water is to be expected as secondary waste [3, 6]. Boing notes that plasma-based cutting techniques can be as much as fifty times faster than mechanical means for cutting metal components, but that they tend to spread contamination [3].

One of the major sources of costs found in dismantlement processes are the secondary wastes that are produced [3]. Plasma torches are one technology that produce secondary wastes: they cut metals at a relatively high speed but produce particulates and aerosols [3]. This fact once again points to the need for effectively

capturing these particulates at the source. It is also noted that the testing of plasma torch dismantlement may also clog certain kinds of filters. A study confirming this type of phenomenon will be reviewed in a later section.

Decontamination

As an aside, decontamination technologies are used to reduce the level of activity in waste or in an environment.[7] They are one means used to protect workers from receiving a dose, by clearing the working environment of radioactive contaminants before, after, and while dismantlement operations take place[7]. Dismantlement technologies that produce aerosols such as plasma cutters may spread contamination, furthering need for more decontamination efforts. Decontamination technology may prove costly, and may be unnecessary if the spread of radioactive materials is minimized. It is the intent of this work to help minimize the need of additional decontamination efforts by working towards capturing the aerosols (which contain radionuclides) as they are produced rather than as they spread. As Mr. Boing suggests, it's desirable to keep the dismantlement processes "simple" [3].

2.2.3 Sources of Radionuclide Isotopes of Interest in Nuclear Decomissioning

The radionuclides of interest in nuclear decommissioning processes that are contained within components come to be from two mechanisms: fission products and neuron activation.

Fission Products

Nuclear fission leads to a wide array of radioisotopes, which are referred to as fission products. Many of these fission products are radioactive with long lifetimes. Under ideal operating circumstances, these fission products will be kept in the fuel, lest a fuel failure occurs. In that case, leakage of fission products may spread into other systems. Spills and leaks, and fuel failure may subsequently spread these fission products into other areas of a nuclear reactor site [8].

Neutron Activation

Neutron activation is a process in which a nucleus of an atom captures a neutron through bombardment, and subsequently transitions to an excited atomic state as the nucleus becomes more massive. The neutron bombardment of an atom in a component may be transmuted into an unstable isotope, which will eventually decay radioactively. Primary parts of a nuclear reactor facility that contain the neutron activated radionuclide inventory are in the structures that surround a reactor core. The core peripheries and the biological shield both contain metals and concrete, which will be bombarded with neutrons over the life of the reactor as fission reactions take place [8]. Over time, there will be a buildup of neutron activation products, some of which may remain past of life of the plant due to their long half-lives. These activation products will then be released into the air as the components are dismantled by some means.

Table of Radionuclides of Interest

This section outlines the radionuclides that are important to the Canadian nuclear industry in decommissioning scenarios. A table of such radionuclides are displayed in Table 2.1. They are either produced via neutron activation, or are a fission product. The decay emission types are also listed, but the decay type does not have an effect on the scope of this work. This table was constructed as a product of private correspondence with the Ontario Power Generation Decommissioning team [9]. For the purposes of this work, two isotopes are chosen. They are highlighted in the table. The first isotope is iodine-129. It beta decays into xenon-129 with a half-life of 15.7 million years [10]. Iodine is generally chemically active, and tends to spread: reacting or depositing on many surfaces that it encounters. Iodine-129 is a common fission product. Cesium 137 is another common fission product. It beta decays with a half life of 30.17 years. Its daughter isotope, barium-137m emits gamma rays with a half life of 2.66 minutes [10]. Iodine and cesium are also both volatile chemical elements. As a result, cesium is another isotope of concern because its spread in aerosols. Another fact to keep in mind about cesium is that it is a heavy metal. Regardless of its radioactivity, is also a non-radioactive hazard.

TABLE 2.1: Table of select radionuclides relevant to nuclear decommissioning for Ontario Power Generation. Half-lives taken from [10].

Radionuclides	Emission Type	Half-Life (years)
Radionuclides with percent contribution > 0.05%		
C-14	β	$5.7 * 10^3$
Fe-55	x, EC	$2.6 * 10^0$
Ni-59	x	$8.0 * 10^4$
Co-60	γ	$5.3 * 10^0$
Ni-63	β	$9.2 * 10^1$
Zr-93	β	$1.5 * 10^6$
Nb-94	γ	$2.0 * 10^4$
Radionuclides with percent contribution < 0.05% and total activity greater than release criteria		
H-3	β	$1.2 * 10^1$
Cl-36	β	$3.0 * 10^5$
Ca-41	e, x	$1.3 * 10^5$
Sr-90	β	$2.9 * 10^1$
Nb-93m	x, γ	$1.4 * 10^1$
Tc-99	β	$2.1 * 10^5$
Sn-121m	β, x	$5.0 * 10^1$
Sb-125	γ	$2.8 * 10^0$
Te-125m	x, γ	$2.8 * 10^0$
I-129	β	$1.6 * 10^7$
Cs-137	β, γ	$3.0 * 10^1$
Eu-152	γ	$1.4 * 10^1$
Eu-154	γ	$8.6 * 10^0$
Pu-238	α	$9.9 * 10^1$
Pu-239	α	$6.6 * 10^3$
Pu-240	α	$6.6 * 10^3$
Pu-241	α	$1.4 * 10^1$
Am-241	α, γ	$4.3 * 10^2$
Cm-244	α	$1.8 * 10^1$

2.3 Aerosols

Aerosols are generally defined as suspended solid and liquid particulates in air [11, 12]. The particulate size is typically given as a bound on the order of 1 nm to 100 µm [11]. Aerosols often come in various size distributions. This is dependent on the process used to produce them [13].

2.3.1 Aerosols Produced in Nuclear Decommissioning

Aerosols produced in a nuclear site are a concern because they are potentially a radiological risk to workers and the public. This is primarily due to their ability to travel over large distances (suspended in air) and for their inhalability [2, 4]. These aerosols that may be contaminated can spread throughout the areas where the dismantlement takes place, causing further contamination of surfaces, equipment, workers, and possibly the environment [2, 4]. If the aerosols are contaminated, the they can carry radionuclides into the respiratory system of workers if inhaled. As discussed earlier, the spread may also vary based on the dismantlement method that produced them.

The spread of contaminants in plasma cutting processes is illustrated in Figure 2.1. The contaminated component is cut and is a source of radionuclides that spread through the air. They spread onto the floor and may spread towards other components.

Chae et al. [14] provide a thorough overview of the radioisotopes that may be spread in cutting processes. They also discuss the effects of cutting different metal material types, as they will have an effect on the behaviour of the spread which occurs during dismantlement processes . They also discuss the differences in aerosol production for several types of cutting technologies, including laser cutting, metal grinding, and plasma cutting [14].

Radioactive Aerosols produced by Plasma Cutting

It is known that plasma cutting of radioactive components such as piping can produce aerosols [4]. Shimada et. al. [4] investigated the levels of radioactivity in

aerosols produced by the cutting of contaminated pipes from the Japanese Power Demonstration Reactor (Tokai, Japan) and FUGEN (Tsuruga, Japan) reactor [4].

The pipe from the FUGEN reactor was a carbon steel pipe section taken from their liquid waste treatment system. It is featured in Figure 2.2. Note the corroded inner surface of the pipe.

The pipe's internal surface was internally contaminated. The contamination had a surface concentration with a range from 550 to 55000 $\frac{Bq}{cm^2}$ of cobalt-60. When cut with a torch (unspecified make), the particulates produced were captured and characterized as a function of their size and radioactivity [4]. Figure 2.3 features two distribution plots. The first characterizes the distribution of radioactivity to each bin of aerosol particle size. The second characterizes the specific radioactivity in Becquerels per gram. To summarize, the 2 µm particulates generally carried more radioactive cobalt, but not as high in concentration as the smaller diameter aerosols. The smaller diameter aerosols contained the highest concentrations of Cobalt species. The line of fit specifies the specific radioactivity of the aerosol particulate as a function of inner diameter [4].

2.3.2 Overview of Aerosol Filtration Techniques

Aerosols, depending on their size, can be captured using different types of filters. There is a body of research on the capture of aerosols generated during nuclear dismantlement processes such as plasma cutting. Common filters used in homes, buildings, etc. have been investigated for their possible application to capture aerosols produced in nuclear dismantlement processes. A more standard of filter includes the High Efficiency Particulate Air (HEPA) filters. These filters follow a standard that requires capture efficiencies down to 0.3 µm.

It is known that filtration systems such as HEPA filters may not suffice, due to the fact that the products of plasma cutting may interfere with the filters' abilities to continuously capture particulates. Lee et al. [15] studied various aspects of HEPA filters that may interfere with decommissioning work. They study the degradation of filter efficiency in a HEPA filter as a stainless steel sample is cut with a plasma torch inside an enclosed apparatus.

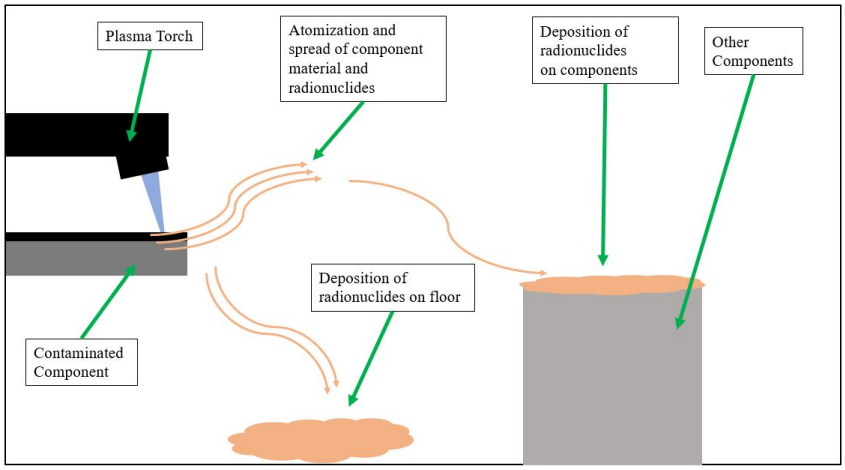

FIGURE 2.1: Sketch of contaminant spread from contaminated component to ground and other components.

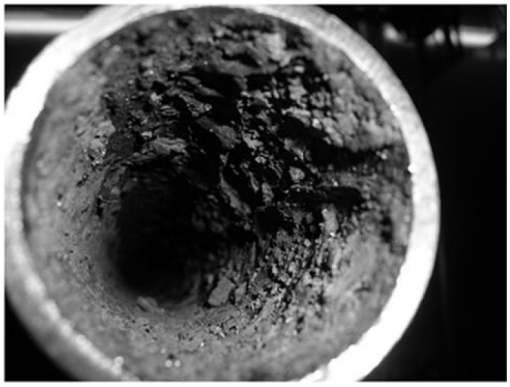

FIGURE 2.2: Contaminated Pipe from FUGEN reactor [4].

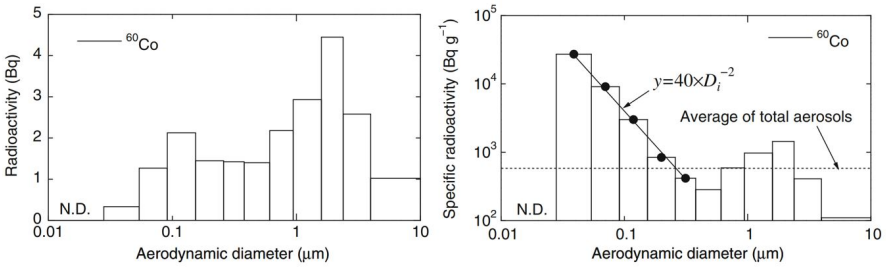

FIGURE 2.3: Plots of radioactivity and specific radioactivity distributions. Modified from Shimada et al. [4].

The aerosols and vapours produced by these cuts were captured by a HEPA filter, which was not replaced for the entire course of the experiments. Multiple cuts were made, and the capture efficiency of the filter was measured [15]. The results of this experiment are shown in Figure 2.4. In this figure, each cut of a 3 cm section counts as a unit of "Filtration Time". It is noted that filter efficiency drops in the 1 µm particulate diameter range as more cuts are performed. HEPA filters, as they are clogged, will eventually allow less air to flow through them [16]. This essentially reduces their ability to function as specified.

Characterization Efforts towards the Capture of Iodine Aerosols

There are research efforts that seek to obtain more precise understanding of the behaviour of iodine aerosols during plasma cutting scenarios. Harvel et al. produced some novel and foundational work, on which this thesis is based, where a microwave-based plasma is produced, and vaporizes iodine in the process [17]. They were able to trap and identify multiple chemical forms of iodine in a paper filter. The microwave plasma system setup used in this thesis is derived from their paper. This thesis acts as a continuation of this work.

2.4 Plasmas

Plasmas are generally described as a fluid mix of electrons, one or more gaseous elements, and their equivalent ionic species [18, 19]. Plasmas exist in a wide array of environments and temperatures, from high pressures in the cores of stars to neon lights [19]. While there is not a necessarily rigid definition of plasmas, there are many similar descriptions. They exhibit various properties that are not common in gases, such as the internal screening of electric fields and collective response when subjected to electromagnetic fields [18, 19]. They also have a degree of opacity to light, and generally are not at thermodynamic equilibrium [18, 19].

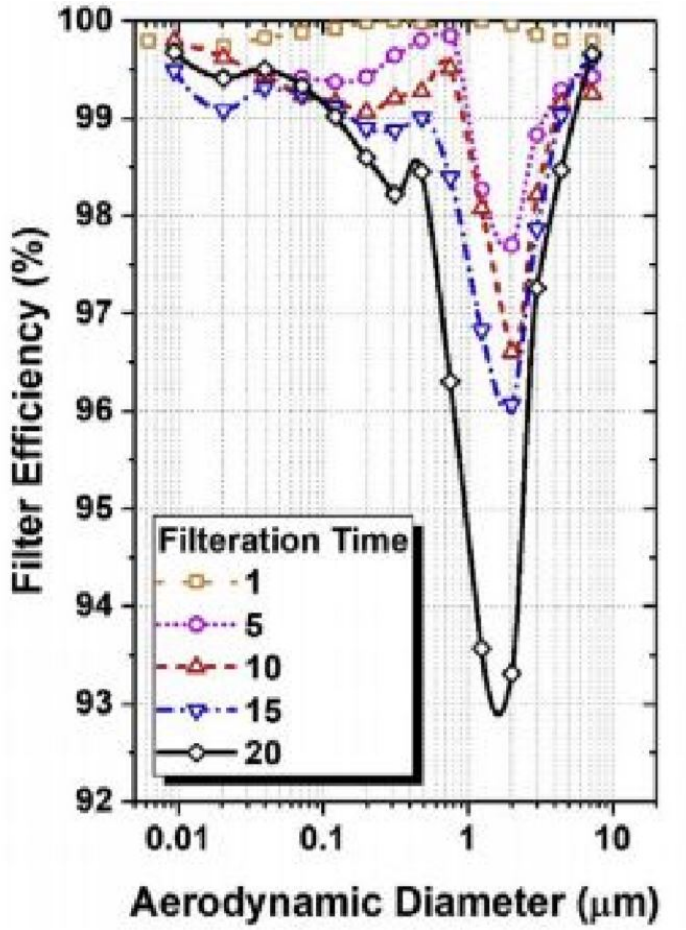

FIGURE 2.4: Plot denoting the drop of HEPA efficiency for each subsequent cut using plasma torch. Taken from [15].

While the methods of modelling plasma will not be explored in depth, a description of them will be used to give context to the different behaviours that may be seen in this work. The physics of plasmas can often be characterized with certain parameters [19]. The parameters of interest for this work that will be discussed are the densities of atoms, electrons and excited states, as well as their respective temperatures.

Other parameters that inform the behaviour of plasmas will also be discussed: the Debye length, the plasma's degree of ionization, and the mean free paths of the contained species.

The literature showcases a wide range of applications for plasmas. They include, but are not limited to: the cutting of material, metal sputtering, and waste processing. These applications will be briefly outlined in this work as they are important to this project. The reactions of the plasma and materials that occur in these applications are expected to be seen to some extent in the experiments described in this work. For similar reasons, if investigated further, the modeling used to improve these processes also provide direction in how to develop aerosol capture technology. A general view of processes that form plasmas are those that involve the liberation or introduction of electrons into the gas through some means, and where the gas' species are ionized. The resultant collection of positive and negative charges effectively allow the plasma to behave as a collective unit (such as a fluid) when influenced by electromagnetic fields. Typically a configuration that produces large constant or varying electric fields or potentials that drive ionization in a gas is used to produce plasmas [20].

2.4.1 Plasma Parameters

As a result of the physical models and observations made, the types of plasma that are observed can often be expressed by various parameters that include, but are not limited to the temperature of the plasma's constituents, as well as their concentration or density [18]. This section will first discuss temperature and density values of species within a single-species plasma [18]. They act as fundamental parameters from which many others can be derived. The values of the parameters also allow to verify if the treatment of the subject as a plasma is valid [18]. The

section will use a hypothetical species A as part of the descriptions, which can be have multiple ionizations. In a single species plasma, the constituent species will consist of the neutral gas atom A, its positive and negative ions, and free electrons e.

Temperature

The knowledge of the temperatures of the plasma species (electrons, ions, neutral atoms) in plasmas is important, as they, with their densities, often inform the internal dynamics of the plasma. From a chemical kinetics point of view, they, to some extent, also inform the types of chemical reactions the plasma constituents participate in and at what rate. The latter especially applies to the temperature of the ions. Unlike in an ideal gas, electron temperatures often do not vary with system pressure in a monotonic manner. An example of this is seen in Kaneda et al., where electron temperature decreases with gas pressure [21]. Often-times the temperatures of plasma constituents are assumed to be the same. This is referred to as Local Thermodyamic Equilibrium (LTE) or the description of "thermal" [18]. While the temperature profile of the plasma may vary with space, the plasma species as a function of space, or at least at the same local region, would have equal temperatures under the LTE assumption. The treatment of LTE assumes that the plasma has existed long enough for enough inter-molecular collisions between ions, electrons and neutrals to for the kinetic energy distribution to become Maxwellian [22]. This may not always be the case. In cases, such as arc plasmas, the assumption being valid is dependent on the system and method with which they are generated. Additionally, these plasmas may be thermal in some regions, and not in others once again due to the physical processes by which they are generated. Fluorescent lamps, as it will be seen later in this section, have multiple different regions that may be treated as a plasma, but do not have the same resultant behavior. As the applications of plasmas often are based on the temperature of the ions, the assumption of LTE can allow for the equating of ion temperature with electron temperature, simplifying many physical models. It is worth noting that a plasma having a non-Maxwellian kinetic energy distribution and a Maxwellian one each having the same (effective)

temperature may result in different behaviour and applications. It is generally not assumed that plasmas are in the LTE state due to many physical effects [19]. These effects include but are not limited to how the the plasma produced, interactions with the container, and the thermalizing or moderating effects of collisions with atoms by electrons. In many plasmas, the assumption of LTE may not be possible. Arc and spark discharges are often not treated as thermal. Additionally, the usage of plasmas in an industrial setting, such as the cutting of material with a plasma torch, can create aerosols that mix into the plasma, effectively creating a dusty plasma. These plasmas may not be necessarily considered to be in LTE as dust, ion, and electron temperatures can often vary from each other by many orders of magnitude [23]. Dusty plasmas will be discussed later in this chapter, but are not subject to thorough study for the purposes of this thesis. The exploration of these types of plasmas helps inform some of the behaviour that may be observed later in this work.

Density

The densities of species in plasmas are typically expressed as a number density, because mass and charge densities are simple to recover from this value.[19] Densities of all species are taken into account: those of the neutral plasma gas, its excited states, its ions, and the free electron density. Assumptions may be made about about higher ionization states, such as setting those concentrations to zero if temperature is sufficiently low [19]. Densities, like temperatures, can vary with space in a plasma. Assumptions are often made about the densities of constituents, such as setting them to zero in the case of high ionization states of colder plasmas. As it will be seen in applications such as chemical reactions within plasmas, the concentrations of certain species will have larger contributions than others. Densities of plasmas may vary by many orders of magnitude, from $1 \times 10^4\,\mathrm{m}^{-3}$ in the magnetosphere to the $1 \times 10^{31}\,\mathrm{m}^{-3}$ in inertial fusion [18, 19].

Debye Length

The Debye length is one way of describing the shielding of a charge induced electric field in a plasma [19]. The Debye length describes the rate at which an electric potential attenuates over distance inside a plasma. The potential decays over distance faster than the $\frac{1}{r}$-dependence of Coulomb potential. This is due to the shielding effects of positive and negative charges that surround the charge. This modified potential is also referred to as the Yukawa potential $V(r)$ [19]. It is defined as the following:

$$V(r) = \frac{Q}{4\pi\epsilon_0 r} \exp\left(-\frac{r}{\lambda_D}\right) \tag{2.1}$$

Q is the charge that produces the potential, r is the absolute distance from the charge, and ϵ_0 is the permittivity of free space. The Debye length is defined as the decay term in the exponential: λ_D. For a single charged species j inside a plasma, the Debye length that it contributes is expressed in the following equation:

$$\lambda_j^2 = \sqrt{\frac{\epsilon_0 k_B T_j}{n_j {q_j}^2}} \tag{2.2}$$

where q_j is the charge of the species, k_B is the Boltzmann constant, T_j is its temperature (if different species have different temperatures) and n_j is the number density of the species. The total debye length λ_D of a plasma, formed by a mix of charged species, can be extracted from the following equation:

$$\frac{1}{\lambda_D^2} = \sum_{species j} \frac{1}{\lambda_j^2} \tag{2.3}$$

From this, it can be inferred that Debye length contributions from each ionized species that are small dominate the total Debye length overall. The Debye length can vary from the scale of angstroms in the case of implosion fusion, to hundreds of metres in the magnetosphere. Figure 2.5 compares the Coulomb potential with the Yukawa potential with a Debye Length of $\lambda_D = 1\,\mathrm{m}$ for a test charge of $Q = 4\pi\epsilon_0$, to cancel out the leading constants. The logarithmic scale demonstrates how the screening of the electric potential occurs over distance.

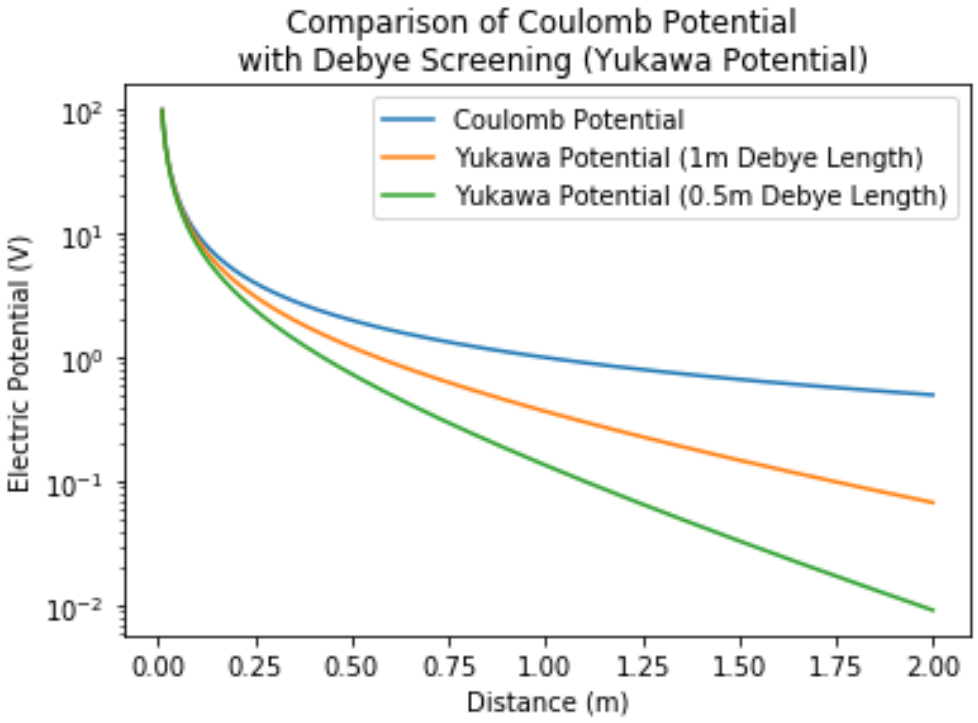

FIGURE 2.5: Plot comparing the Coulomb potential and Yukawa potential for a given Debye Length. The Coulomb potential decays over distance slower than any Yukawa potential.

The Debye length can also be used to verify that the treatment of an object as a single species plasma is correct. There are two conditions that should be true for the plasma description of plasma to be valid. The first is to require that the Debye length is much less than the scale L of the plasma:

$$\lambda_D < L \tag{2.4}$$

If the Debye length was greater than or equal to the scale of the plasma, the expected behavior would be more like that of a gas, and therefore a plasma treatment would not be consistent [18]. The second condition is that the collection of particles around the test charge is very large. This is typically expressed by counting the number of species located in a cube with Debye length width:

$$n{\lambda_D}^3 > 1 \tag{2.5}$$

where n is total number density of the plasma. A number less than one would contradict the assumption that enough charges are present to screen electric fields. A larger value indicates a smaller number of collisions in the plasma, which is to say that it is near collision-less, as [18]. The Debye length is an important parameter in plasmas, due to the fact that it allows one to gauge whether a plasma treatment is valid or not, and acts to predict the behavior observed within the plasmas.

Degree of Ionization

The degree of ionization in a plasma is measured as the ratio of ion species densities n_j to the total density n of the plasma, denoted by α:

$$\alpha = \frac{\sum_{ionsj} n_j}{n}. \tag{2.6}$$

The degree of ionization varies from the makeup of the plasma gas and is dependent on many factors including the method by which it is generated. It can be shown, using statistical mechanics arguments, that α generally rises with temperature [22]. The degree of ionization indirectly indicates the types of collisions that dominate.

In a highly ionized plasma where α is large, Coulomb-force interactions dominate as there are many charges. Conversely, for a partially ionized plasma, collisions with neutrals dominate.

Plasmas can have a low value of α, but with no agreed-upon lower limit in the literature. The degree of ionization's value can be unity in fusion confinement plasmas. A degree of ionization of zero would effectively imply that the system does not merit the plasma treatment, as some amount of ionization is required for the physical models to be consistent [18]. The degree of ionization in plasmas is important to some extent as it should indirectly inform certain aspects of the plasma such as its temperature, and types of reactions that can take place within it. For instance, charged particles will interact differently with ionic plasma species than with neutral ones.

Mean Free Path

The mean free path l_{mfp} of a species within a plasma is the average distance it travels between collisions. The value can vary from species to species within the plasma, as it also depends on the species' physical size and mass. As a rule of thumb, if the mean free path of particles within the plasma is on the order of its scale L or larger, the plasma can be described as being near collision-less [18].

For a sense of scale, the mean free path for inertial fusion plasmas is on the order of 1×10^{-7} m whereas the plasma in the magnetosphere is effectively collision-less with a mean free path on the order of 1×10^{14} m where essentially no collisions take place [18].

The mean free path is an important parameter to keep in mind for the plasmas produced in this work. Large numbers of collisions are required in order for a fluid (liquid, gas, plasma) to attain thermodynamic equilibrium. Additionally, from a reaction standpoint standpoint, more reactions may occur inside a plasma if more collisions take place due to a smaller mean free path.

Table of parameters

Table 2.2 summarizes some plasma parameters for various types of plasmas seen in the literature. These are to be taken as order of magnitude values rather than

exact values. An estimate of scale is included for reference.

TABLE 2.2: Table of plasma parameters for various types, primarily taken from Bellan [18] and Beuthe [20].

Symbols	n	T	λ_D	$n{\lambda_D}^3$	l_{mfp}	L
Units	m^{-3}	K	m	unitless	m	m
Solar Corona	10^{15}	10^{6}	10^{-3}	10^{7}	10^{5}	10^{8}
Solar Wind	10^{7}	10^{5}	10^{0}	10^{9}	10^{11}	10^{11}
Magnetosphere	10^{4}	10^{5}	10^{2}	10^{11}	10^{14}	10^{8}
Ionosphere	10^{11}	10^{3}	10^{-2}	10^{4}	10^{3}	10^{5}
Mag. Fusion	10^{20}	10^{8}	10^{-4}	10^{7}	10^{4}	10^{0}
Inertial Fusion	10^{31}	10^{8}	10^{-10}	10^{2}	10^{-7}	10^{-5}
Dense Bench Plasma	10^{20}	10^{4}	10^{-6}	10^{3}	10^{-2}	10^{-1}
Diffuse Bench Plasma	10^{16}	10^{4}	10^{-4}	10^{5}	10^{1}	10^{-1}

As can be seen, the parameters of plasmas can vary by several orders of magnitude. These plasmas are known to have different behaviors, and yet still have a valid plasma treatment.

2.4.2 Plasma Regimes

As discussed in the parameters section, plasmas encountered in nature and in the laboratory often behave differently from each other, even though they are all treated under the same descriptive term. In some sense, plasmas exist in regimes, which are dictated by the conditions by which they are produced and as their physical parameters. The introduction of additional gas species (a "multi-species plasma"), or small solids in the form of dust (dusty plasmas) may radically change the observed behaviour. This section is devoted to outlining the regimes of plasma that are expected to be encountered through the course of this work.

Arc Plasmas

Arc plasmas are produced by an electric arc in gas. This occurs due to dielectric breakdown. Dielectric breakdown of the gas occurs when an applied voltage

difference overcomes the dielectric strength of the gas, where then the resistance rapidly drops in value. The electrons emitted by the cathode are rapidly accelerated towards the anode and then transfer kinetic energy to the gaseous atoms or molecules. These transfers of energy cause excitation and ionization reactions, generating the glow seen in the region of the arc when recombination and de-excitation reactions occur [20]. Arcs can be generated with DC, AC or transient signals, such as pulses. Arc plasmas often are referred to based on their currents and voltage drops caused by the current. The voltage drops are dependent on the excitation mechanisms. The electric arc currents through the plasmas have been described to have a lower limit on the order of 0.1 A , and currents have been observed as high as 10000 A [20]. The wide range of currents are due to changes in the plasma's resistivity with applied voltage. Some of these plasmas are described to have a negative "differential resistance" where a rise in applied voltage lowers the net resistance, allowing it to conduct more current [24].

Arc plasma torches are an example of arc plasmas. They cut metal by producing an arc between the cathode on the torch head and the grounded metal while pumping compressed gas such as air to supply the plasma gas [20]. Figure 2.6 is a sketch of the process that takes place.

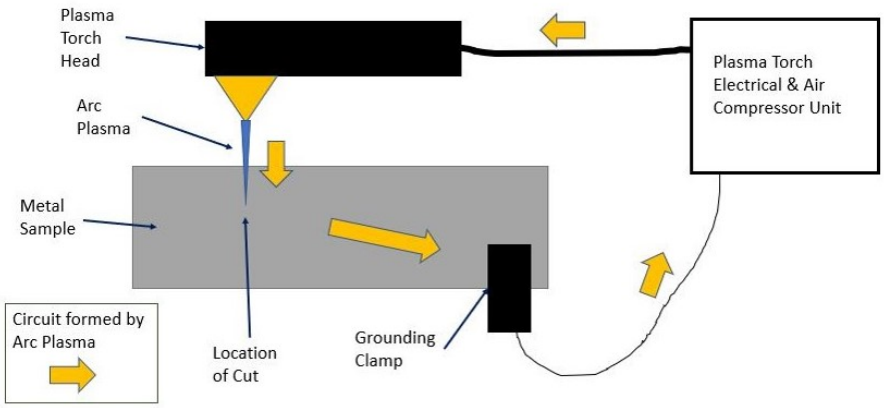

FIGURE 2.6: Schematic of plasma generated by arc plasma torches.

A large voltage is applied between the plasma torch nozzle and the metal sample that is being cut. The circuit to the ground is completed using a grounding clamp.

The current that flows through the compressed air heats up the atoms through collisions. The plasma torch used in this work outputs a current on the order of 20 A, at an imput voltage of 90 V [25].

Jet Plasmas

Plasma jets are arc plasmas where the ionization region is extended by steady gas flow between the electrodes, pushing the arc with the direction of the flow. Some plasma torches and microwave plasma systems can be classified as jet plasmas. Electrode configurations may vary, as well as signal types that are used to ionize the gas. Jets may be produced using DC voltage, or by employing a high voltage RF or microwave signal. AC signals may not require direct electrode contact with the gas [20]. Contact-less plasma jets allow for higher electrode durability than their direct current counterparts. The plasma generated in this work could be considered a conntact-less plasma jet.

Multi-Species Plasmas

Multi-Species plasmas can take the same forms of the aforementioned plasmas, but now consist of many gaseous species. Air plasma torches are an example where there is a mix of ions, neutrals, and molecular forms of oxygen, nitrogen, argon, and so on. The behaviour of multi-species plasmas are more complicated to model and typically require statistical modeling techniques. Multi-species plasmas are often a subject of research. For instance, Mizeracyk et. al [26] introduce a dilute concentration of water vapour into an argon plasma column allowing them to estimate the argon plasma's temperature by calculating the temperature of the hydrogen and hydroxide radicals (OH-) using spectroscopic techniques.

Dusty Plasmas

The introduction of large-sized particles or grains may shift a plasma to a state where the expected behaviour may differ than pure plasmas. Dusty plasmas distinguish themselves from single and multi-species gas plasmas by the presence of relatively large dust grains in the plasma. The scale of the grains is on the

order of $0.1 - 10\mu m$ [23]. It is noted here that this dust size falls within the definition of aerosols employed previously. The dust grains experience drag forces, and typically undergo a far stronger force of gravity than individual ion atoms. Gravity is often included in the modeling of dusty plasmas, especially in astrophysical models [23]. The behavior of the spokes on Saturn's rings, for instance, were explained in part by a dusty plasma model while taking into account their orbit around the planet along with its magnetic field. The behaviour in dusty plasmas is often more complicated to model in comparison to single-species plasmas. New parameters are often introduced which allow for some modeling techniques. They are a function of the size, composition and density of dust grains. The large dust particulates present in a dusty plasma typically act as a charge and electron sink. The size and surface area of dust grains changes the collision mechanics and temperature distributions in dusty plasmas. Dusty plasmas are rarely in LTE and often have electron temperatures that are higher than those of the dust or ions. Dust grains, with their lower mobility, are slower to respond to changes in electric fields and magnetic fields. In some experiments, acoustic waves and crystallization phenomena that are not seen in single or multi-species gas plasmas have been observed in dusty plasmas [23].

2.4.3 Overview of Plasma Applications

The applications for plasmas discussed in this section outline types of behaviour that will be observed throughout this thesis' experiments. The section begins with a brief overview of glow discharge lamps, and then discusses plasma reactors, applications for metal sputtering and deposition, and plasma torches.

Gas Discharge Lamps

Gas discharge lamps are encountered in everyday life. They are often used in room lighting and neon signs due to their brightness and energy effciency. One such type of lamp is shown in Figure 2.7. A schematic has been added to help identify the regions of interest. There are several types of plasmas formed in this lamp. This is due to electrons traveling from the cathode towards the anode. The "negative

glow" region is caused by dense, slow electrons being emitted by the cathode [27, 28]. The electrons gradually gain speed and become less dense, and travel through a region of the lamp where not many interactions occur. This is the Faraday Dark Space. The electric field gradually increases due to there being fewer ions present, and accelerates the electrons to a higher velocity, colliding with the atoms. The atoms become excited due to energy being imparted to them from the collisions, and de-excite, emitting light. This is referred to as the "positive column". The "anode glow" is created by the strong electric field present at the anode which induces additional excitation reactions [27, 28].

Plasma Reactors

Plasma reactors use the typically high temperature of constituents of plasmas, including the ions and stray electrons, to chemically transform compounds introduced into them [29]. An example of a plasma reactor is featured in Figure 2.8. It produces an argon plasma which is used to decompose carbon dioxide into carbon monoxide [30]. The argon plasma is produced by heating argon gas with microwaves. The chemical reactions take place inside the plasma region outlined by the right panel of the figure.

For this work, the radionuclide and metal compounds that enter the plasma formed by the torch or microwave system may react to form other compounds, or they may decompose. This is dependent on the internal behavior of the plasmas themselves and will likely be a function of their descriptive parameters. Recall that one of the goals of this work is to simulate the internal behavior of the contaminants in the torch's plasma during cuts by the controlled experiment: the argon plasma. The research in plasma reactors, in the long run, may help model, build, and research these plasmas.

Metal Sputtering

Plasmas are often employed in the process of metal sputtering where the plasma is used to deposit thin films of material on a surface. The plasma often acts to vaporize and charge the material where it hits the target surface [31].

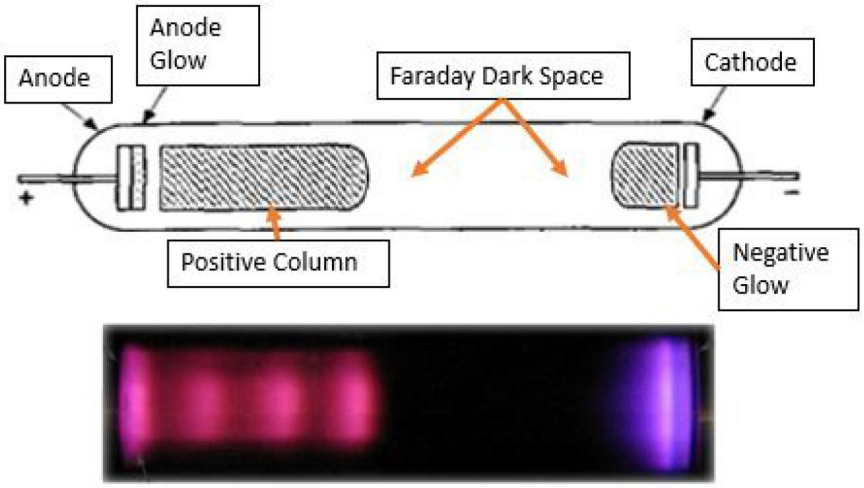

FIGURE 2.7: Schematic and image of gas discharge lamp with labeled glow regions. Modified from [27, 28].

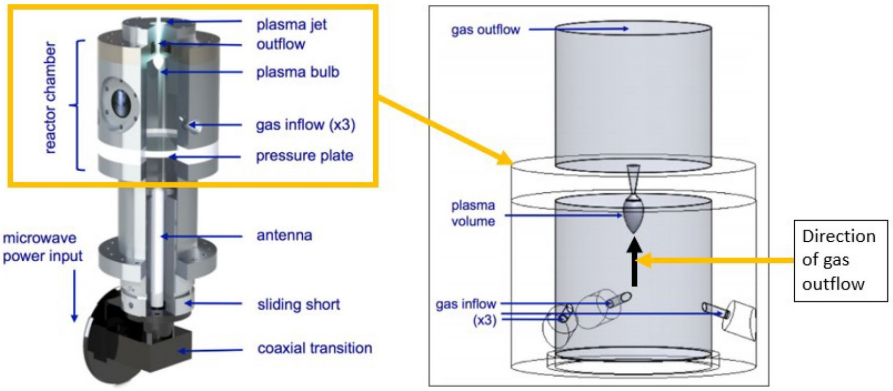

FIGURE 2.8: Image of plasma reactor and schematic of its reaction region [30].

The vaporization of contaminated metal in decommissioning senarios during during plasma cutting may create deposition patterns. These deposition patterns are often exploited in metal sputtering applications. This knowledge may be useful to future research in the development of aerosol capture technologies.

Figure 2.9 shows a plasma sputtering system along with a schematic. An argon plasma is produced by applying a sinusoidal voltage across a carbon rod electrode and the target object [31]. The argon plasma atomizes parts of the carbon rod, and induces deposition onto the surface of the substrate. This method of deposition is a means to produce thin coatings on the substrate surface that many other methods may not be able to achieve.

Plasma Torches

As mentioned in a previous section, plasma torches are used to cut metal at high speeds, typically through the formation of plasma arcs. They often do not require a gas supply, as many can run off of internal air compressors and use air as the plasma gas. The plasmas formed by these torches can have a temperature in the thousands of Kelvins, which can melt many metals [20, 32]. One figure provided by Beuthe has one plasma torch in the $1300K$ range [20]. Figure 2.10 provides a schematic and image of how a plasma torch projects the electric arc through air onto the work piece, cutting it. The plasma torch used in this work functions using this principle: electrons are accelerated at a high speed from an electrode through compressed air (or gas). The electrons impart momentum and energy to the molecules and atoms in the air [20].

2.5 Overview of Emission Spectroscopy

Spectroscopic methods are employed to explore the behavior of the the plasmas investigated in this work. These methods use the characteristics of emission line shapes and intensities to calculate temperatures, determine the type of species present in the plasma, and so on. The physics behind emission lines will not be discussed in depth in this section.

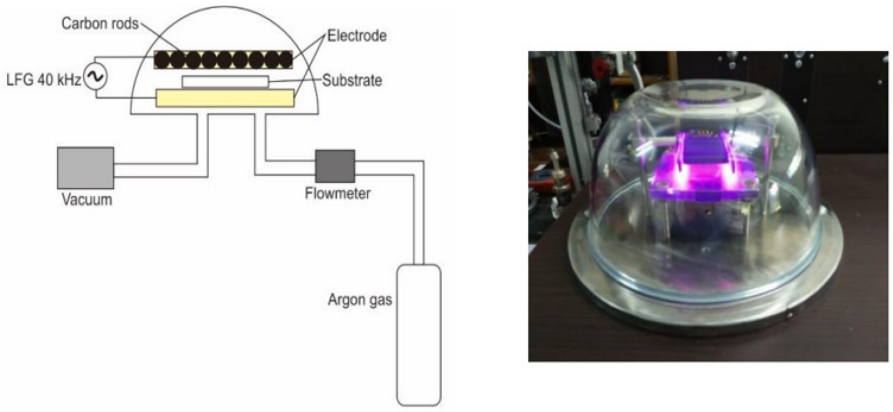

FIGURE 2.9: Schematic and image of plasma sputtering setup. Modified from [31].

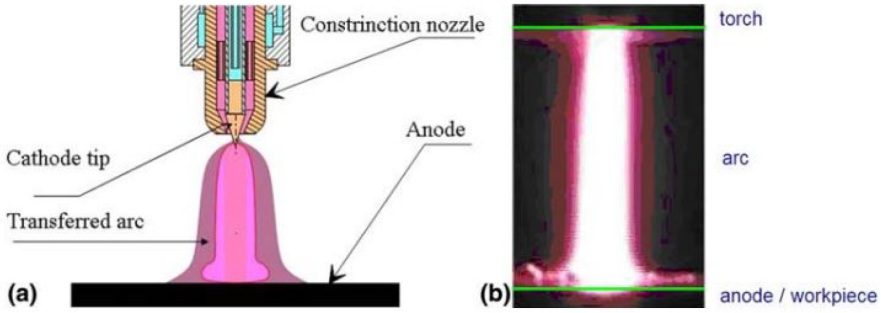

FIGURE 2.10: Image and schematic of a plasma torch arc interacting with metal surface [32].

2.5.1 Emission Lines

In general, atomic emission lines are the observation of electronic transitions from excited electronic states in an atom or molecule to another excited electronic state of lower energy. This is sketched in Figure 2.11. The difference in energy of the two states is emitted in the form of a photon. These photons have characteristic wavelengths, which is expressed in the Planck relation. The states' individual energy levels are a function of the quantum state of the atoms' electrons [33, 34].

Emission lines provide important information about the population of excited species in plasmas such as those produced in this work. The relative intensity of transitions that reach any given end state indicate relative population of said end state. Figure 2.12 features the spectrum produced by a microwave-based argon plasma [35]. This spectrum is consists of argon emission lines.

Neutral argon's energy levels as well as transitions between them are described in Figure 2.13 [36]. Each state is given a label called a Paschen label. For the purposes of this work, these Paschen labels just act to identify the different excited energy states that electrons occupy in neutral argon. The $1s_5$ and $1s_3$ states are metastable states of argon. Some of the transitions between different excited states are labeled with the corresponding wavelength of light that is produced as the de-excitations occurs. Many of these identified lines are detectable by the spectroscopic equipment that is used in this work: from $\sim 190\,\text{nm}$ to $970\,\text{nm}$. It is noted that transition to the ground state of argon will emit photons with wavelength on the order of $107.4\,\text{nm}$ or less, and therefore will not be detected by the spectroscopic instruments.

Similarly, transitions between close-by energy states will not be detectable either, given that their wavelengths are too large. For instance, a transition between the 13.48 and $13.33eV$ states will release a photon of $8270\,\text{nm}$. It should be noted that neutral argon atoms will not have the same energy state levels as singly-ionized argon, doubly ionized argon, and so on [37].

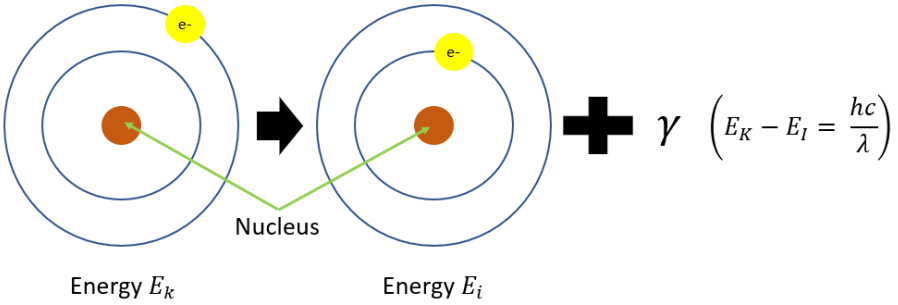

FIGURE 2.11: Sketch of atomic excitation reaction.

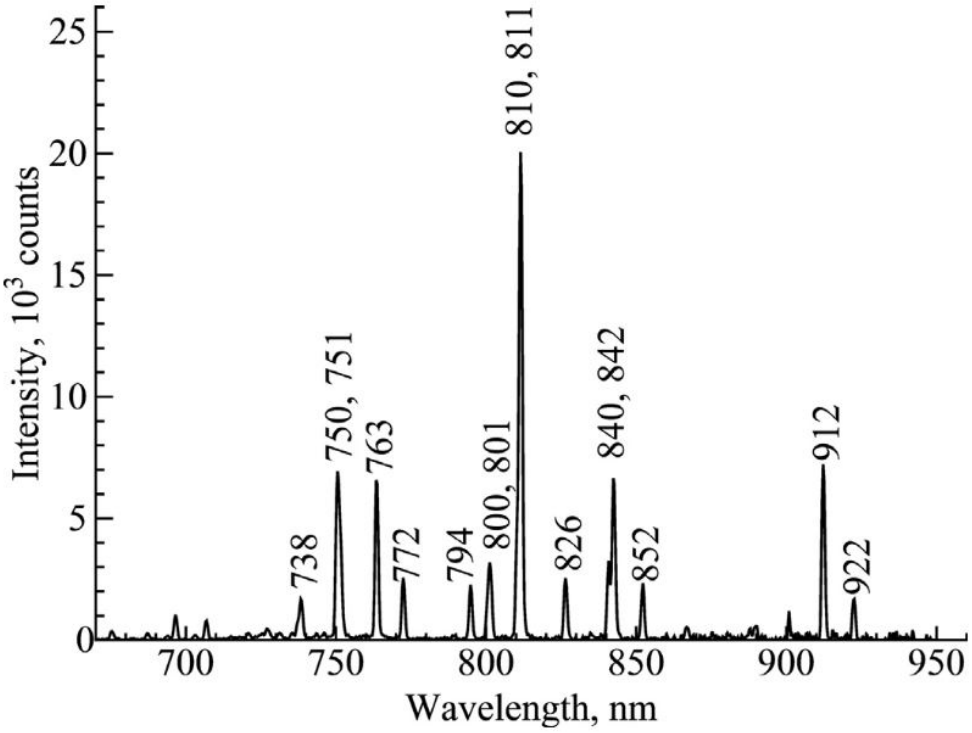

FIGURE 2.12: Emission spectrum of argon plasma produced in microwave system. Taken from [35].

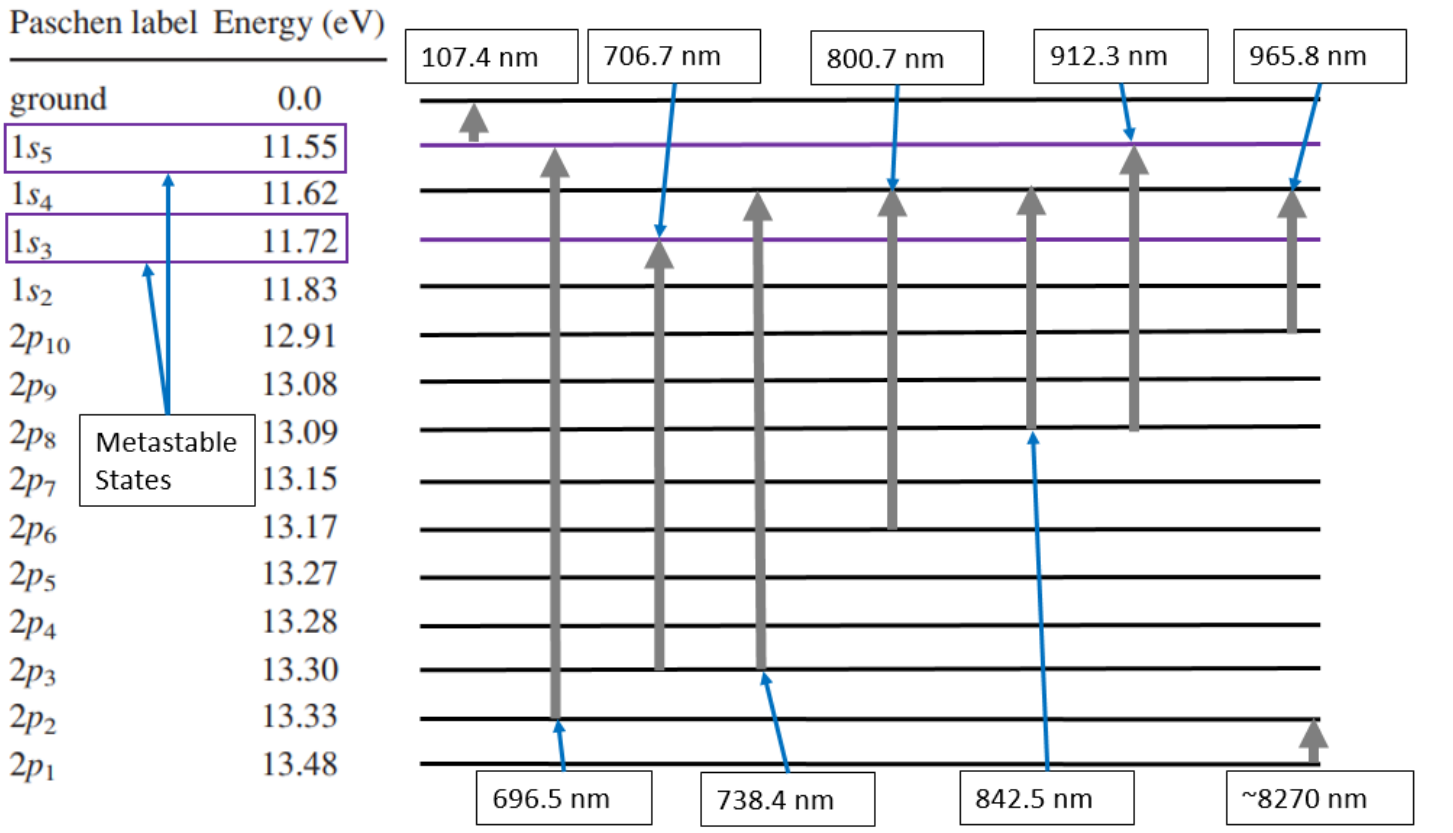

FIGURE 2.13: Sketch of electronic transitions in neutral argon with associated energy levels and photon wavelengths to demonstrate transitions between different excited energy states. Figure built from [36].

Transition Probability Relation to Mean State Lifetime

Transitions from one electronic state to another occur over time in an analogous manner to radioactive decay, where the rate of de-excitation for atoms from state k to state i is proportional to the population of the initial state k. This proportionality constant is the associated transition probability A_{ki} [34, 38]. A_{ki} can also be expressed as a pseudo-lifetime ($T_{lifetime}$) of an excited state, which is expressed as its inverse: [34].

$$T_{lifetime} = \frac{1}{A_{ki}} \tag{2.7}$$

The relative intensity of emission lines in a plasma, along with the associated transition probability play a role in the method of calculating the plasma temperature. This will be discussed in a later section.

2.5.2 Emission Line Broadening

Emission spectra of atoms do not take the form of a series of vertical spikes. For a variety of physical reasons, any emission line, in a plasma or not, will be blurred or smeared. This transforms the emission line from a spike of intensity to a distribution. If broadening terms in a plasma emission spectra can be isolated, they may provide information about its physical properties, such as its local density and temperature. The three types of line broadening that are expected to be encountered are Doppler broadening, natural line broadening, and pressure broadening. These are discussed in this section. These line broadening sources, including those not discussed in this work, generally form a peak on a measured spectrum that takes a Gaussian or Lorentzian appearance. These peaks are often characterized by their Full-Width-Half-Maximum (FWHM). A FWHM describes the width of the distribution at half of its peak (maximum) value [34].

Doppler Broadening

Doppler broadening is produced by the relative velocity of the emitter atoms and the observer. While a source and observer may be at rest with respect to one

another, the mean squared velocity of the atoms in the source are not zero, and cause a shift in the emitted photon wavelength. This mean squared velocity is a function of the temperature, allowing for a measurement of Doppler broadening to be a representation of the plasma's temperature. Doppler broadening is expressed in terms of the emitter's atomic mass μ and temperature T [34]. The Doppler broadening of a peak of wavelength λ takes the form of a Gaussian distribution, with FWHM ($\Delta\lambda_{FWHM}$), where

$$\Delta\lambda_{FWHM} = 7.16 \times 10^{-7}\lambda\left(\frac{T}{\mu}\right)^{\frac{1}{2}} \tag{2.8}$$

Natural Line Broadening

Natural line broadening occurs from the non-zero lifetime of an excited state. Recall that there exists a transition probability between two states A_{ki} and the fact that it can represent the mean lifetime of the excited state, or an uncertainty in its lifetime. By Heisenberg's Uncertainty Principle, the product of the uncertainty in energy and of time $\Delta E\Delta t$ is bounded at a minimum. The uncertainty in time can be expressed in terms of uncertainty in frequency Δf, and the broadening in frequency Δf can be expressed in terms of the emission probability A_{ki} in equation 2.9 [34, 38].

$$\Delta f = \frac{A_{ki}}{2\pi} \tag{2.9}$$

This broadening in frequency space takes the form of a Lorentzian distribution with a FWHM of Δf. The broadening in frequency can be shown to be related to the broadening in wavelength through the relation in equation 2.10.

$$\frac{\Delta f}{f} = \frac{\Delta\lambda}{\lambda} \tag{2.10}$$

In this case, $\Delta\lambda$ is the broadening term in the spectrum, $\Delta\lambda_{FWHM}$ [34]. Re-arranging and expressing in terms of wavelength λ,

$$\Delta\lambda = \frac{A_{ki}\lambda^2}{2\pi c} \tag{2.11}$$

where c is the speed of light.

Broadening in Measured Spectrum Due to Instrumental Error

When measuring the spectrum of any light source, the true line shape will inevitably be distorted by the optical and geometric properties of the instrument used to observe it [39]. The of sources of known spectral shapes such as lamps and laser pointers can assist in determining instrument error. The removal of instrument error when determining values such as the Doppler Broadening FWHM is vital. This will not be explored in detail in the Materials and Method section, but will be important information to consider when performing the spectroscopic analysis.

2.5.3 NIST Database

The National Institute for Standards and Technology (NIST) Atomic Spectra Database is used in order to identify emission lines of excited and ionic species that are present in the plasmas produced [37]. There are two types of emission line lists consulted: detailed lists with assorted information such as electronic configuration, and lists of "strong lines" that provide an intensity estimate. The former is used primarily for the Saha Plots, for which information about transitions between electronic states is an input. The latter is used in the identification of additional lines in the plasma experiments of this work. These lists are discussed in detail in Appendix A.

NIST Database Species Labeling Conventions

When describing the emission lines of a chemical species and its ions, the NIST database differentiates between neutral species and a species' successive ionizations using Roman numerals. For instance, neutral argon is denoted as "Ar I", its first ionization state as "Ar II", its second ionization state as "Ar III", and so on. This convention is followed throughout this thesis.

Emission Line Detail Lists

The database provides additional information on electronic transitions with given initial and final electron configurations. The database provides other data such as the transition probability A_{ki} [37]. The database estimates relative intensities using a method beyond the scope of this work. These intensities are meant to act as a guideline to identify emission lines when peaks in a spectrum are close to one-another as well as when spectrometer wavelength resolution is limited. Table 2.3 shows a selection of argon emission lines. All of the information listed in Table 2.3 is used in plasma temperature estimation calculations. Many of the argon strong lines are in the 690 nm to 1000 nm region, making emission line spectrometers that can measure spectra in this region suitable. This is discussed in Appendix A.

Strong Line Lists

The NIST database also provides emission line lists called "Strong line lists". They contain less information than the detailed lists, but are used to identify species that are present in a plasma. These lines contain the species type (neutral or ionic), an estimate of the relative intensity, and the wavelength associated with the line.

Metastable States

Metastable electronic states are excited electronic states in an atom that have a longer decay time [37]. A thorough understanding of how this arises is beyond the scope of this work. Argon's metastable states have energies of 11.55 eV and 11.72 eV [36].

As seen in Appendix A, many of these metastable states are end-states for many the higher intensity lines of argon. The detection of these states will help inform some of the properties of the argon plasma produced in some of the experiments outlined in this thesis.

TABLE 2.3: Sample NIST emission line data for argon emissions including energy terms, wavelengths, and transition probabilities. Included is the letter grade describing the uncertainties in transition probability. Taken from [37]

Observed Wavelength Air (nm)	Rel. Int. (?)	$g_k A_{ki}$ (s^{-1})	Acc.	E_i (eV)		E_k (eV)
415.8590	400	7.00e+06	B	11.54835433	-	14.52891337
419.0713	100	1.40e+06	B	11.54835433	-	14.50606752
419.8317	200	2.57e+06	B	11.62359262	-	14.57594866
420.0674	400	6.8e+06	B+	11.54835433	-	14.49905352
425.9362	200	3.98e+06	B+	11.82807106	-	14.73811524
426.6286	100	1.6e+06	C+	11.62359262	-	14.52891337
427.2169	150	2.4e+06	B	11.62359262	-	14.52491318
430.0101	100	1.88e+06	B+	11.62359262	-	14.50606752
433.3561	100	2.8e+06	B+	11.82807106	-	14.68829018
451.0733	100	1.18e+06	B+	11.82807106	-	14.57594866
603.2127	70	2.21e+07	C	13.07571560	-	15.13054424
641.6307	70	5.80e+06	C	12.90701519	-	14.83881088
667.7282	100	2.36e+05	B	11.62359262	-	13.47988670
675.2834	150	9.65e+06	C	12.90701519	-	14.74254073
687.1289	150	8.34e+06	C	12.90701519	-	14.71089798

2.6 Other Physical Phenomena of Interest in this Work

This section describes two physical phenomena that may have been encountered through throughout this work. They are worth describing due to their impact on the observations made, and applications towards future work.

2.6.1 Penning Ionization

Penning ionization consists of the ionization of an atom X due to an interaction with another that is at a metastable excited state, A^{**} [40]. The metastable atom imparts energy to atom X, which results in a de-excitation of A^{**} to a de-excited atom A. Atom X releases an electron of some velocity from the energy imparted to it and becomes ionized into species X^{+}. Penning ionization only occurs if the metastable state's energy is higher than the ionization energy of the target atom X [40]. A Penning ionization reaction is described in equation 2.12.

$$A^{**} + X \rightarrow A + X + e^{-}. \tag{2.12}$$

In the argon plasma produced in this work, there are four main chemical elements are expected to be observed: the argon that makes up the argon plasma, carbon, which is part of the plasma seed, and finally the iodine and cesium that are added as part of the investigative work. The ionization energies of these elements will be of interest if Penning ionization is to be considered a possible mechanism of ionization. Table 2.4 tabulates the ionization energies of these elements.

Element	First Ionization Energy (eV)	Second Ionization Energy (eV)
Argon	15.76	27.63
Carbon	11.26	24.38
Cesium	3.89	23.16
Iodine	10.45	19.13

TABLE 2.4: Tabulated first and second ionization energies for argon, carbon, cesium, and iodine. Taken from [37].

These values are extracted from the NIST Atomic Spectra Database [37]. As stated earlier, the metastable states of neutral argon have energies of 11.55 eV and 11.72 eV. These energies are higher than the ionization energies of carbon, cesium and iodine, making Penning ionization a possible mechanism of ionization. Penning ionization may be confirmed as a possible mechanism by detecting emission lines associated with Argon's excited metastable states.

It should be noted that the standard enthalpy of formation for cesium iodide is $3.59eV$ [41]. That implies that it takes $3.59eV$ of energy to break the ionic bond between cesium and iodine in the cesium iodide compound. In this case, excited states (metastable or otherwise) of argon that interact with the cesium iodide salt have sufficient potential energy to break its bond.

2.6.2 Thermophoresis

Many experiments conducted in this work result in the atomization and suspension of particulates into plasmas. The plasmas produced are expected to form temperature gradients, and therefore suspended particulates would be expected to undergo some sort of thermophoresis force [20]. Thermophoresis is the phenomenon where suspended particulates feel an effective force due to them being present inside a gas or plasma that has a temperature gradient [42]. Thermophoresis forces may apply towards or against the temperature gradient, depending on the properties of the particulates [43]. Figure 2.14 shows suspended particulates undergoing the thermophoretic force due to them experiencing a temperature gradient. In this case, the particulates are experiencing a force which pushes it with the temperature gradient. Modeling the forces that the atomized particulates produced in the experiments is not the scope of this work , but this phenomenon may be a factor in experimental observations.

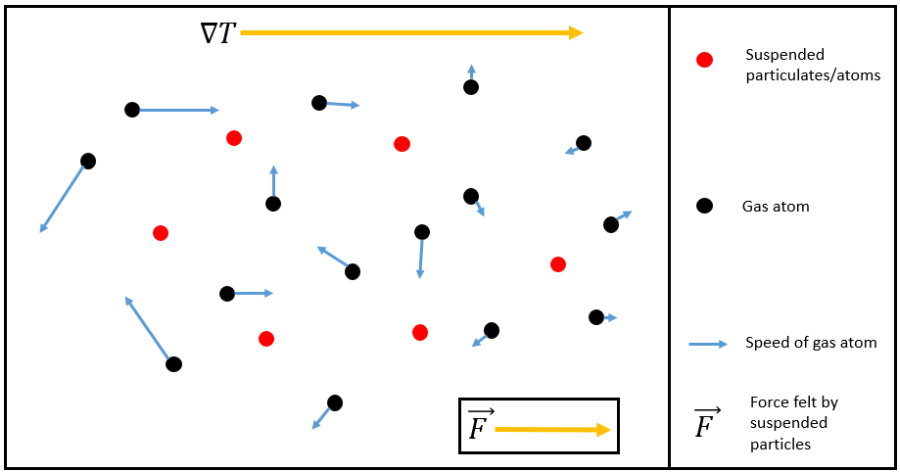

FIGURE 2.14: Sketch of a suspended atoms or particles undergoing thermophoresis. The arrows can be associated with the mean speed (related to temperature) as the suspended particles. Not to scale.

Chapter 3

Materials and Methods

3.1 Description of Approach

The approach of this work is to replicate conditions produced by a plasma cutting torch in its dismantling environment. In general, there is no precise control over the temperature and constituents of a plasma produced by an arc plasma torch in an industrial environment. The plasma produced in the arc is also a multi-species plasma that may also have a dust component as metal is being vaporized and melted as the cut is performed. This is illustrated in Figure 3.1.

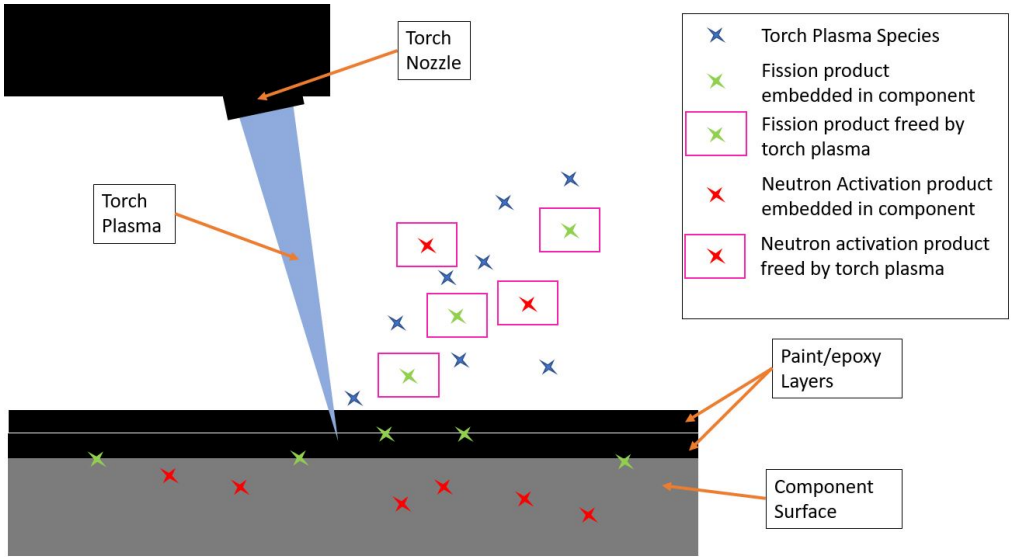

FIGURE 3.1: Visualization of aerosols produced by a plasma cutter.

The boxed species are those that are of interest: the released radionuclides. The complexity of a system of plasma, cutting surface, radionuclides, and so on would make accurate analysis difficult. An indirect understanding of the overall behavior can be achieved. A laboratory plasma, where a higher degree of control over its constituents and parameters can be produced and characterized qualitatively and quantitatively. This approach was useful in providing an understanding of the torch plasma and the parameters that may affect the operation of an arc plasma torch in a decommissioning environment. After characterizing the laboratory plasma, chemical equivalents of the contaminants in various forms, were added to the plasma. This was done to simulate the reaction of radionuclide contaminants in a plasma. The resulting emission spectra was analyzed for molecular and atomic forms. While the contaminants are introduced the characteristics of the plasma can be changed in a precise manner, such as varying its temperature by changing microwave power. This provided a window in what reaction products are produced as a function of temperature or other parameters. A commercial plasma torch was used to emulate the types of cuts taking place on metallic components. The emission spectra of the arc plasma produced was observed, and temperature measurement methods can be explored to analyze the temperature of the torch. Similar to the laboratory plasma, metallic components that are coated with the same contaminant analogues introduced into the controlled plasma can be cut with the torch. The presence of the physical forms of these contaminants were measured using the same spectroscopic methods as those with the analysis of the controlled system. The observations were compared to those in the controlled system. The physical forms the contaminants take, such as molecular, neutral, and ionic, will help inform the types of technologies that can be used to capture the aerosols in a decommissioning scenario.

The two experimental setups in this work can have their experimental conditions varied by the user. This is outlined in Table 3.1. The plasma gas for both can be changed, the flow rate, and the introduction of the species. The two systems have different means of changing the imparted power to the system.

TABLE 3.1: Tabulation of how Plasma Torch and Microwave Plasma setups' conditions.

Experimental Parameters	**Plasma Torch**	**Microwave Plasma System**
Power imparted to the plasma/plasma gas	Current supply of the torch can be varied from 15 A to 28 A.	Control over output microwave power to high certainty (± 10W). Stub tuners, and field applicator plunger allow for high control over how much microwave energy is imparted to the plasma gas.
Gas flow rate	Gas pressure of the torch internal air compressor may be varied from 0 PSI to 200 PSI.	Gas flow rate can be controlled by changing argon gas bottle flow rate. Flow meter allows precise knowledge of gas flow rate.
Plasma gas	Air is readily available to use via the torch unit's internal air compressor. Argon and other gasses can be used with appropriate gas hose attachments to torch power supply.	Argon gas readily available to use. Other gases can be used with appropriate gas hose attachments to a gas pump or compressor.
Addition of mock-contaminant species	Any solids that can be glued to the surface of sheet metal sample. Any liquids that can be mixed into glue	Any solids that can be woven/wrapped into quartz wool bundle.

From the literature review, it was inferred that the changing of the conditions in Figure 3.1 can change the parameters of the plasma. For a given plasma, changing the gas flow rate and input power will invariably change the temperature and density of the plasma. The microwave plasma system will be seen to have a stronger means of precisely controlling input power, gas flow rate, and the contaminant species introduced when simulating decommissioning processes.

3.2 Microwave Plasma System

The controlled plasma that was studied in this work is an atmospheric argon plasma that is produced inside an assembled microwave waveguide system. This called the microwave plasma system. There were two configurations used in this work. One configuration for the testing and calibration of the system's instruments, and the other for plasma production.

Schematics of both waveguide configurations are featured in Figures 3.2 and 3.3. The primary differences between the two configurations are the heat loads. The testing configuration uses a closed-loop chilled water system to absorb microwave energy. The other confiuration uses a cylindrical chamber called the field applicator to apply microwave energy to a column of argon gas. All microwave components will be discussed in this chapter. The assembled microwave plasma system is shown in Figure 3.4.

The microwave source consists of a magnetron which is powered by a SM845 high voltage power supply produced by MKS Instruments [44]. The magnetron is a model TMA20 manufactured by MKS Instruments [45]. It is specified to produce microwaves up to an output power of 2000 W. It is water-cooled and has a W340 waveguide connection. It produces microwaves at $2.45GHz$, which is suitable for the W340 waveguide connection. The magnetron is required to be have some minimum flow of coolant to keep it below a temperature of 40 C. The minimum flow rate is verified using an internal sensor. This is due to the fact that waste heat is a byproduct of microwave production. This waste heat may damage the components of the magnetron.

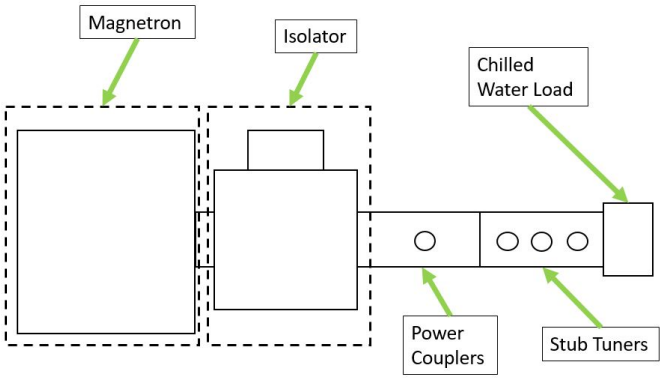

FIGURE 3.2: Schematic of microvave waveguide system with chilled water load.

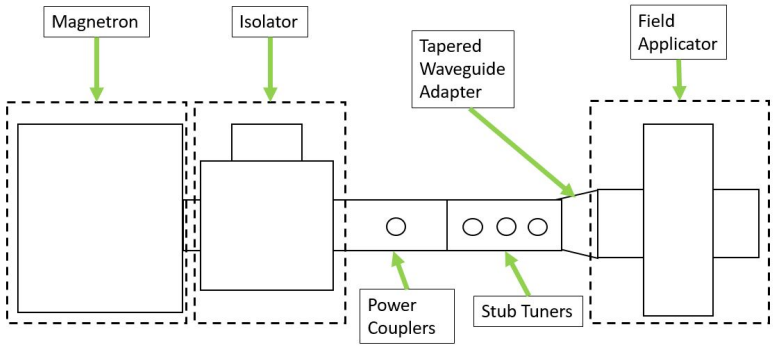

FIGURE 3.3: Schematic of microwave waveguide system with field applicator.

3.2.1 Coolant System

Many components of the microwave system require coolant to maintain component temperatures at a safe and operable level. The laboratory chilled water system was used for this purpose. It is a closed loop system that continuously circulates a nitrite solution of water, which is generally held below 10 degrees Celsius. This value is based on temperature measurements over months of experiments. The magnetron, isolator, and the water-chilled heat load (even when not in use) are connected to this system in the manner illustrated on Figure 3.5. The isolator and water-chilled load are components that will be discussed in later sections.

Two flowmeters were used: F-400N series flow meter manufactured by Blue-White industries [46] which can measure up to 5 $\frac{L}{min}$, and an FL-10G flow meter which can measure up to 2.5 $\frac{L}{min}$ manufacturered by OMEGA Engineering [47]. The flow rate through the F-400N flowmeter into the isolator heat sink is measured to be 1.5 litres per minute, while the flow rate into the FL-10G flowmeter is measured to be 2.15 $\frac{L}{min}$ (through the chilled water load) when the coolant system is run at full pressure.

3.2.2 Microwave System Controls

The microwave output is produced, monitored, and controlled by the high voltage power supply and control panel.

High Voltage Power Supply

The high voltage power supply is the SM845 High Voltage Power Supply (Figure 3.6) manufactured by MKS Instruments [44]. It provides all the necessary power to the magnetron [44]. It features an LCD display that can be programmed to report and change various operating conditions in live time. The power value of microwave output is adjusted using the adjuster knob. It is noted here that the LCD display of the power supply failed during the course of this work. This did not impede on progress, as the important values reported by the display can be determined by other means.

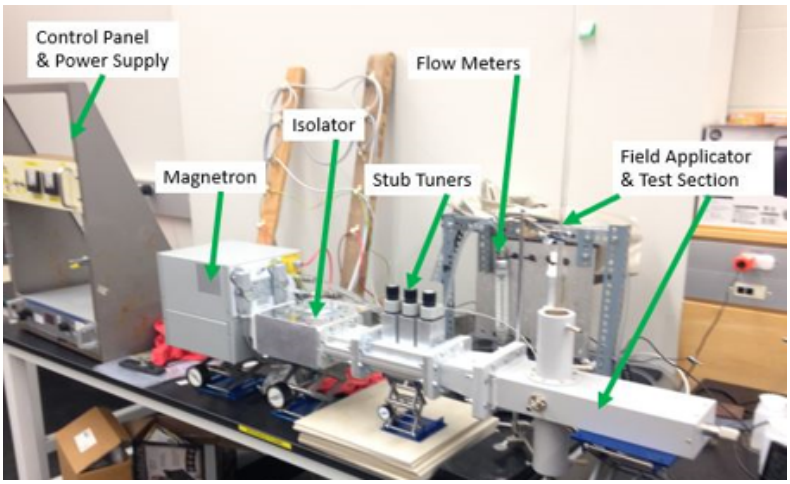

FIGURE 3.4: Photo of microwave plasma system with field applicator and test section.

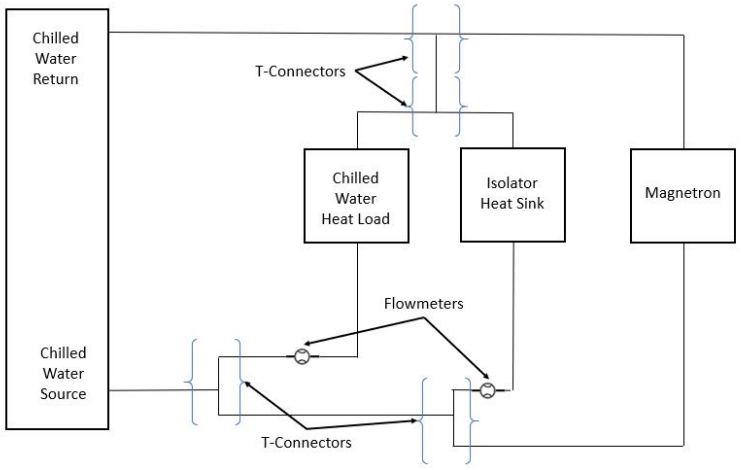

FIGURE 3.5: Flow Diagram of Microwave System Components in chilled water cycle. Arrows indicate direction of coolant flow.

Control Panel

The control panel features various LEDs and lamps that, in other working modes, specify the states of the microwave components. The enable and hibernate switches enable and disable microwave output. Two monitors output a voltage signal which represents the forward and reflected microwave power. The control panel is wired according to the wiring diagram in Figure 3.8. The wiring diagram is taken from power supply user manual [44].

The panel interfaces with the High Voltage Power Supply (HVPS) using a 25-pin connector. The pin wiring is specified in the manufacturer's manual [44]. The lamps and volt-meters were chosen and wired based on the specification provided in the HVPS manual as well, with one exception: the specified voltmeter monitors have less input impedance than specified. This is addressed in a later section.

The control panel is fastened on a fixture above the power supply as seen in Figure 3.4. A photo of the panel is shown in Figure 3.7. The panel's primary use is the enable and disable switches and to view the microwave power information that the monitors provide.

3.2.3 Production and Transmission of Microwaves

Microwaves are produced as current flows through the magnetron at a high voltage. The microwaves then pass through the isolator, the power coupling unit, and the stub tuners. Some microwave energy is likely absorbed along the way, but this is assumed to be negligible due to the components being specified as loss-less. Most of the microwave energy is deposited onto the load at some fraction of the initial amount. The rest are reflected. The reflected energy is deposited to some extent into the stub tuning and power coupler units, and the remainder is deposited into the isolator. The isolator is designed to redirect all reflected microwave power into its heat sink, protecting the magnetron head from damage. The fraction of microwave power that is deposited onto the load and the isolators heat sink is dependent on the tuning settings and the load component used. The transmission of microwaves through the waveguide system is sketched in Figure 3.9. Appendix C estimates the minimum coolant flow necessary to the isolator.

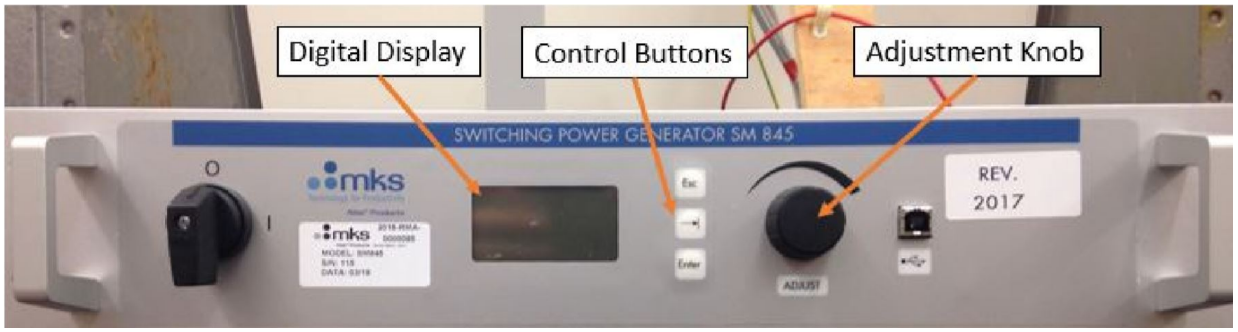

FIGURE 3.6: Magnetron high voltage power supply.

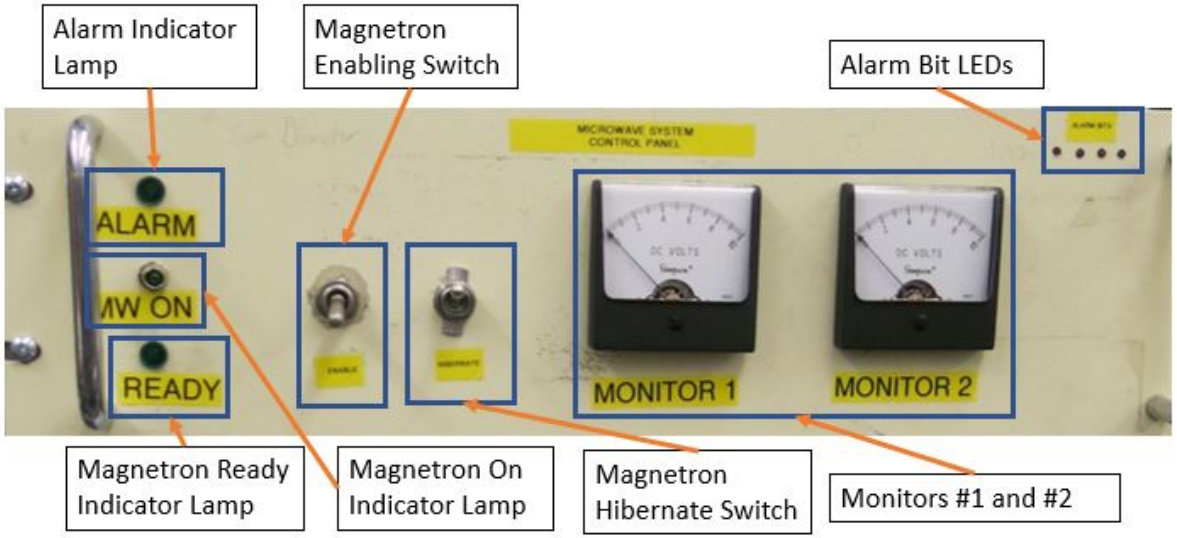

FIGURE 3.7: Photo of microwave system control panel.

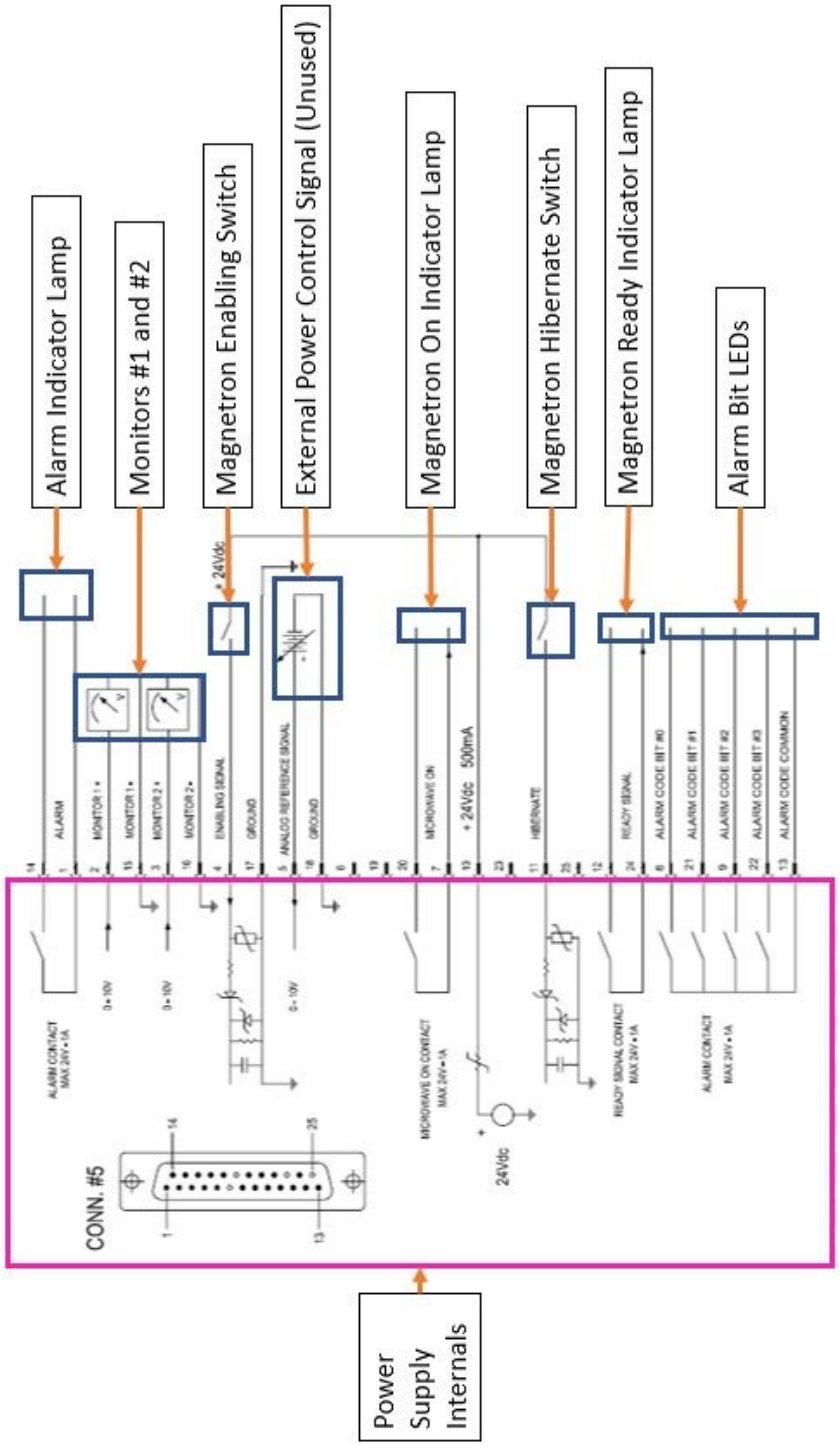

FIGURE 3.8: Microwave system control panel wiring.

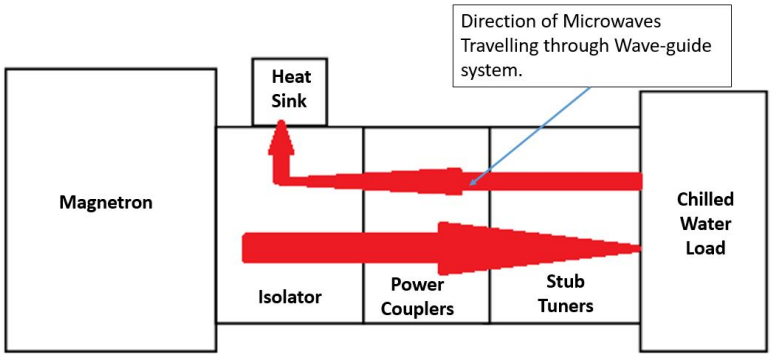

FIGURE 3.9: Deposition of microwave energy throughout microwave waveguide system. Energy is primarily deposited in the heat sink of the isolator and the attached load.

To maximize power transfer to the load, the tuning stubs are adjusted. One way to view transmission of microwave energy is through the realization that a steady waveform of EM fields is being produced inside the wave-guide by the microwaves. The intensity of these fields as a function of space will dictate where the energy is being deposited. Changing the tuning stubs changes the shape of the fields (and energy deposition profile) inside the wave-guide [48].

Microwave Transmission

The microwave waveguides used for transmission are primarily WR340 rectangular waveguides. These waveguides are cavities of specified cross-sectional dimensions: 86.36 mm by 43.18 mm. These cavity dimensions are suitable for the transmission of 2.45 GHz microwaves.

Isolator

The isolator is the component that protects the magnetron head from reflected microwave energy. Its first opening is connected to the magnetron. Its exit leads to the primary branch of the waveguide system: the sensors, stub tuners, and loads. The isolator also contains is a water-chilled heat sink. It is is designed to redirect any reflected microwave power from the primary branch into its heat sink

rather than passing through back into the magnetron, to protect the magnetron from damage.

Stub Tuners

The stub tuning unit is the AG340M3 unit manufacturered by MKS Instruments [49]. It consists of three equally spaced conductive stubs. To insert and retract the stubs, the knobs can be turned counter-clockwise and clockwise respectively. Each stub can individually retract to be flush with the wall of the wave-guide and be inserted up to a maximum length of 25 mm. Due to the different types of loads that can be attached to the microwave system, the stub tuners are used to change the effective load impedance. This is a means to control where and how much microwave power is deposited [48].

3.2.4 Load Attachments

There are two load attachments that are used with the microwave system. They are designed to focus the microwaves being produced by the magnetron onto a region where the microwave energy will be absorbed.

Water-Chilled Load

The water-chilled load focuses microwaves onto chilled water coolant channels. It was used in preliminary testing of the microwave system and in the re-calibration of the power sensor box, which is an issue which will be discussed in a later section.

The chilled load may also act as a safety measure for future experiments: if another load component is placed between the chilled load and the stub tuners, then the water chilled load can act to absorb unabsorbed microwaves before they reflect back towards the isolator and magnetron. Figure 3.10 features shows of the interor and exterior of the water-chilled load.

Field Applicator

The field applicator is a cavity that applies microwave power to objects placed in the center of its hollow cylindrical section. It is in this component that the plasma

is produced, by heating a column of argon gas in the cylindrical cavity. That detail will be discussed later in this chapter. Figure 3.11 displays the exterior of the field applicator. The field applicator has two optical ports (also called a viewport in Figure 3.11 and 3.12) that allow for the viewing of the interior of the cavity from the exterior. It is in these two view-ports that fiber optic cables are positioned to collect light from the plasma emissions. The field applicator end is equipped with a movable conductive wall, which is controlled by a plunger. This plunger controls the positioning of the wall, which changes the shapes of the microwave deposition [50]. The plunger is kept retracted at 150 mm, as that setting in combination with certain stub tuning settings was found to allow consistent plasma production. These settings were determined by preliminary system testing. The interior of the field applicator is shown in Figure 3.12.

The field applicator cavity is a WR430-type rectangular waveguide. Its internal cavity dimensions are 109.22 mm width by 54.61 mm height. These cavity dimensions are also suitable for the transmission of $2.45GHz$ microwaves. The field applicator is attached to the main branch of the wave-guide using a tapered adapter due to the fact that their size of openings do not match. The model of tapered adapter is the GA2017 manufacturered by Gerling [51]. The tapered adapter linearly shifts from the WR340 size to the WR430 size, which allows for an essntially "loss-less" connection, as per the manufacturer.

3.2.5 Microwave Power Measurement

The forward and reflected microwave power values in the waveguide system are measured using the power couplers. The signals produced by the couplers are then interpreted by a power sensor box which relays a DC signal to the power supply. The power supply interprets these DC signals as a power value which can be programmed to appear on its display and relays these values to the monitors on the control panel in the form of a voltage signal.

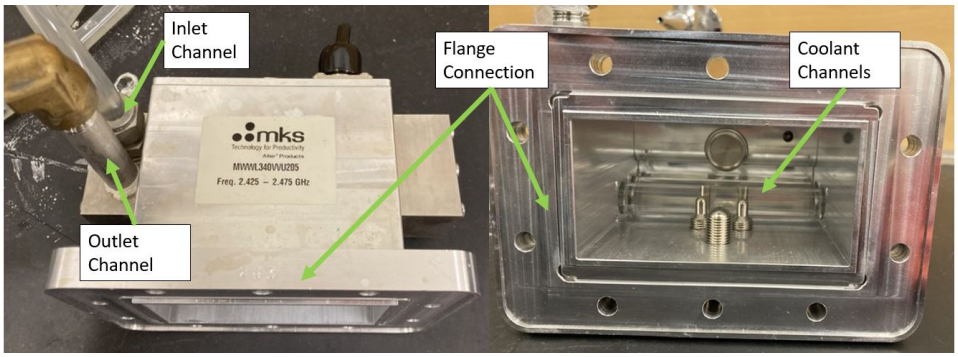

FIGURE 3.10: Image of water-chilled load exterior.

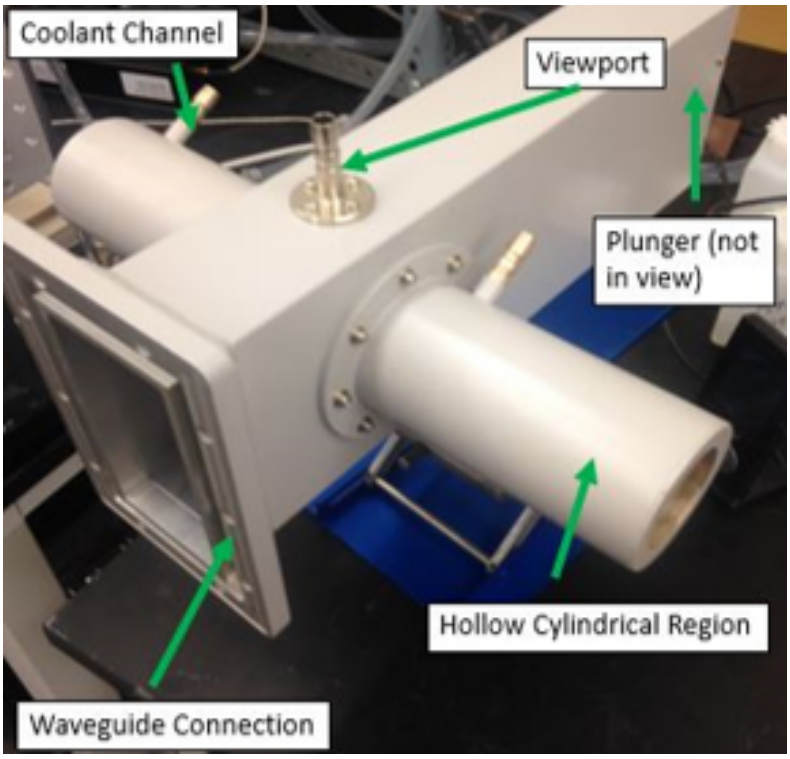

FIGURE 3.11: Image of field applicator exterior.

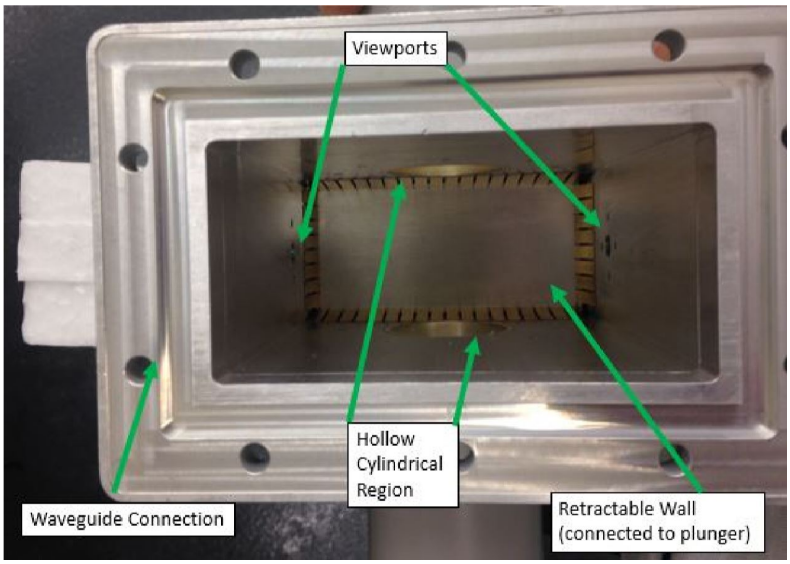

FIGURE 3.12: Image of the interior of the field applicator.

Power Couplers

The power couplers are manufactured by MKS Instruments [52]. They are designed to re-direct forward and reflected power inside the waveguide system to the power sensor box. When installed into the waveguide system, one redirects a small fraction of forward power, the other redirects a small fraction of reflected power. Each side labelled "A" or "B" to keep the calibrations consistent.

Power Sensor Box

The RD800 sensor box, manufactured by MKS Instruments, interprets the signals sent to it by the power couplers [53]. It is equipped with two sensor ports. One is rated to measure power levels up to 1000 W, and the other measures up to 2000 W. When connected to the display, the signal received by the 2000 W and 1000 W ports are interpreted on the display as forward and reflected power respectively.

Control Panel Monitors

The control panel, as seen in Figure 3.7, features two voltmeters, labelled ”Monitor 1” and "Monitor 2". Monitor 1 measures the forward power, and Monitor 2 measures the reflected power, where each 0.1V on the scale is *specified* to represent 20W and 10W on each respective meter.

Connection Configurations

Two connection configurations were used for this work. These configurations are kept constant because of the calibration measures described in Appendix D.

Configuration 1: For Monitor 1

- "A"-side of the power coupler measuring forward power towards chilled load
- Cable from "A"-side to 2000 W port on the RD8400 Sensor Box with attenuator.
- Power information displayed as "Forward Power" on the display in Watts and in Monitor 1 as a voltage signal.

Configuration 2: For Monitor 2

- "B"-side of the power coupler measuring reflected microwave power away from chilled load
- Cable from "B"-side to 1000 W port on the RD8400 Sensor Box without attenuator.
- Power information displayed as "Reflected Power" on the display in Watts and in Monitor 2 as a voltage signal.

Microwave Power Measurement Calibration

During microwave production experiments with the chilled water load attachment, the forward and reflected power values displayed by the power supply display and monitors were known to be incorrect:

- The configuration 1 values were saturating to a maximum of 2000 W for low output (200W) microwave powers. The output microwave powers were initiailly verified to not be the reported 2000 W values by noting a negligible temperature difference in the heated load. A temperature difference of several degrees would be expected to be felt by the load.
- The positioning of the RD8400 sensor box and its cabling appeared to influence the Forward and Reflected powers reported on the display.
- Configuration 2 was consistently reporting lower-than-expected power values when swapped to measure forward power.
- Monitors 1 and 2 were known to have insufficiently high input impedances.

Two measures were put into place in order to rectify some of issues:

- An attenuator was procured and inserted into the connection between the Forward-direction power coupler and the RD8400 sensor box. This is featured in Figure 3.13. This prevented signal saturation.

- Conductive fabric, known as Faraday Cloth, was placed over top of the RD8400 sensor box to act as a Faraday cage. This cloth was laid over the sensor box in order to protect it from stray microwave signals, which may affect the signals that it receives/transmits. The conductive fabric was grounded by connecting to the Microwave System's common ground. An image of this is featured in Figure 3.14.

These changes and pre-existing issues still meant that the microwave power values on the display were inaccurate, but made calibration possible. As such, a method of "re-calibrating" the monitors was needed. The re-calibration of the control panel monitors was done by measuring the temperature differences between the coolant before it is being heated by microwaves at the inlet, and measuring the temperature of the heated coolant at the outlet. Calibration curves mapping monitor voltage V to an estimate of the true microwave power P measured by the couplers were produced. The method of doing so is described in Appendix D.

Figure 3.15 features both resultant calibration curves for the monitors.

With the coupler connection to sensor box configurations (#1 and #2), the Forward and Reflected microwave power were known by consulting Monitors 1 and 2 respectively without needing the LCD display.

3.2.6 Plasma Production

As mentioned previously, the plasma is produced inside the cavity of the field applicator. This section describes the apparatus in which the argon plasma is produced, its function, and a high-level description of how the plasma production takes place.

Test Section

The test section is used to contain argon gas as it is expelled from its source container, as well as the plasma as it is generated, is referred to in this work as a test section. A schematic of the test section is featured in Figure 3.16.

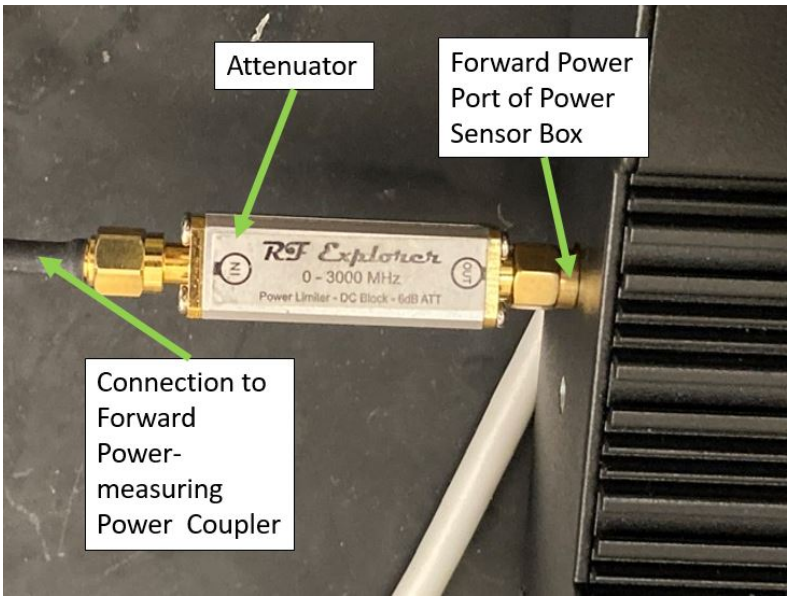

FIGURE 3.13: Attenuator Component to prevent saturation of power measurement.

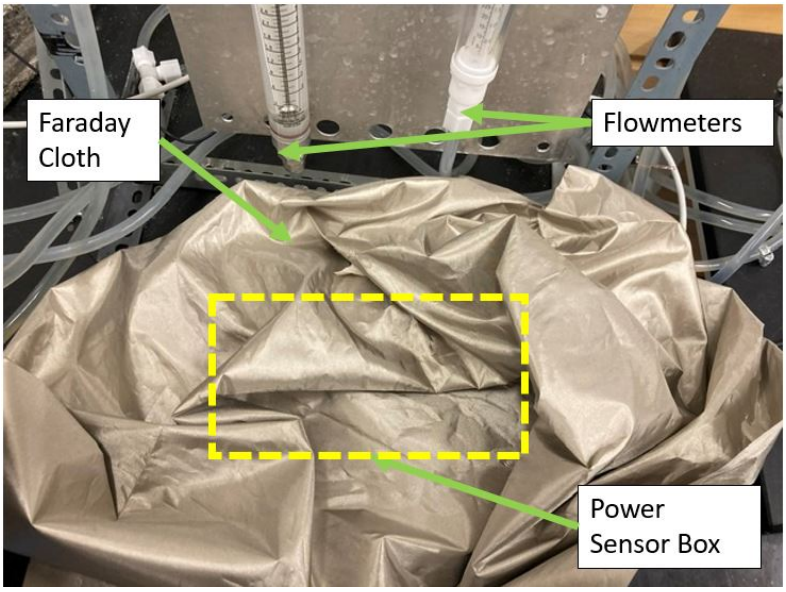

FIGURE 3.14: Metallic fabric used to shield sensor box from microwaves. Fabric was also grounded.

The test section consists of two nested glass tubes. The outer tube remains as one piece. The inner tube is cut into two sections. The inner tube is used to hold a plasma seed in place, using quartz wool. The plasma seed is made of carbon material. The test section is built so that the carbon seed bundle points upwards, with the intended flow of gas. Fused quartz wool acts to partially seal the inner tube from the gap between the tubing, and to hold the hold the seed in place. The tubing positions are held in place using rubber hoses of various sizes. The gap between the inner and outer tubes are sealed from the unwanted entry of air using rubber hose and electrical tape. Glass tubing is used in order to allow visual inspection of the plasma, and to allow for spectroscopic measurements from many angles and positions. The quartz glass essentially evenly transmits light in the wavelength range of 200 nm to 2000 nm, according to the manufacturer.

Plasma Seed The plasma seed is made of carobn material and is wrapped in the quartz wool where it is held in place inside the test section. When heated with microwaves, the carbon acts as an electron donor as it reaches a high temperature (rather than ionization which is not possible with microwaves), allowing the plasma to be produced by the liberated electrons which are then excited with the microwaves. With the current setup and power levels used in experiments, the plasma seed, along with its positioning in the center of the field applicator's cavity, is essential for the argon plasma to be produced.

Tubing Material Choice The type of glass used in the tubing is fused quartz glass. Fused quartz tubing, rather than Pyrex or glass tubing, is used due to its higher melting point. The argon plasma temperatures calculated in this work are on the order of 2000 K, which is hot enough to melt glass materials such as Pyrex. Pyrex, for instance, has a melting point on the order of 1200 K, whereas the fused quartz glass used in this work has a melting point of 1956 K, according to private correspondence with the manufacturer, ChemGlass. Some previous experiments used plain glass for the plasma experiments and resulted in warping and melting.

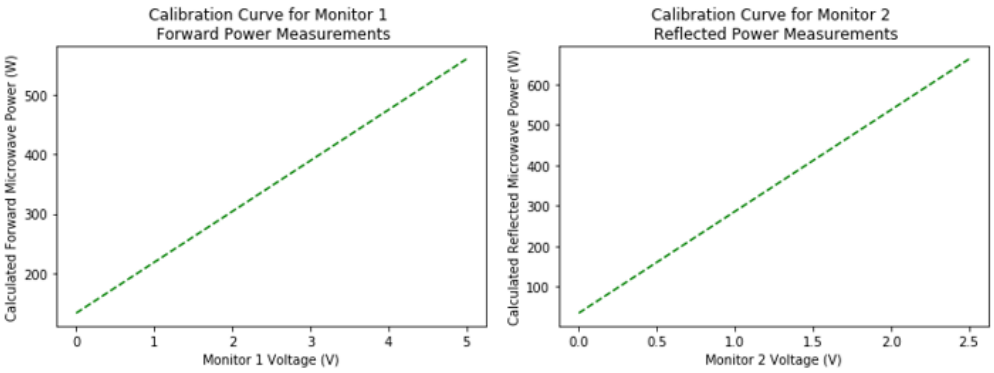

FIGURE 3.15: Calibration Curves for Voltmeter Monitors 1 and 2, which measure forward and reflected power respectively.

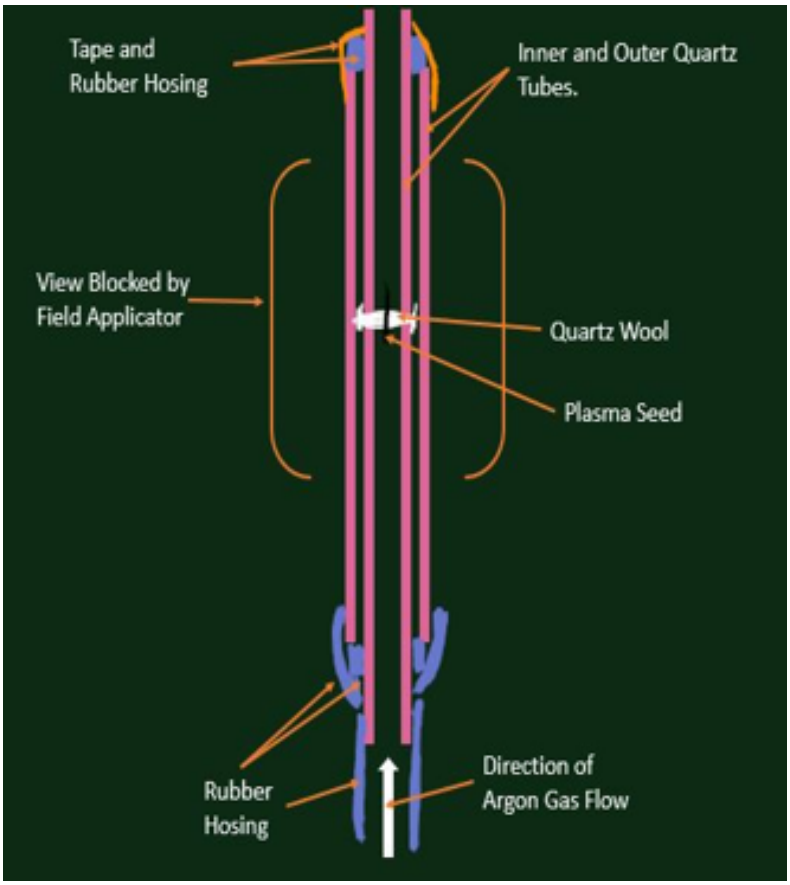

FIGURE 3.16: Sketch of test section design.

Gas Connection An argon gas bottle, through a flow regulator and flow meter, connects to the bottom opening of the test section. As a note, only the top of the test section is left open to the atmosphere. The gap between the inner and outer tube, as mentioned earlier, is sealed using electrical tape.

Energy Deposition Inside Field Applicator

As argon gas is pumped through the test section inside field applicator, and as the plasma is produced, energy is deposited into the gas/plasma. This is sketched in Figure 3.17. Using a microwave meter, it was determined that very little microwave leakage (around 1 W) occurs outside of the field applicator as the plasma is produced. In the figure, the "focal point" (geometric center) of the field applicator is identified.

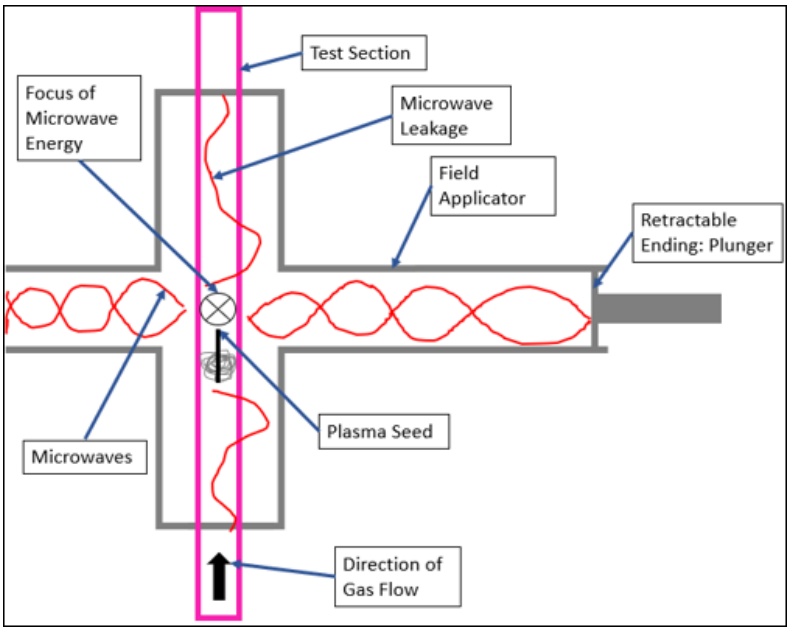

FIGURE 3.17: Microwave energy deposition inside field applicator. Energy focused near plasma seed in order to produce argon plasma. Microwave leakage may occur out of the open regions.

Clamp Positioning

The test section was held in place by clamping at two locations from above. The stand and clamps were all made of conductive metal. To help prevent plasma and streamer attraction to clamps, which was annoyance associated with experimental failures in the initial tests, the stand was connected to the wave-guide system's common ground, and the clamps covered in Teflon tape. Teflon tape acts as a dielectric helping shield electric fields (and therefore forces). The tape also helps the clamps grip the smooth tubing. When used in experiment, the central portion of the test section becomes very hot, especially where the plasma is produced, due to the conduction of heat from the plasma. A schematic of the clamping configuration is included in Figure 3.18.

3.2.7 Fibre Optic Cable Placement

When used to analyze the emissions produced by the plasma, the fibre optic cables were positioned at the optical ports of the Field Applicator. This would provide a direct view of the focal point region where the plasma is produced. These cables were held in place using lab retort stands. The clamping is featured in Figure 3.19. These cables will be described in more detail in a later section.

3.3 Spectroscopy Systems

There are two spectroscopy systems used in this work. The first is a high-resolution system that uses a monochromator to isolate and scan through narrow wavelength ranges at a high resolution with low instrument broadening. The other spectroscopy system used is a Black Comet manufactured by StellarNet, which provides a live-time broadband spectrum.

3.3.1 DK-480 Monochromator

The monochromator in use is a DK480 half-meter monochromator produced by Spectral Products [39].

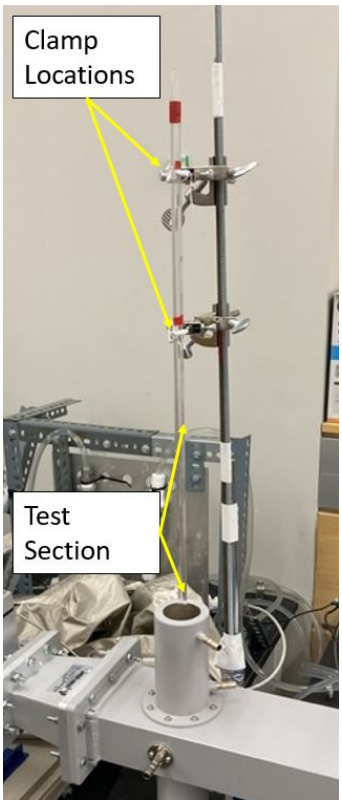

FIGURE 3.18: Image of clamp positions for test section. Clamping done from above, allowing for test section to hang freely below.

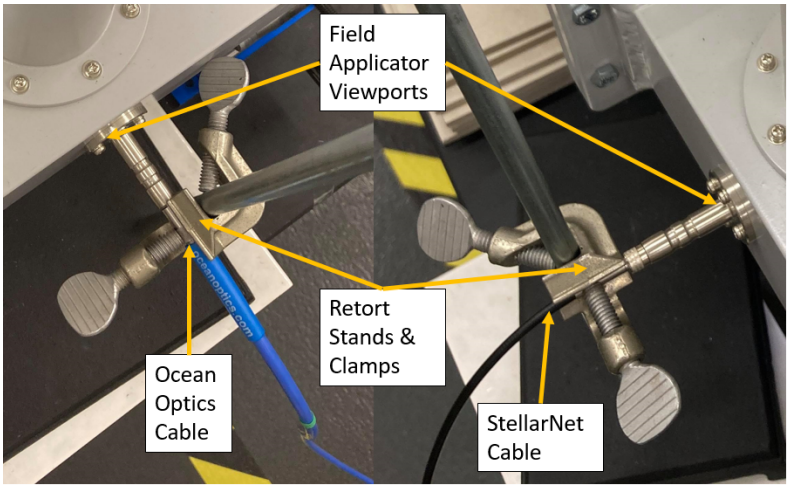

FIGURE 3.19: Positioning of Fibre Optic Cables at Field Applicator entrances.

The internal structure is similar to the type shown in Figure 3.20. Light is piped to the monochromator entrance slit and reflects off of a mirror. The incoherent light is split into its respective wavelengths using the rotatable grating. Because the light is now split into its spectrum, the wavelength of light is selected by the thickness of the the exit slit, with the rest being blocked. In the schematic in Figure 3.20, a range of wavelengths in the green region is selected. The angle of the grating dictates the range of wavelengths being selected. The light, after it passes through the exit slit, strikes a Charge Coupled Device (CCD), which records the intensity of light which strikes it. The monochromators entrance and exit slit widths can be independently changed from 10 µm to 10 000 µm with a resolution of 1 µm. The slit widths play a role in how much light enters the monochromator as well as how much light hits the CCD. This indirectly affects the instrument error and the uncertainty in measurements. There is a trade-off between the intensity and resolution of the spectra produced by measurements using the monochromator, as will be seen in later sections. Monochromator spectral measurements involve scanning through a set of wavelengths using pre-selected wavelength bins whose spacing can be as low as 0.01nm [39]. The monochromator wavelength and CCD intensity recordings are simultaneously controlled using software provided by the manufacturer. The intensity values are recorded as in units of counts. These counts are rounded to the nearest integer and may also be averaged. The intensity scale in spectra, as a result of the rounding and averaging are interchangably reported as having arbitrary units (A.U.) or units of counts. The monochromator provides high resolution measurements for this work. This comes at a cost: scanning large ranges of wavelengths that are hundreds of nanometres wide can take minutes to perform. For most experiments that measure time-evolution of emission lines, the Black Comet was used instead.

Detector Module

The AD131 detector module is the CCD used record intensity values. It transforms photon collisions into a voltage value, which is represented as integer counts in the spectroscopy software. The AD131 detector has multiple features, such as an internal amplifier which can multiply signals by an integer between 1 and 10.

The detector is capable of measuring wavelengths from 190 nm to 1000 nm. The detector is also capable of automatically averaging the intensity it measures over multiple samples. For this work, 200 samples were used for each datapoint.

Entrance Adapter

The monochromator features an entrance adapter which allows for a direct connection from the entrance slit to the fibre optic cable. The adapter is shown in Figure 3.21. The adapter allows for x,y,z-directional movement using knobs. The fibre optic cable connector is covered in the figure.

The x,y,z knobs are adjusted to their optimal position by using a high intensity source, such as a laser pointer or calibration lamp. The entrance slit is initially kept open at a large entrance thickness (5000 µm) and knobs are adjusted to maximize intensity. The entrance slits are closed to a shorter entrance thickness, and the process is repeated as described in [54].

3.3.2 Black Comet Spectrometer

The Black Comet system is a spectrometer manufactured by StellarNet. The Black Comet has the ability to provide rapid and continuous spectral snapshots from 180 nm to 850 nm. The Black Comet bins the intensity values into wavelength bins. The size of these bins vary from 0.24 nm (higher wavelengths) to 0.41 nm (lower wavelengths), making the wavelength uncertainty larger than that of the monochromator. The internal structure of the Black Comet is similar to that of the monochromator. It has the same mirror, grating, mirror configuration, but the grating is held in place. A detector array is held in place that captures the light. The light splits into its respective spectrum, which is then resolvable by mapping the detectors along the array to different wavelengths. This is featured in Figure 3.22. The Black Comet is capable of taking spectral snapshots at frequencies of 10 Hz. These rapid snapshots are useful when studying systems that evolve quickly over time. The plasmas produced in this work (and the light they emit) can evolve at shorter time scales than what the DK480 monochromator can scan.

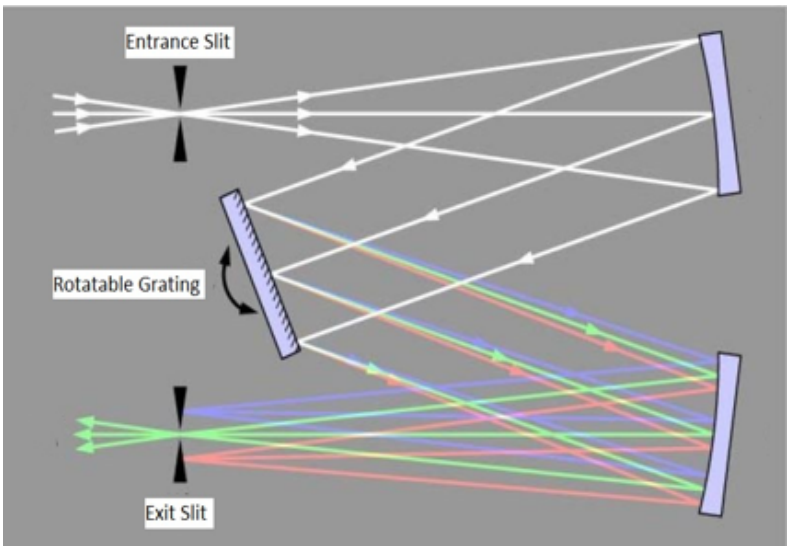

FIGURE 3.20: Schematic of monochromator's internal structure.

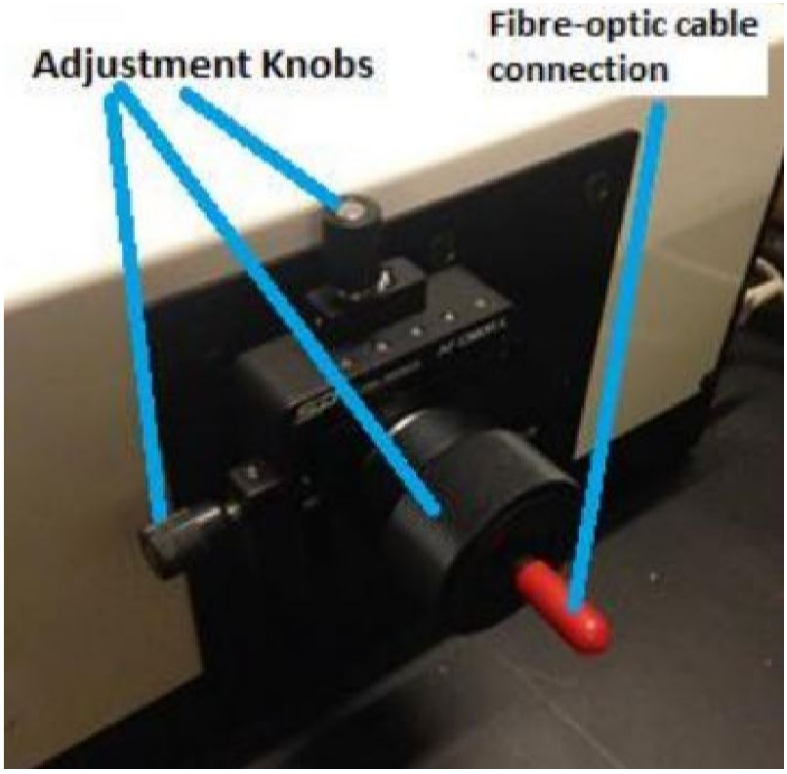

FIGURE 3.21: Entrance adapter to monochromator.

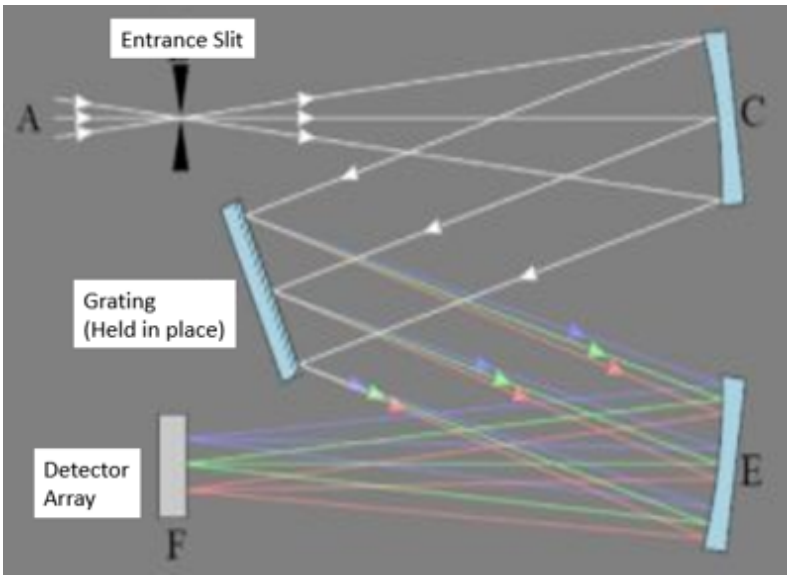

FIGURE 3.22: Photo of Black Comet Spectrometer interior.

3.3.3 Calibration Lamps

There are two calibration lamps that were used to verify the calibration of the spectrometer systems. The first is an AR-2 argon lamp, which is a pure argon emission source, and an HG-2 mercury lamp, which consists of a mix of argon and mercury. Both are manufactured by Ocean Optics [55]. The mercury lamp is used for its shorter wavelength emission lines, allowing for calibration into the shorter wavelength regions down to 253 nm. The argon lamp has emissions in the longer wavelengths. Calibration curve were generated by plotting the measured emission line wavelengths from the lamp spectra against the known emission line wavelengths from the NIST database [37].

DK-480 Monochromator Calibration

The Monochromator had its calibration verified using the AR-2 lamp alone, since all of its spectral measurements were done in the 700nm to 980nm range. Figure 3.23 features the AR-2 lamp spectrum as measured by the monochromator.

The calibration curve generated by the monochromator is featured in Figure 3.24. As seen in the figure, the wavelengths have a slight offset of 0.04 nm. Apart from this offset, the monochromator is well-calibrated.

Black Comet Spectrometer Calibration

The Black Comet easily can measure wavelengths from 180 nm to 850 nm. The HG-2 and the AR-2 lamps were both used to cover the full range of the spectrometer. Figures 3.25 and 3.26 feature the spectra of the lamps measured by the Black Comet. The calibration curve is shown in Figure 3.27. In this case, the Black Comet has an offset of 0.3 nm. It is important to keep track of this offset value as it helps prevent confusion of emission lines when dealing with regions where many peaks in spectra may overlap.

Comments on Calibration Curves

The calibration offsets for the DK480 and Black Comet are taken with a grain of salt. The plasmas produced experimentally do not have as stable behavior or the same spectral shapes as the calibration. As such, it is assumed that these offsets may change. In order to identify weaker lines, the offset has to be determined first, which is typically done by searching for stronger known emission lines and re-estimating the offset. This comment only affects the identification of lines.

3.3.4 Fibre Optic Cables

The fiber optic cables used in the spectroscopy system are 400 µm diameter UV VIS cables manufactured by StellarNet, as well as UV-VIS 100 µm diameter cables manufactured by Ocean Optics. The Stellarnet fibre optic cable is capable of measuring intensities from 190 nm to 2200 nm [56]. The Ocean Optics fibre optic cable is optimized to measure intensities from 300 nm to 1100 nm [57].

Both calibration lamps allow for direct connections with these cables, as well as the DK480 monochromator entrance adapter, using an SMA905 connection. For the microwave argon plasma experiments, the 400 µm diameter cables are used to deliver an increased intensity of light to the monochromator.

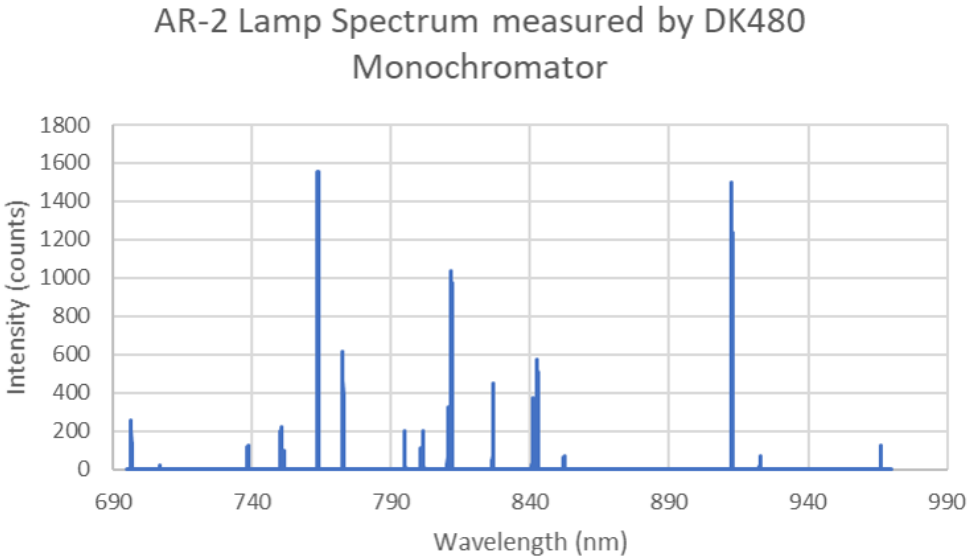

FIGURE 3.23: AR-2 argon lamp spectrum as measured by DK480 monochromator. All peaks in the spectrum are that of argon.

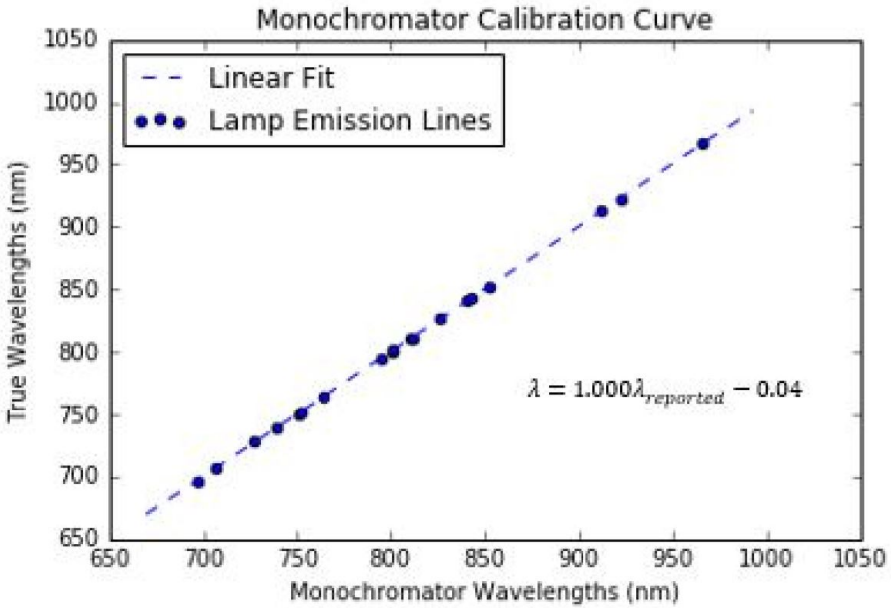

FIGURE 3.24: Calibration curve and line of fit for DK480 Monochromator using the AR-2 lamp. Peaks measured will tend to have an offset.

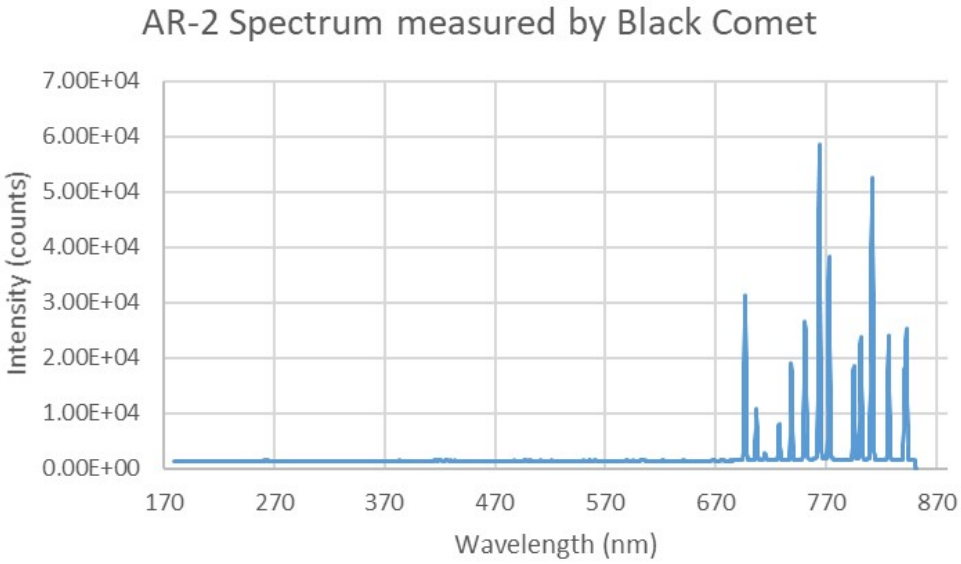

FIGURE 3.25: AR-2 argon lamp spectrum as measured by Black Comet. All peaks in the spectra are that of argon.

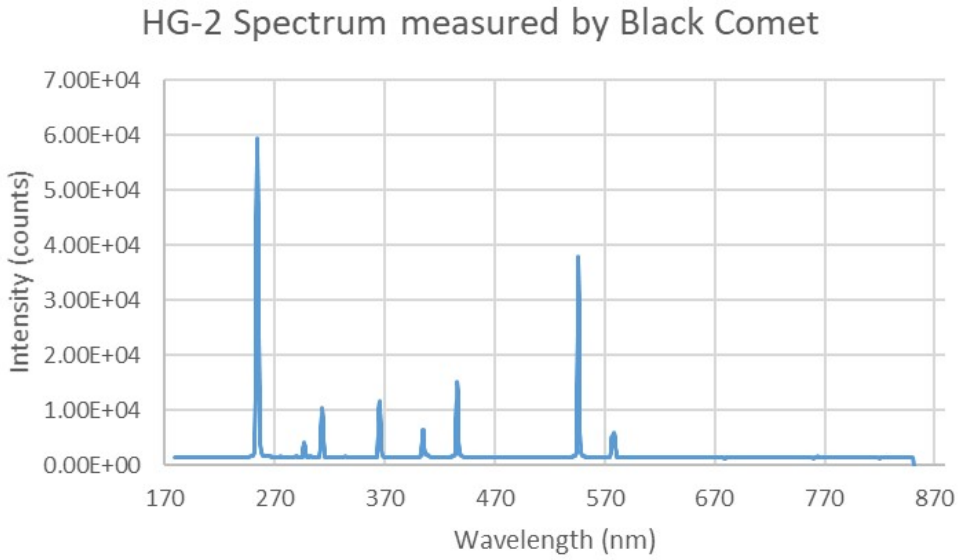

FIGURE 3.26: HG-2 mercury lamp spectrum as measured by Black Comet. All peaks in this spectra are that of mercury.

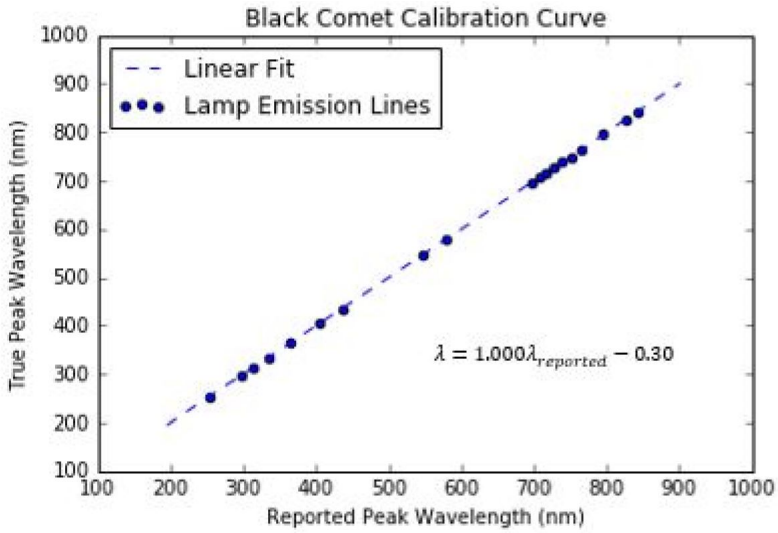

FIGURE 3.27: Calibration curve and line of best fit for Black Comet. Peaks measured will tend to have an offset.

The 100 µm cables were used with all experiments involving the Black Comet, as the Black Comet did not need the increased intensity of light delivered by a thicker inner diameter cable.

3.4 Plasma Torch Setup

This section describes the experimental setup for the plasma torch experiments.

3.4.1 Plasma Torch

The plasma torch used is a Lincoln Electric Tomahawk 375 [25]. It is an arc plasma torch that is specified to cut metal up to 3/8ths of an inch, or 9.525 mm. The torch functions as an arc plasma torch, as described in the literature review. It features an internal air compressor that can take the supply of air from the work-space and use it as the plasma gas. For this work, the internal air compressor was used. As a result, the plasma produced by the torch is an air plasma.

3.4.2 Experimental Enclosure

The plasma formed by the torch causes rapid melting and vaporization. Sparks and metal flecks can spread throughout the environment if they are not contained. A metal enclosure in combination with a welding blanket are used to assist in the containment of sparks and flecks as the cuts take place. In addition, a fume extractor is included to siphon out fumes of paint and other products generated during cuts. The cutting enclosure is pictured in Figure 3.28.

Plasma Torch and Fibre Optic Cable Setup

Two setups were used for the plasma torch experiments: one cutting samples from above using the torch, as would be seen in normal operations, and one cutting from below. The latter was used for most experiments because the plasma torch could be held in place with little effort, making the operation of these experiments more consistent. Figures 3.29 and 3.30 feature sample and torch setups for cutting from above and below.

3.5 Procedures

Procedures have been developed with the intention for future researchers to reproducibly build experimental apparatuses, perform experiments, and to operate equipment that were used in this work. This section provides a description for each of them.

3.5.1 Microwave Production Procedures

Microwave Production

The microwave production procedures provide instructions for safely and consistently producing microwaves of a known power inside the waveguide system. They include guidelines for using the display menu and display knob to change performance parameters of the microwave head in order to obtain a desired power output. These procedures were always run using the chilled water load [58–61].

Power Meter Calibration

The power measurement component of the waveguide system has a calibration procedure outlined due to the meters not correctly reading their values. This procedure outlines how to perform the heat transfer calculations described in Appendix D. This allows for the voltages recorded on monitors 1 and 2, which are a function of the Forward and Reflected microwave powers, to be mapped to a "truer" microwave power value [62].

3.5.2 Argon Plasma Production Procedures

A detailed procedure of plasma production as well as a test section construction guide is described in this section. These procedures outline the building of a test section where the plasma is produced and contained, as well as the tuning, gas flow, and microwave settings to use in order to reproduce the plasmas produced in this work.

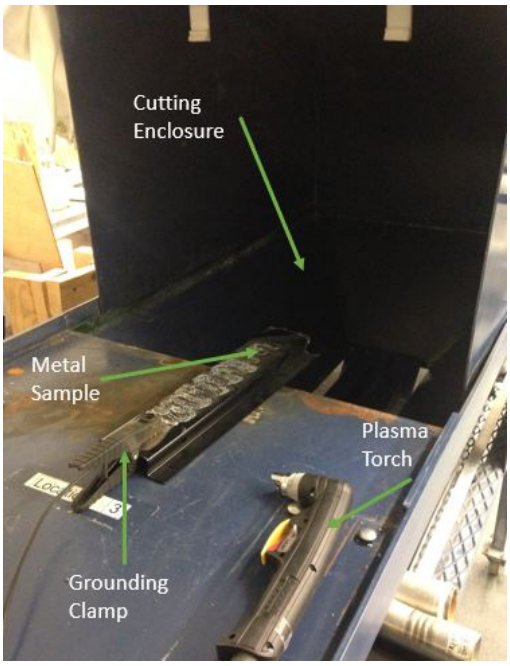

FIGURE 3.28: Photo of plasma torch cutting enclosure.

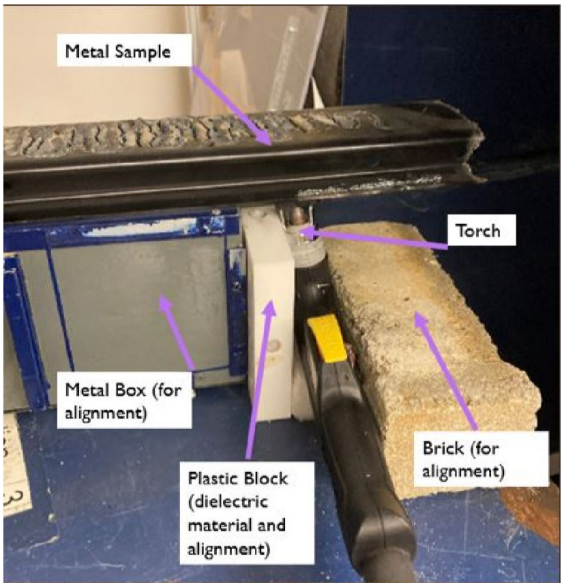

FIGURE 3.29: Setup for cutting metal components from below with the plasma torch.

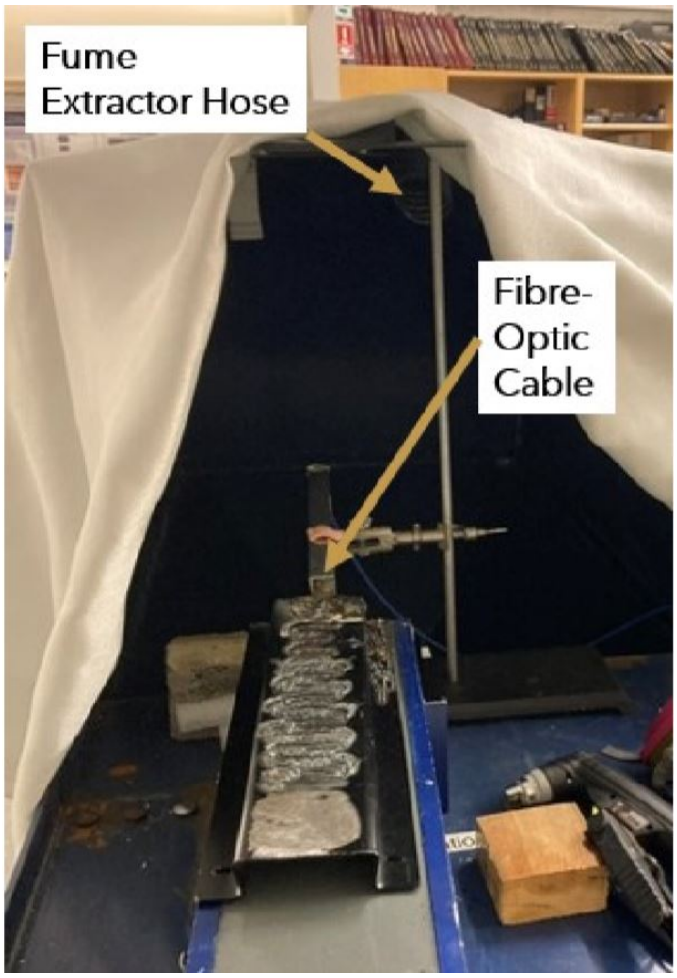

FIGURE 3.30: Setup for cutting metal components from above with the torch. Fibre optic cable held in place with retort stand and clamp.

For all experiments involving argon plasma production in the microwave system, laser safety glasses were worn in order to block many of the strong emission lines produced by the plasma. They are manufactured by Eagle Pair. They were specified to attenuate wavelengths from 190 nm to 540 nm, as well as 800 nm to 1700 nm. These glasses helped protect the eye from strong ultraviolet and strong infrared light that the plasma would invariably produce. Many of the emission lines identified for argon are in the 700 nm-800 nm region, as well some being featured in the 200 nm-400 nm region. An image of the glasses are featured in Figure 3.31.

The attenuation properties of the glasses were tested by verifying how they attenuate the light of a broad-spectrum work lamp that also shines light in the regions where argon has strong lines. Figure 3.32 provides four plots that denote the attenuation properties of the glasses. Plot A shows the spectrum of the lamp measured by the monochromator. Plot B shows the spectrum measured but blocked by a lens of the safety glasses. Plot C shows the ratio of the two. Plot D plots the wavelength region where optical density was measurable.

The optical density (measurement of attenuation) is expressed as the following:

$$\text{Optical Density} = \log \frac{I_{Unblocked}}{I_{Blocked}} \tag{3.1}$$

where the log is in base 10 and I_{Lamp} and $I_{Blocked}$ are the incident lamp light and the lamp light blocked by a lens from the glasses, respectively.

The intensity of the lamp is zero from the 450 nm range and below, so these plots only verify the optical density of the glasses from that value to 1000 nm. As a note, the outlier at 600 nm is removed. Plot D plots the optical density of the of the glasses as a function of wavelength. As a note, if the optical density was found to be undefined (i.e. the blocked intensity went to zero), it was assigned a value 4 to facilitate plotting.

From plot C and plot D, the optical density of the glasses are verified to be above 2.5 from 450 nm to 550 nm as well as above 3 for 675 nm and onwards.

FIGURE 3.31: Laser Safety Glasses used for argon plasma experiments.

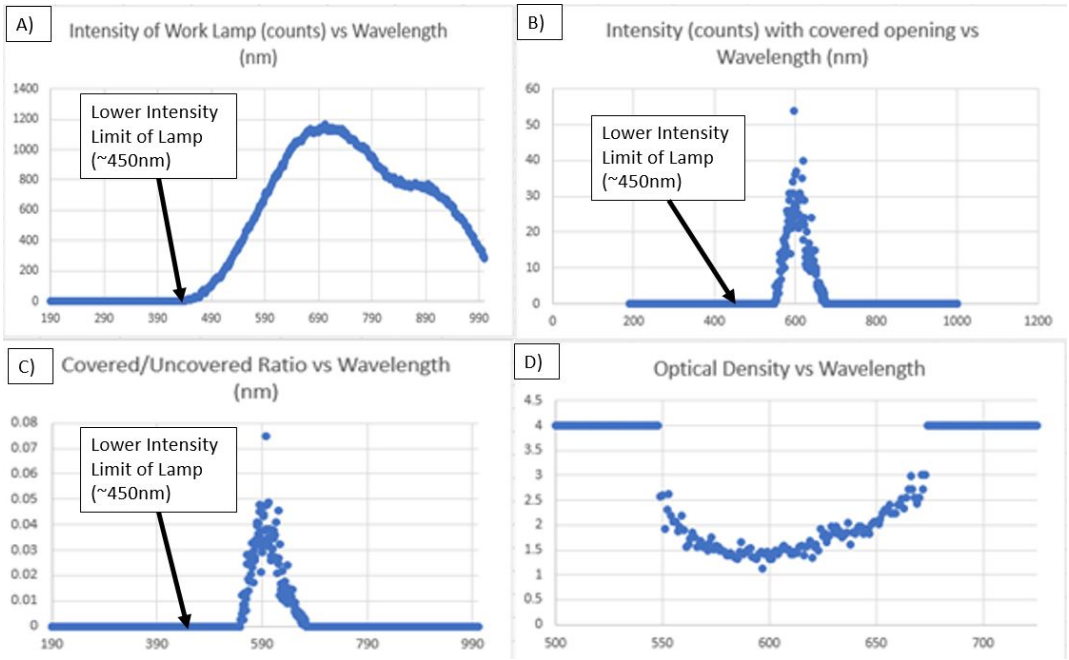

FIGURE 3.32: Plots demonstrating the attenuation properties of the safety glasses from 450 nm to 1000 nm.

Figure 3.32 demonstrates that the optical density of the glasses between 550 nm and 675 nm ranged from 1 to 3, and was above 3 in all other regions. These glasses block the strong emission lines of argon (696 nm and above) based on these plots, making the viewing of the plasma safer for the eyes when these glasses are worn.

Plasma Production with Microwave System

Plasma production with the microwave wave-guide system involves heating argon gas in a column. The argon column is contained within the test section held in place. These test sections in this work allow for the production of plasma in a confined area, where the plasma doesn't react with the outside air. In effect, the sections effectively produce a relatively "pure" argon plasma, assuming no leaks.

Argon Plasma Generation and Measurement Settings

Table 3.2 outlines all of the microwave system, gas flow rate, and spectrometer system settings used for all of the argon Plasma experiments, unless specified otherwise. Input power values vary and are specified in the text.

TABLE 3.2: Table of experimental parameters used for the argon Plasma experiments from procedures.

Parameter	Value
Argon Gas Flow Rate	2.5 L/m
Test section inner diameter	5 mm
Tuning Settings	Stubs #1, #2 and #3 have 7.00, 9.00 and 9.00 mm insertion lengths respectively.
Microwave input power	Varies (Specified in the text)
Plunger Retraction	150 mm
Black Comet Integration Time	100 ms
Magnetron Coolant Flow Rate	1.5 L/m
Chilled Water Load Coolant Flow Rate	2.15 L/m
Fibre Optic Cable for Black Comet	Ocean Optics 100 µm UV-Vis Cable
Monochromator Number of Samples to Average	200 samples per data point
Monochromator Wavelength Step Size	0.1 nm
Monochromator Entrance and Exit slit widths	250 µm
Fibre Optic Cable for Monochromator	Stellarnet 400 µm UV-Vis Cable
Mass of Cesium Iodide Contaminants (when applicable)	0.15 g

Quartz Tube Test Section Construction

A procedure for the construction of the quartz tube test sections for use in the argon plasma production, including the sourcing of the material has been generated [63].

Low Power Plasma Production

This procedure explored the adjustment and use of suitable stub tuner settings to achieve consistent production of argon plasma at a low input power [63].

Plasma Tuning Testing

This procedure investigated the effects of changing the tuning stubs insertion lengths on the value of jet height, the amount of reflected power, as well as the intensity of lines from the argon plasma. [63].

Plasma Jet Height Characterization

This procedure investigated the effects of changing input power as well as gas flow rate on the height of the plasma jet that is formed [64].

Plasma Temperature Dependence on Input Power

This procedure takes spectral measurements of the plasma from the view-port at multiple input microwave powers. These spectral measurements can be transformed into Saha plots by identifying the emission lines from the peaks. The input powers were changed in steps, increasing gradually to a self-imposed 480 W limit, and decreasing gradually down to 220 W [65].

Determination of Cesium Iodide Emission Lines

This procedure used a test section which holds mock contaminants (of a mass on the order of 0.15 g in the same plasma seed bundle. The contaminants in this case would be cesium iodide. The plasma was ignited and held at an input microwave power following normal procedures [66]. Based on previous work [17], it is expected that mechanisms such as Penning ionization would break apart the salt and release

salt constituents into the plasma. The excitation of these constituents are expected to be visible to the spectroscopic equipment.

A spectral image is continuously recorded from the Black Comet spectrometer. This procedure allowed for the determination of cesium and iodine emission lines that form, by comparing the spectrum obtained with the spectra of the argon plasmas produced in earlier experiments. An additional safety measure included in this procedure due to the introduction of iodine into the system. An iodine trap is attached to the top end of the test section using rubber hose. The iodine trap consists of a wool soaked in iodine solution that is sandwiched between dry layers of wool. These layers are held in a funnel. The funnel is attached to the test section exit using rubber hosing. Any atomized iodine that is produced by the plasma travels through the test section (due to the pressure of the gas) will be caught in the iodine-soaked wool. This is based on a design by Harvel et al. [17]. The schematic of the iodine trap is featured in Figure 3.33 and an image of it is in Figure 3.34.

3.5.3 Plasma Torch Experimental Procedures

There were two experiments performed with the plasma torch. One involved the determination of a "baseline" spectrum produced by metal being cut without contaminants. This was done by taking spectral measurements of the plasma produced using the Black Comet. Table 3.3 features the experimental parameters used for the plasma torch experiments.

TABLE 3.3: Experimental parameters used for the Lincoln Electric 375 plasma cutter experiments [67, 68].

Parameter	Value
Working gas	Air- Using Torch's internal air compressor
Gas pressure	50 PSI or 345 kPa (Gauge)
Current Limit	18 A
Black Comet Integration Time	100 ms
Fibre Optic Cable for Black Comet	Ocean Optics 100 µm UV-Vis Cable

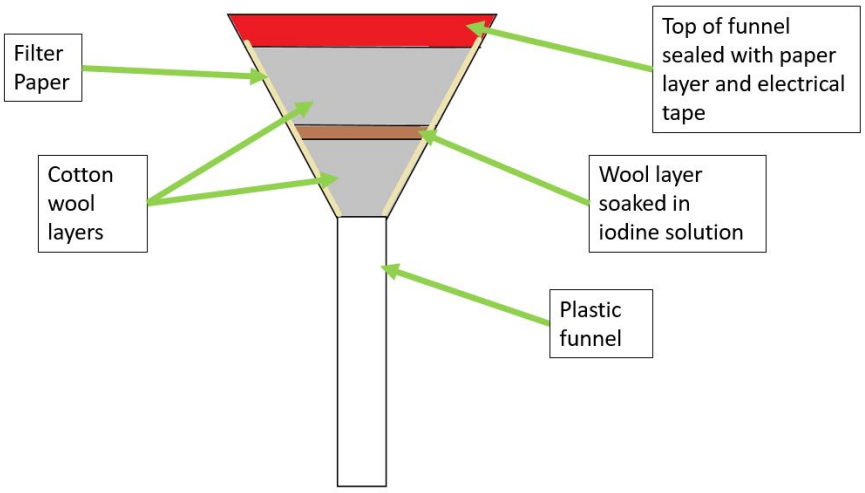

FIGURE 3.33: Schematic of the iodine trap used with the argon plasma test section.

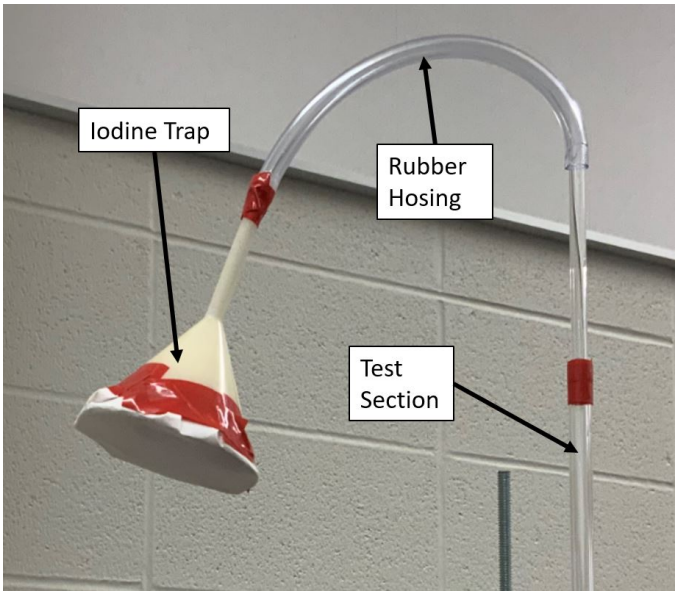

FIGURE 3.34: Iodine trap for experiments involving the introduction of cesium iodide into argon plasma test section.

Cutting of Sheet Metal with Plasma Torch

The Lincoln Electric torch is relatively straightforward to handle. A procedural document in this case has not been formalized, but relies on user training from an experienced user. The usage of the torch is is also constrained based on user knowledge and experience [67]. Protective eyewear that was provided with the torch was worn when cuts took place.

Determination of Torch Plasma Spectra

In order to measure a large bandwidth spectrum of an arc plasma torch using the monochromator or Black Comet, the arc produced ideally should be consistently and continuously produced. The current procedure involves cutting the piece from below. As the torch arc formed, the metal piece was pushed forward while holding the torch steady using the setup seen in Figure 3.29. Using the fibre optic cable setup, spectral recordings can took place while the cut was being made [67]. This is sketched in Figure 3.35, the sample being cut has contaminants glued to it. The contaminants are liberated by the plasma and react within. The light from the excitation reactions that occur (from the air or contaminants) in the plasma were captured by the fibre optic cable and are measured spectrometer.

Preparation of Contaminated Sheet Metal Samples

The sample mock-contaminants used in this work were cesium iodide, and potassium iodide. Potassium iodide was used in earlier experiments due to the fact that experiments with cesium iodide would cause releases of cesium (a heavy metal) into the air. The contaminants were glued to the surface of the metal samples using Foam Glue manufactured by Bob Smith Industries following an outlined procedure [68]. The foam glue, according to the manufacturer, contains primarily silicon and some organic alcohols (carbon, hydrogen, oxygen). This information is useful for the spectroscopic analysis in later chapters in case any of the emission lines are detected in the spectra. Figure 3.36 shows contaminant salt grains (potassium iodide or cesium iodide) glued to the surface of the metal sample that is to be cut.

Cutting of Contaminated Sheet Metal

Once a baseline spectrum was obtained, a second experiment involving cutting a contaminated metal sample was done by taking the spectral measurements of the plasma arc produced when the contaminated metal is cut, using a similar method as described previously [67]. It was assumed that the contaminants will mix into the plasma and traces of the contaminants would appear as peaks in the spectrum. Samples were cut using setups like in Figures 3.29 and 3.30.

3.6 Methods of Spectral Analysis

Emission spectroscopy was used as a method of analysis due the known methods of temperature measurement in the form of Saha Plots and Doppler broadening, as well as the ability to identify atomic species from their emissions. It is known from the literature that the pattern of emission lines produced by atomic species can be used for their identification. In this work, argon and air plasmas are produced. Additionally, cesium iodide salts are introduced to both plasmas. Cesium and iodine have known emission lines for their neutral and ionic species. The species may be identified by emission spectroscopy, if the intensity of the emission lines are sufficiently high to be distinguished from the "background" spectra.

The spectroscopy systems are computer-controlled. The procedures outline how to use the software that control them, and how to properly store/save the files are outlined in an internal document [54]. The software used to control the Monochromator is the proprietary AD131 software readily available from the Spectral Products website. The Black Comet is controlled by the proprietary SpectraWiz software.

For both the DK480 Monochromator and the Black Comet time series measurements and spectral measurements can be obtained. The monochromator can track the intensity of a single wavelength down to millisecond intervals, while the Black Comet can track the entire spectra at a minimum of around 100 millisecond intervals.

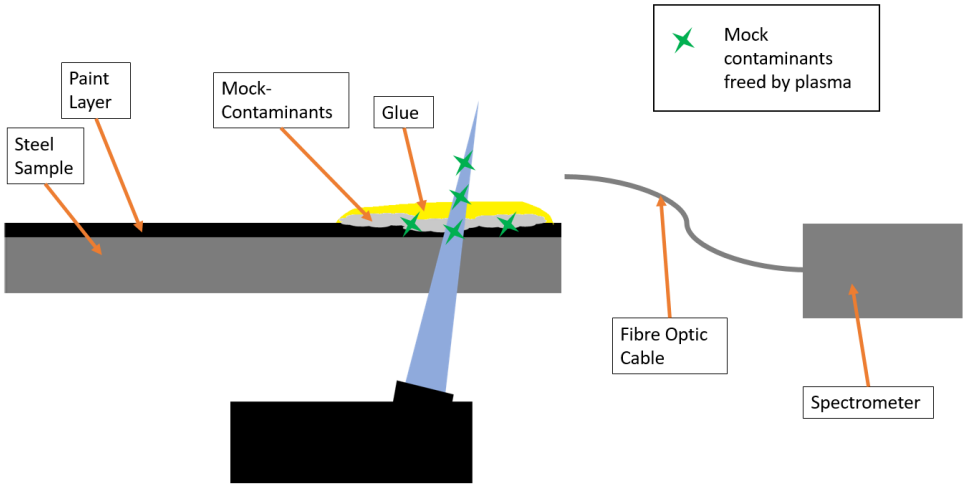

FIGURE 3.35: Fibre optic cable measurement of the cutting of a contaminated sample. Measurement of the baseline torch plasma spectrum occurs with this same method, but without contaminants glued to the sample.

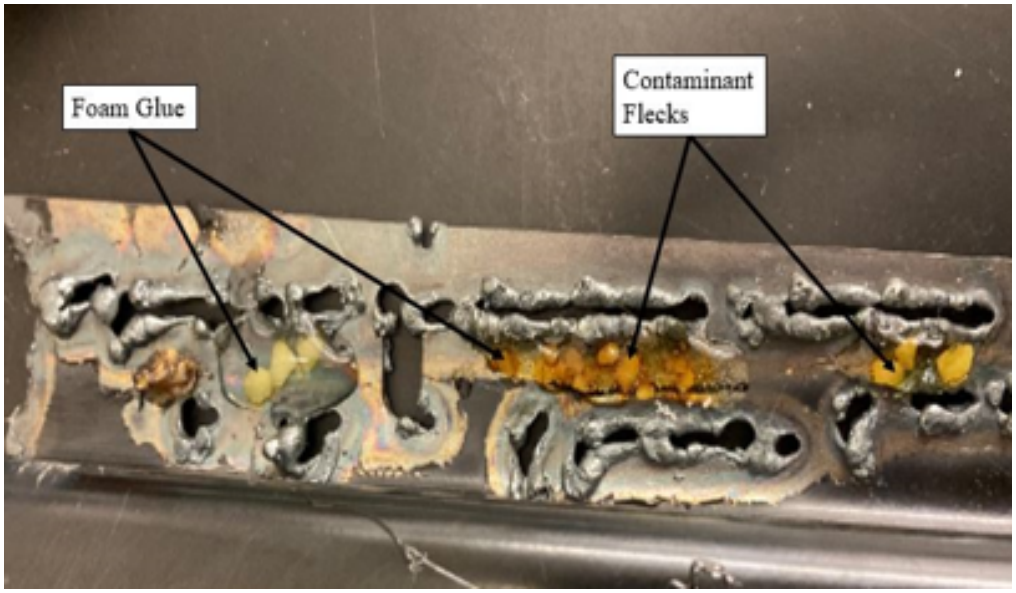

FIGURE 3.36: Glued on contaminants to metal sample. The embedded salt grains may be potassium iodide or cesium iodide.

The monochromator user manual generated for the purposes of this work outlines how to generate both time series measurements as well as spectral measurements, along with guidelines on the control of other spectral acquisition settings [54].

3.6.1 Spectroscopic Methods of Temperature Measurement

There are two methods to calculate temperature values using spectral data that are explored in this work. The methods are effectively independent of one another, in the sense that the temperature values are obtained from different physical mechanisms. The Saha-Boltzmann plots use the relative representation of multiple emission lines in a single species contained in a plasma to infer the temperature. The Doppler Broadening method derives a temperature value from the extent that the Doppler Effect broadens a single emission line, by isolating the Doppler contribution from other sources of line broadening.

Saha-Boltzmann Plot

The Saha-Boltzmann plot method was used in this work due to the fact that it can transform the relative intensity of emission lines into temperature values. This section is derived in combination from from Ohno et al. [69] and the Spectroscopy Handbook of the NIST Atomic Spectra Database [37]. Many of the emission line lists consulted in order to identify lines useful for Saha Plots are featured in Appendix A.

The density of a population of energy states in a single species plasma at thermal equilibrium can be described by Boltzmann statistics. This implicitly assumes that the plasma, including the neutral atoms and those in excited states, are at equilibrium, or at least local thermodynamic equilibrium in the region from which light is being collected [69].

Equation 3.2 describes the ratio of an excited atomic state in a plasma of energy E_2, where n_2 is the density of the excited state, g_2 is the state's degeneracy, n is the total density of all of the species, T is the system's temperature, $Z(T)$ is the partition function of the plasma, and k_B is Boltzmann's constant.

$$\frac{n_2}{n} = \frac{g_2}{Z(T)} \exp\left(-\frac{E_2}{k_B T}\right) \tag{3.2}$$

For the relative densities between two states 1 and 2, Equation 3.2 can be solved twice for densities n_1 and n_2, and then substituted into one another:

$$\frac{n_2}{n_1} = \frac{g_2}{g_1} \exp\left(-\frac{E_2 - E_1}{k_B T}\right) \tag{3.3}$$

Suppose that an electronic transition were to occurs from state 2 to state 1. Assuming state 2 is at a higher energy, a photon of energy $\Delta E = E_2 - E_1$ would be emitted. The photon would have a frequency of $\frac{\Delta E}{h}$ and a wavelength of $\frac{hc}{\Delta E}$, where h is the Planck constant. These photons of specific wavelengths produce the spectrum of the plasma. Transitions from one state to another occur at different probabilities, producing spectra with lines of different relative intensities. The intensity I of emission lines emitted from an optically thin plasma can be expressed as a function of the photon energy $\frac{hc}{\lambda}$, transition probability from state 2 to state 1 $A_{1,2}$, density of the upper excited state n_2, and the characteristic length of the plasma L [37]. This is expressed in Equation 3.4.

$$I = \frac{1}{4\pi} \frac{hc}{\lambda} n_2 A_{1,2} L \tag{3.4}$$

Solving for the density of the upper excited state n_2, Equation 3.5 is obtained.

$$n_2 = \frac{4\pi I \lambda}{hc A_{1,2} L} \tag{3.5}$$

substituting Equation 3.4 into Equation 3.2 and re-arranging:

$$\frac{I\lambda}{A_{1,2} g_2} = \frac{hcLn}{4\pi Z} \exp\left(\frac{E_2}{k_B T}\right) \tag{3.6}$$

Taking a logarithm of both sides, the following is obtained:

$$\log\left(\frac{I\lambda}{A_{1,2} g_2}\right) = \log\left(\frac{hcLn}{4\pi Z}\right) - \frac{E_2}{k_B T} \tag{3.7}$$

This equation, provided the assumptions are correct, should produce a linear scatter plot of $\log\left(\frac{I\lambda}{A_{1,2}g_2}\right)$ as a function of E_2. All constants in the former are known within uncertainty, and are accessible on the NIST atomic spectra database [37]. The intercept $\log\left(\frac{hcLn}{4\pi Z}\right)$ is constant across samplings of different emission lines [69].

This is referred to as a Saha-Boltzmann plot, or a Saha plot for short. Fitting a line to the scatter plot that is produced should have a slope of $-\frac{1}{k_B T}$. The temperature can then be extracted from the value of the slope. Appendix B provides an outline of how these Saha plots are produced from raw spectral data. This is done by analyzing Intensity vs. Wavelength plots (emission spectra) in order to find emission lines and their intensities, processing the intensities values into Saha plots, and finally processing the Saha plots into Temperature values. Saha plots were used for pure argon plasma experiments, and attempted for the calculation of the plasma torch temperature.

Doppler Broadening Method

Doppler broadening is the smearing out of emission lines from the unidirectional motion of atoms in a plasma. The smearing grows as the atoms grow hotter, as their root-mean-squared velocity increases. This broadening takes the form of a Gaussian curve [70]. This broadening is described in terms of the FWHM of the curve. It can be directly related to the width (standard deviation) of a Gaussian distribution. The FWHM is a function of the temperature, as seen in Equation 3.8.

$$\Delta\lambda_D = 7.16 \times 10^{-7}\lambda\left(\frac{T}{\mu}\right)^{\frac{1}{2}} \tag{3.8}$$

Temperature is described by variable T, μ is the atomic mass of the plasma gas in atomic mass units, λ is the wavelength of the peak, and $\Delta\lambda_D$ is the FWHM contribution to the line shape due to Doppler broadening. Both wavelength terms are in units of nanometres.

As seen in Equation 3.8, the expected Doppler broadening contributions can be calculated for an emission line of known wavelength from a species of known

molar mass. Figure 3.37 shows the expected Doppler broadening contribution as a function of temperature for various argon emission lines.

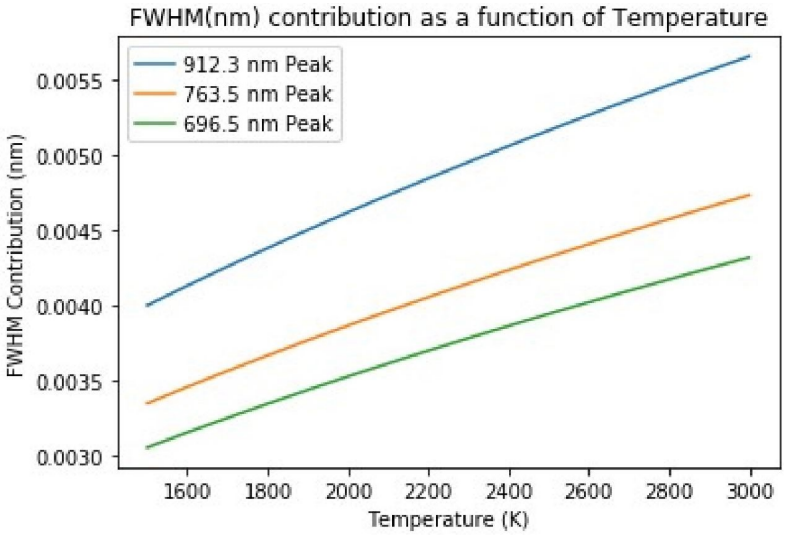

FIGURE 3.37: Plot of projected Doppler Broadening contributions to emission line shape.

In order to measure line Doppler broadening, the spectroscopy setup must be able to resolve peak widths (using numerical fitting techniques) on the order of 0.004 nm. Part of this work involves investigating whether the usage of this method is viable with the spectrometer and experimental setups used. The instrument error has to be sufficiently small to distinguish between it and an increase in overall FWHM of a measured peak from a change in Doppler broadening as temperature increases or decreases. The predicted values of Doppler broadening measurements are low in comparison to the specified (0.01 nm) resolution of the spectroscopy systems. This method of determining temperature requires isolating the Doppler broadening contribution from the spectrum measured of an individual peak [70].

An individual emission line has multiple sources of broadening, as discussed in the previous chapter. For the microwave plasma, it was assumed that the two sources of broadening are the instrument error and the Doppler broadening contribution. The natural broadening source was taken to be negligible. The total broadening of an emission line for the purposes of this work can be expressed in Equation 3.9 [70].

$$(\Delta\lambda_{total})^2 = (\Delta\lambda_D)^2 + (\Delta\lambda_{instrument})^2 \tag{3.9}$$

Where $\Delta\lambda_{instrument}$ is the broadening source from the instrument that measures the spectrum. All of these values are expressed as a FWHM. This equation implicitly assumes only two sources of broadening, the instrument error, and the Doppler broadening due to the species having a definable temperature in the plasma.

To isolate the Doppler broadening term from equation 3.9, the instrument error is first determined by calculating the FWHM of stronger peaks of a colder stable source. Recall that the Doppler broadening contribution is proportional to the square root of the temperature, and inversely proportional to the square root of the molar mass of the atom in question. The emission line from a source with a large molar mass and a low temperature is ideal. In our case, the instrument error could be determined using the HG-2 or AR-2 lamps [70]. The measurement of instrument error is intended to be done using thin entrance and exit slit width settings on the monochromator to minimize uncertainty. It will be seen in a later chapter that thin slit widths are essential for this calculation to be possible, if it is at all feasible.

With the same slit width settings used to determine the instrument error, the spectrum around an experimental plasma emission line can then be taken to calculate its temperature. The FWHM of the emission line can be calculated using a non-linear fit. The fit function in this case would be a Gaussian distribution [70]. There is no single best peak for this purpose. Instead a selection of peaks may be used. The peaks that are chosen should have a high peak intensity (which is determined by observation), as well a large wavelength value. The Doppler contribution to the peak profile is directly proportional to the wavelength value. A high intensity peak is chosen as the FWHM can be calculated to a higher certainty when a Gaussian fit is performed.

3.7 Outline of Tasks and Experiments Performed to Fulfill Thesis Goals

To fulfill the goals of this thesis, the procedures and methods developed in previous sections were put to use. Tables 3.4 and 3.5 outline the experiments and methods used in order to complete the experiments. Included are the objectives that the tasks partially fulfill along with the procedures and methods used.

3.7.1 Experiment and test matrices

Tables 3.6 to 3.8 feature test matrices for experiments performed with the argon plasma experiments and torch plasma experiments. Table 3.6 outlines the test conditions performed to characterize the un-contaminated argon plasma. All argon plasma experiments that were performed with cesium iodide contaminants had argon gas flow rates adjusted to always be 2.5 $\frac{L}{min}$. The test matrix for all cesium iodide-contaminated argon experiments is featured in Table 3.7. All plasma torch experiments had the current limit settings on the power supply set to 12.5 A. The air compressor pressure was always set to 50 PSI or 345 kPa. Table 3.8 outlines the test matrix for all plasma torch experiments.

TABLE 3.4: Table of tasks and experiments performed to characterize microwave system, argon plasma production using the microwave system, and the spectroscopic methods used to identify emission lines and plasma temperature.

Tasks & Experiments	**Relevant thesis objective**	**Relevant methods, procedures, and manuals**	**Systems used**	**Databases used**
Microwave system start-up	1	Procedures 3, 4, and MWP-PRO-5	Microwave system with chilled water load	
Microwave system testing and power coupler calibration	1	Procedures 3, 4, 6, RCT-PRO-5, and Appendix D	Microwave System with chilled water load	
Construction of quartz tube test sections	1,3,4	Procedure 8		
Calibration of DK480 monochromator and Black Comet spectrometer	3	Spectrometer system user manual	AR-2 and HG-2 calibration lamps, DK480, and Black Comet	
Argon plasma production at a single input microwave power level	2,3	Procedures 3, 4, 7, and 8	Microwave system with field applicator + test section	
Testing stub tuner settings for argon plasma production	1,2	Procedures 3, 4, 7, and 8	Microwave system with field applicator + test section and DK480	NIST ASD
Argon plasma production at multiple input microwave power levels	3,4	Procedures 3, 4, 7, 8, and 10	Microwave system with field applicator + test section	
Argon plasma jet height characterization	1,3	Procedures 3, 4, 7, 8, and 9	Microwave system with field applicator + test section	
Spectroscopic measurements of argon plasma	1,3	Procedures 3, 4, 7, 8, 9, Appendix A, spectrometer system user manual	Microwave system with field applicator + test section, DK480 and Black Comet	NIST ASD, NIST Strong Lines database
Saha plot temperature calculations	2,3	Chapter 2, Appendices A & B		NIST ASD
Production of argon plasma with cesium iodide contaminants introduced into test section	4	Procedures 3, 4, 7, 8, 11, 12, and Spectrometer System User Manual	Microwave system with field applicator, test section, and Black Comet	NIST Strong Lines database

TABLE 3.5: Table of tasks and experiments performed to characterize the introduction of mock-contaminants into the argon plasma, the baseline of the plasma torch, and the introduction of mock-contaminants to sheet metal samples cut by the plasma torch.

Tasks & Experiments	**Relevant thesis objective**	**Relevant methods, procedures, and manuals**	**Systems used**	**Databases used**
Construction of test section containing cesium iodide contaminants	4	Procedure 8		
Production of argon plasma with cesium iodide contaminants introduced into test section at multiple input microwave power levels	4	Procedures 3, 4, 7, 8, 11, 12, and Spectrometer system user manual	Microwave System with field applicator, test section, and Black Comet	NIST Strong Lines database
Sheet metal cuts with plasma torch	2,5	Procedure 13	Tomahawk 375 Plasma Torch	
Measurement of torch plasma spectral baseline	2,5	Procedure 13	Tomahawk 375 Plasma Torch, DK480, and Black Comet	
Production of "contaminated" sheet metal samples	5	Procedure 14	Tomahawk 375 Plasma Torch and Black Comet	
Cutting of contaminated sheet metal samples with spectroscopic acquisition	5	Procedure 13	Tomahawk 375 Plasma Torch and Black Comet	
Analysis of baseline and contaminated spectra produced by plasma torch	5	Chapter 4, Appendices A & B		NIST ASD, NIST Strong Lines database

TABLE 3.6: Test matrix for pure argon plasma experiments and characterization. Table generated from procedures [58–65, 71].

Testing	Argon Flow Rate (L/m)	Tuning Settings (mm, mm, mm)	Input Microwave Power (W) (in the listed order)
Initial Plasma Ignition Testing	2.5	(0,0,0)	280
Testing "optimal" tuning setting	2.5	Varied	280
Tuning Effects Experiment	2.5	(7,9,9) (7, 9, 4.5) (7, 9, 0) (7, 9, 13.5) (7, 9, 18) (7, 4.5 , 9) (7,0 ,9) (7, 13.5, 9) (7, 18 ,9)	280
Argon Plasma Jet Height Characterization (every combination of flow rate and input power)	2.0, 2.5, 3.0.	(7,9,9)	219 263 306 349 392 435 478
Argon Plasma Saha Plot Temperature as a function of Input Power	2.5	(7,9,9)	219 306 392 478 392 306 219

TABLE 3.7: Test matrix for cesium iodide-contaminated argon plasma experiments and characterization. Table generated from procedures 10 and 11 [65, 66].

Testing	Mass of cesium iodide contaminants	Tuning settings	Input microwave power (W)
Initial test ignitions	0.15 g (each)	(7,9,9)	190
Testing CsI + argon plasma ignition and production at constant power	0.15-0.17 g (each)	(7,9,9)	190, 306
Testing CsI + argon plasma response to changes in input microwave power	0.15 g	(7,9,9)	219 306 392 478

TABLE 3.8: Test matrix for plasma torch experiments and characterization. Table generated from procedures 13 and 14 [67, 68].

Testing	Contaminants Used
Measuring baseline spectrum of plasma torch	None
Measuring spectrum of plasma torch spectrum when cutting potassium iodide contaminants	Potassium iodide + Bob Smith Industries Glue
Measuring spectrum of plasma torch spectrum when cutting cesium iodide contaminants	Cesium iodide + Bob Smith Industries Glue

Chapter 4

Results and Analysis

4.1 Introduction

This chapter provides the experimental results obtained to address the objectives of this work. First, the results for the microwave generated plasma with no added contaminants will be discussed to characterize the baseline data. This will include an assessment of the impact of the microwave control system and other parameters on the plasma performance. Then the results for additives within the plasma will be presented. The plasma torch experiments will be also discussed. Observations on how the cuts took place will be presented, along with the spectroscopic measurements of the different experimental cuts in order to gauge whether surface contaminants are detectable in the torch plasma.

4.2 Argon Plasma Characterization

This section describes the observations made during the experiments involving the production of argon plasma inside the microwave plasma system. The section begins with an overview of the spectral measurements as well as its identified emission lines, an assortment of qualitative observations made of the experiment and of plasma behaviour. It ends with the creation and analysis of Saha Plots of the spectroscopic measurements, which associates a temperature value with the plasmas produced.

Argon plasma ignition began when the magnetron was prompted to start microwave output. The plasma would rapidly ignite and appear as a jet, typically

of a purple colour. Figure 4.1 features multiple photos of argon plasmas. The shift in colour as power increases (from left to right in the figure) indicates a change in excited species, which also is known to indicate a shift in temperature. The shift from a "redder" plasma to a violet plasma suggests an increase in temperature. According to Boltzmann statistics, the temperature for a plasma at equilibrium means that higher energy states are represented more. These higher energy states, when they decay, will produce higher energy photons at a higher probability. This results in more of the "blue" and "violet" colours being produced by the plasmas. Images A through C of Figure 4.1 consist of plasmas from separate experiments whose input powers progress from the neighborhood of $150W$ to the neighborhood of $500W$ in image C. Image B would be in the neighborhood of $200W$.

4.2.1 Spectroscopic Measurements

The DK-480 was primarily used in the measurement of the spectra produced by the argon plasmas that were produced in the microwave system. Figure 4.2 features a typical spectrum measured using the DK-480 monochromator. Often times the absolute intensity scale makes spectra difficult to distinguish from one-another visually.

Figure 4.3 uses a logarithmic scale. Many of the fainter peaks, especially those below 100 counts, become visible on this scale. This scale facilitates the identification of peaks.

Black Comet Measurement

Figure 4.4 shows a spectrum of the argon plasma held at 190 W input power as measured by the Black Comet.

Identification of Lines

The NIST database provides estimates for relative intensity of lines that are persistent or strong.

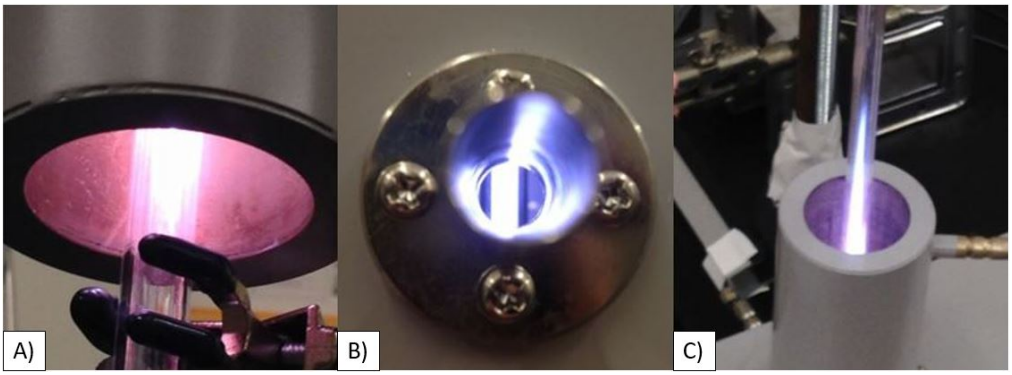

FIGURE 4.1: Images of various colours of argon plasma as produced in the field applicator when microwaves are applied. The test sections are different for each plasma, but have the same inner diameter: 7 mm.

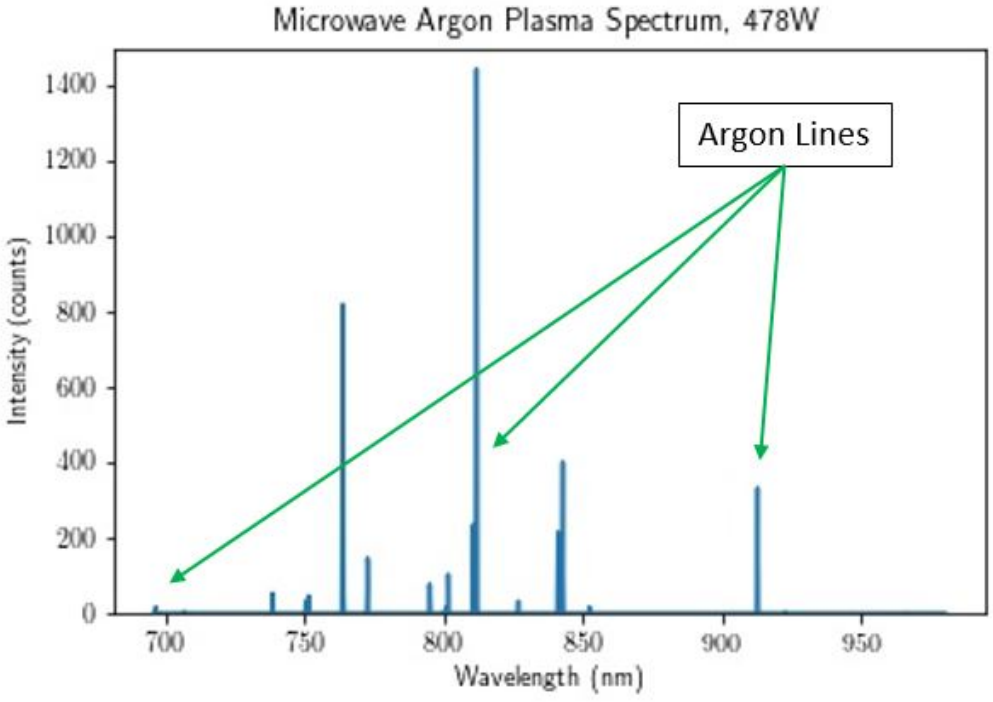

FIGURE 4.2: Typical spectrum produced by DK-480 monochromator. Monochromator does not detect lines in any other wavelength ranges.

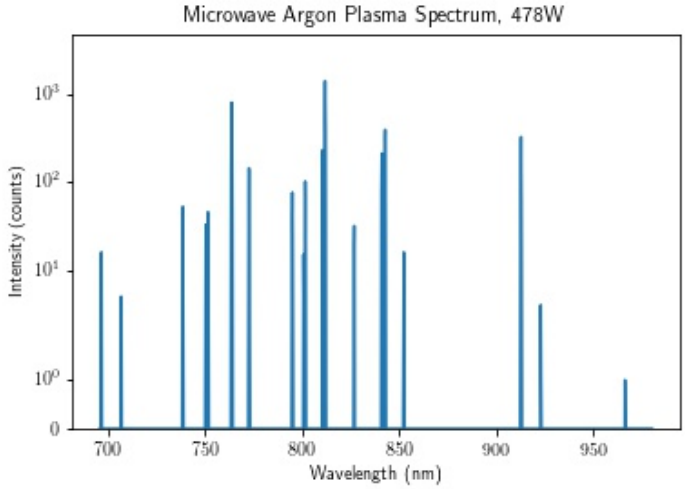

FIGURE 4.3: Log-scale spectrum of Figure 4.2. The log-scale of intensity makes peaks across multiple orders of magnitude of intensity visible.

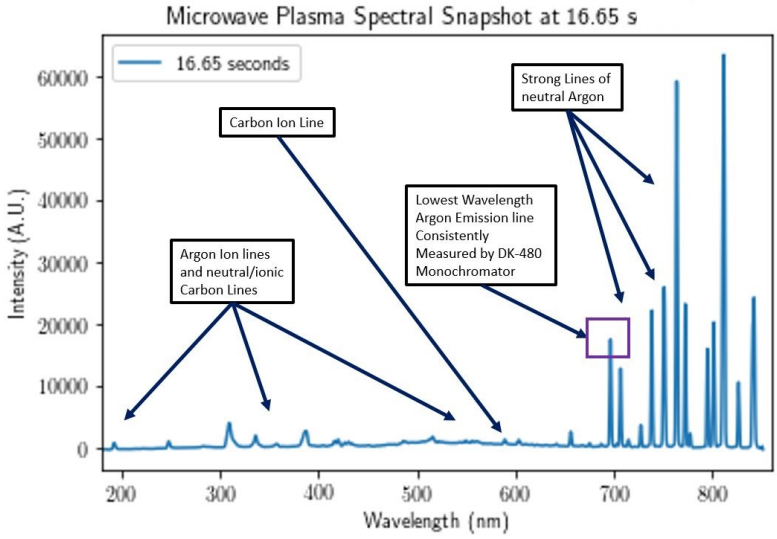

FIGURE 4.4: Spectrum measured by Black Comet for an argon plasma at 190W input power. Spectrum shows the entire wavelength range of the instrument.

These numerical values often confirm the emission lines being detected. Sometimes there are multiple emission lines being resolved as one peak, due to the proximity of emission lines. Appendix B outlines how the emission lines were identified using the "raw" intensity vs wavelength data that the spectrometers can produce. Tables 4.1 and 4.2 compile the emission lines observed during the course of the experiments performed in this work. The Black Comet was used to probe the shorter wavelength region of the spectrum. The purpose of identifying lines was partially to confirm that the plasma was indeed an argon plasma. In addition to detecting all the lines observed by the monochromator, it is also capable of observing lines in the 309 nm to 425 nm range. The species of excited atom in Tables 4.1 and 4.2 are also associated with each line based on a number that appears after it, following the NIST database conventions. Fainter lines, like the 728 nm line, were visible on the monochromator, but only at higher values of input microwave power. It is noted that there are several emission lines measured in the region of these tables that cannot be distinguished from one another. The two 810 nm lines and the 772.3 nm lines cannot be resolved using the monochromator at the settings used in these experiments. These emission lines cannot be used for temperature calculation methods such as the Saha plots and are left out of the plot, but still remain tabulated as "observed peaks" as a group entry. The emission lines of argon identified in these tables are the "Strong Lines" identified by the NIST database (Appendix A), which are also the high relative intensity lines (over 2000) that are identified in the "Detailed Lines List" (also Appendix A). These emission line list tables provide a baseline expectation of what an argon plasma spectrum should consist of in later experiments of this thesis. This result proves useful when additional contaminant species are introduced. The regions where argon lines do not appear, or regions where the lines are expected to have a low relative intensity, are regions where lines formed by the contaminants may be observable without interference from the strong argon lines. The region between 425 nm and 696 nm is such a region.

TABLE 4.1: Compilation of emission lines detected from argon plasma experiments using monochromator and Black Comet for emissions of 738 nm and below. The term "multiple" refers to the fact that multiple emission lines are attributed to a single peak.

Approx. Peak Wavelength (± 1 nm depending on instrument)	Species	Wavelength (nm) from NIST Database	Visible with Black Comet?	Visible with DK-480?	Comments
284	Carbon II	283.7	Y	N	
309	Argon II	309.3	Y	N	Strong line
338	Argon II	337.6	Y	N	
357	Argon II	Multiple	Y	N	Multiple lines from 354 nm to 356 nm
405	Argon II	404.3	Y	N	
415	Carbon I	Multiple	Y	N	Two emission lines
421	Carbon I	Multiple	Y	N	Five emission lines
426	Carbon I and/or Argon II	Multiple	Y	N	Multiple lines
433.5	Argon II	434.8	Y	N	
489	Argon II	487.9	Y	N	
517	Carbon I	Multiple	Y	N	Faint: Multiple Carbon Lines
555	Carbon I	Multiple	Y	N	Faint: Multiple Carbon Lines
562	Carbon I	Multiple	Y	N	Faint: Multiple Carbon Lines
590	Carbon I and Carbon II	Multiple	Y	Varies	Consistently measurable by Black Comet, DK-480 may measure it depending on the experiment.
697	Argon I	696.5431	Y	Y	
707	Argon I	706.8736	Y	Y	
729	Argon I	728.2936	Y	Y	
738	Argon I	738.3980	Y	Y	

TABLE 4.2: Compilation of Emission lines detected from argon plasma experiments using monochromator and Black Comet for emissions of 750 nm and above. Lower input powers would be on the order of 190 W and below.

Approx. Peak Wavelength (± 1 nm depending on instrument)	Species	Wavelength (nm) from NIST Database	Visible with Black Comet?	Visible with DK-480?	Comments
750	Argon I	750.5153	Y	Y	
755	Argon I	754.4652	Y	Y	
764	Argon I	763.5106	Y	Y	
773	Argon I	722.3761	Y	Y	Line merges with 722.4207 nm line
773	Argon I	722.4207	Y	Y	Line merges with 722.3761 nm line
795	Argon I	794.8176	Y	Y	
801	Argon I	800.6157	Y	Y	
802	Argon I	801.4786	Y	Y	
811	Argon I	810.3693	Y	Y	Merges with 810.36931 nm line
811	Argon II	810.36931	Y	Y	Merges with 810.3693 nm line
812	Argon I	811.5311	Y	Y	
841	Argon I	840.8210	Y	Y	
843	Argon I	842.4648	Y	Y	
852	Argon I	852.1442	Y	Y	
868	Argon I	867.7944	Y	Varies	Not visible for lower input microwave powers
912	Argon I	912.2967	Y	Y	
923	Argon I	922.4499	Y	Y	
936	Argon I	935.4220	Y	Varies	Not visible for lower input microwave powers
966	Argon I	965.7786	Y	Y	Not visible for lower input microwave powers

4.2.2 Analysis of Spectroscopic Measurements

This section describes spectroscopic measurements made throughout the argon plasma production experiments performed in this work. An outline of how the raw spectroscopic data is interpreted and processed to obtain values such as plasma temperature is featured in Appendix B.

Comparison of Spectra Produced by Spectrometers

Figure 4.5 compares broadband spectral measurements from both instruments. The spectra were taken from both view-ports of the field applicator. With this in mind, it would be expected that the relative intensities from both spectrometers would be the same. This is not the case: note the difference between relative intensities of spectra measured by the instrument. For this work, the monochromator measurements are taken as being more representative, as the instrument's resolution is superior to that of the Black Comet.

Saha Temperature Method

This section describes the usage of the Saha Plot method to calculate the temperature of an argon plasma produced in the microwave system.The data set is from an experiment that produced argon plasma for mulltiple input power levels. The microwave power was held at a selection of input power steps from 219 W to 478 W and back in steps. The power values were held at the same values on the way down as it was on the way up to the maximum. Monochromator scans from 696 nm to 980 nm were performed for each hold on microwave power. This was the wavelength region is where the strong intensity lines are observed. The emission lines and their peak intensities were identified in these scans and then transformed into Saha Plots, which provided a temperature value for each power step. Appendix B provides a guide on how to transform the identified emission lines in the spectrum into saha plots.

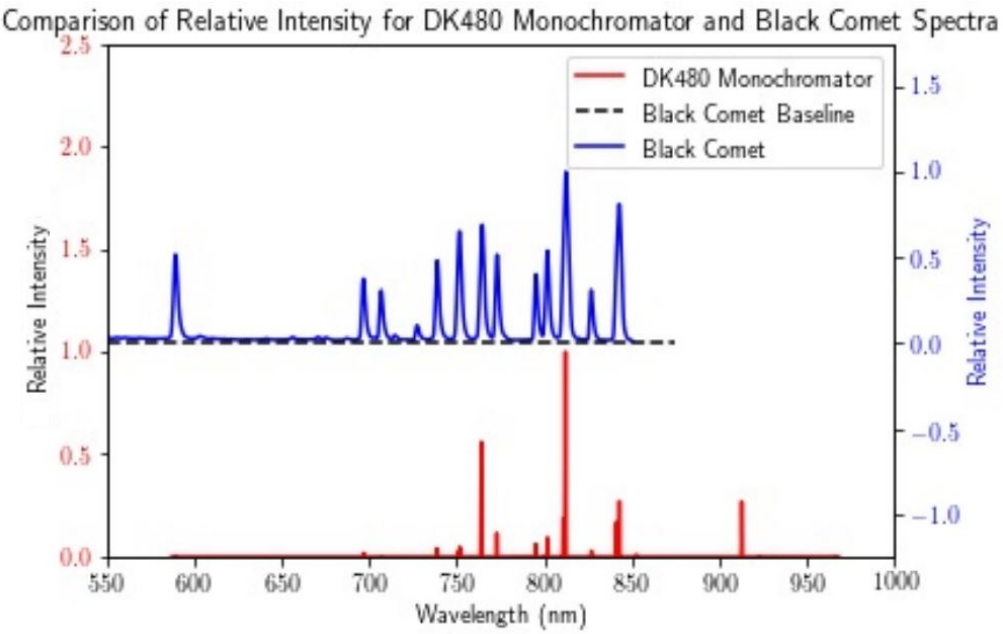

FIGURE 4.5: Comparison of Monochromator (left) and Black Comet spectra (right) for the same plasma. Relative intensity scales are used to facilitate comparison of different relative peak intensities from each instrument, as well as the width of peaks measured in the spectra.

Figure 4.6 showcases two spectra and their respective Saha plots. Appendix B outlines the calculations used to associate an error with each point in the Saha plot. Note that the usage of the weighted fit allows for high uncertainty outliers to be effectively "ignored" by the fit.

Figure 4.7 and Table 4.3 summarize the temperature values obtained from all Saha plots. It is noted here that most temperatures are statistically the same, except for the points #2 and #6.

The temperature values and uncertainties associated with the Saha plots from Figures 4.6 and 4.7 are also tabulated in Table 4.3. Overall, it is suggested that once the plasma is ignited, the temperature does not appear to change with additional input power.

Comparison of Line Intensities at Multiple Input Powers

Figure 4.8 compares the plasma (same experiment from 219 W to 478 W) at the minimum initial low power, at its maximum input power, and at the minimum input power that was returned to before the experiment was shut down. Most peaks that appear in the spectrum at the maximum power of 480W. Figure 4.8 features linear scale spectra on the left, with their log-scale plots on the right. The log scale plots are useful because they demonstrate the overall increase in intensity of each line with power. They also make visible the fainter lines as well as their changes in intensity. Figure 4.9 compares the intensities of argon emission lines for the experiment as a function of input power. Here, a hysteresis effect is noticeable. The intensities tend to increase with input microwave power. As the input powers fall, the intensities do not reach their initial value, but tend to "plateau" above the intensity value that they initially started at. These lines in particular are those whose final excited states are metastable states of argon.

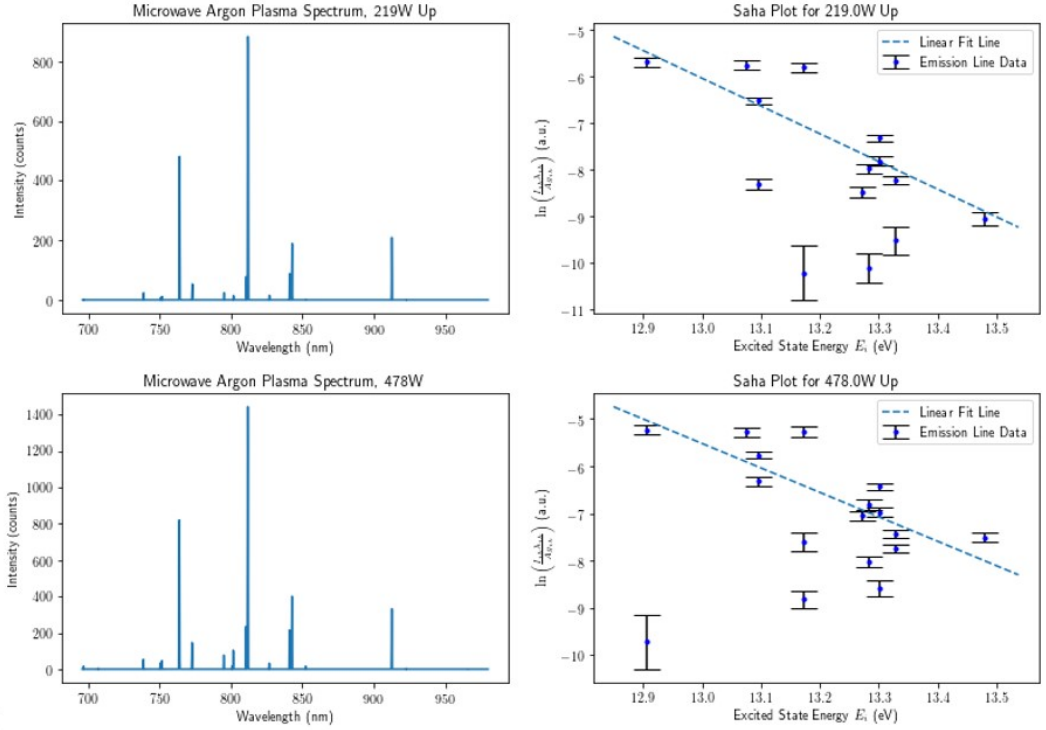

FIGURE 4.6: Sample Saha plots for 219W and 478W input power argon plasmas. Note the range of the independent variable, the excited state energy E_i. The Saha plots produce temperature values of $2000 \pm 500\,\mathrm{K}$ and $2200 \pm 600\,\mathrm{K}$ respectively.

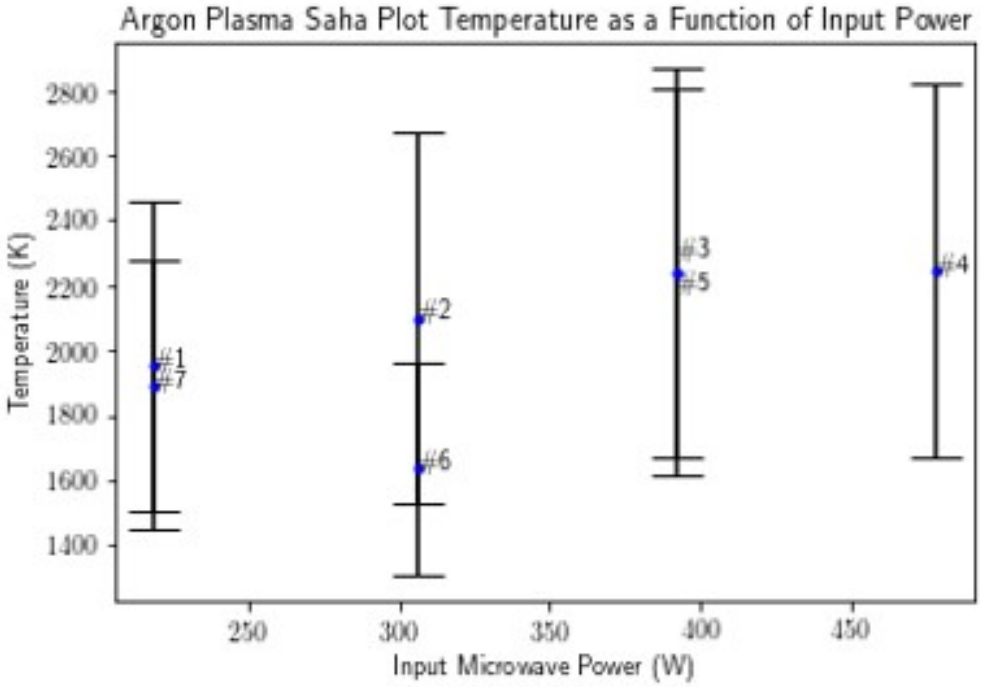

FIGURE 4.7: Argon plasma Saha plot temperature as a function of input power.

TABLE 4.3: Table of argon plasma temperatures and uncertainties.

Input Power Setting	Temperature (K)	Uncertainty in Temperature (K)
1. 219 W (UP)	2000	500
2. 306 W (UP)	2100	600
3. 392 W (UP)	2300	600
4. 478 W	2200	600
5. 392 W (DOWN)	2200	600
6. 306 W (DOWN)	1600	300
7. 219 W (DOWN)	1900	400

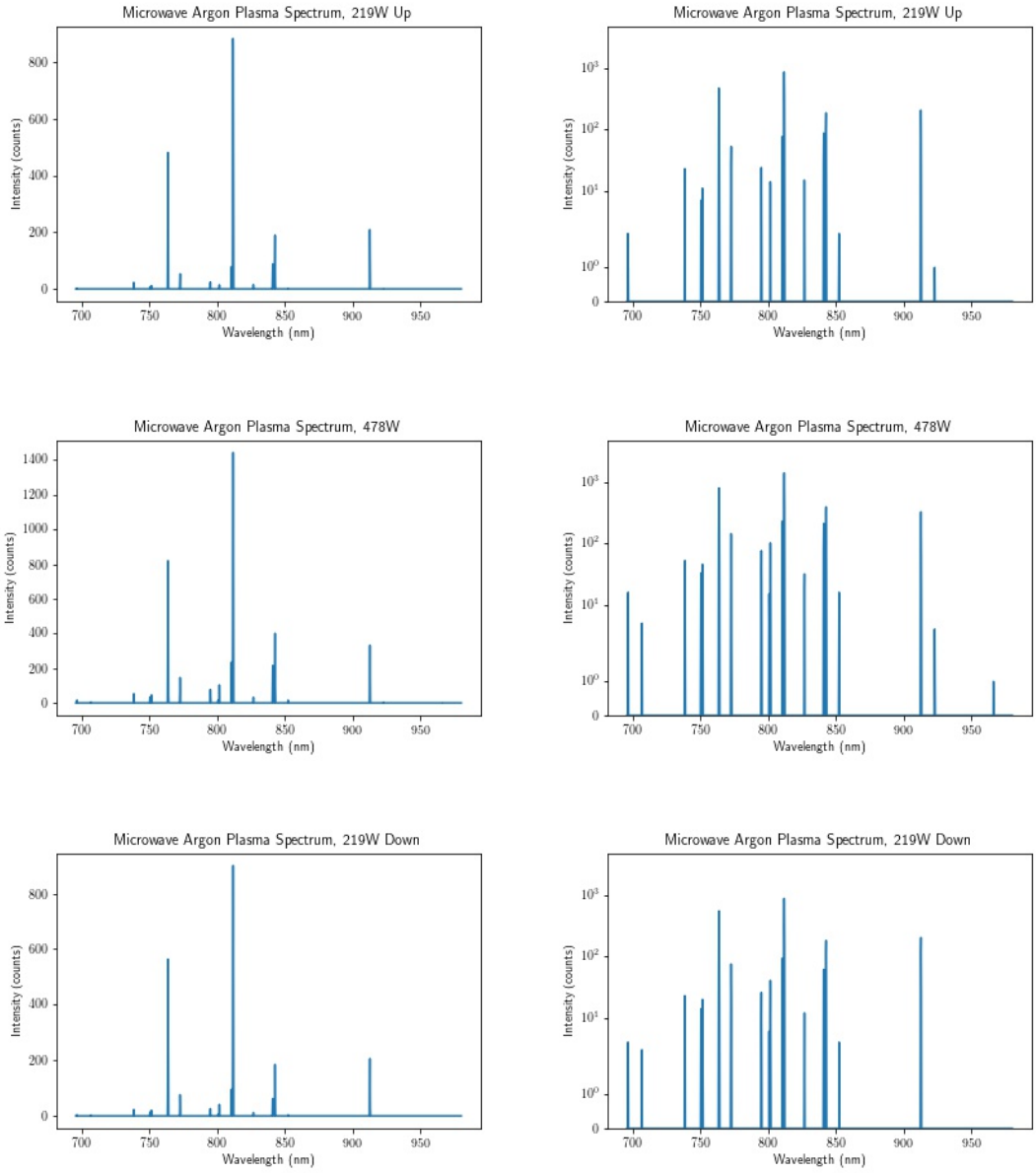

FIGURE 4.8: Comparison of linear and log scale spectra of argon plasmas for input power values of 190W (upward direction), 480W, and 190W(downward direction). Wavelength-Intensity data points were taken in steps of 0.1 nm. All spectra taken from the same experiment.

Characterization of Monochromator Resolution

The effects of slit width changes on the quality of spectral data produced by the DK480 monochromator provided a feasibility test for the alternate temperature measurement method: the measurement of Doppler Broadening.

A single individual argon emission line from an argon plasma was measured with multiple slit settings, with microwave power held constant. As a result, any changes in the spectrum could be assumed to be due to changes in the monochromator slits, assuming the plasma did not evolve over time. The 912.3 nm line was observed as it was measured to have a high intensity. Figure 4.10 contrasts the emission line measurement of the argon plasma for two different slit widths.

The slit width, within the range of 100 µm to 1000 µm, has an effect on the intensity and quality of the measured peaks. There is a trade-off between peak intensity and slit width. Keep in mind that the spectroscopy measurements record intensity in integer values only. A Gaussian fit was performed on the spectral data in order to calculate the full-width-half-maximums of the peaks. Figures 4.11 and 4.12 plot the peak amplitudes and FWHM of the emission lines, which were obtained by fitting the peaks to a Gaussian curve. It is acknowledged from Figure 4.10 that the FWHM values obtained from Gaussian fits are an estimate due to the spectral profiles not always being Gaussian in shape. These figures were done with a single trial.

The amplitude and FWHM curves decay to zero as the slit widths approach zero. The trade-off between small FWHM and intensity that is observed in these plots makes the use of the monochromator for Doppler Broadening measurements of argon species unviable with these settings, as the lowest measured value of FWHM, roughly 0.07 nm, is greater than expected broadening contribution of $0.005nm$. In short, the thin slit width required to measure a small enough peak broadening (the trade-off) to a high enough certainty would result in not enough light from the plasma to entering the monochromator to produce a non-zero reading.

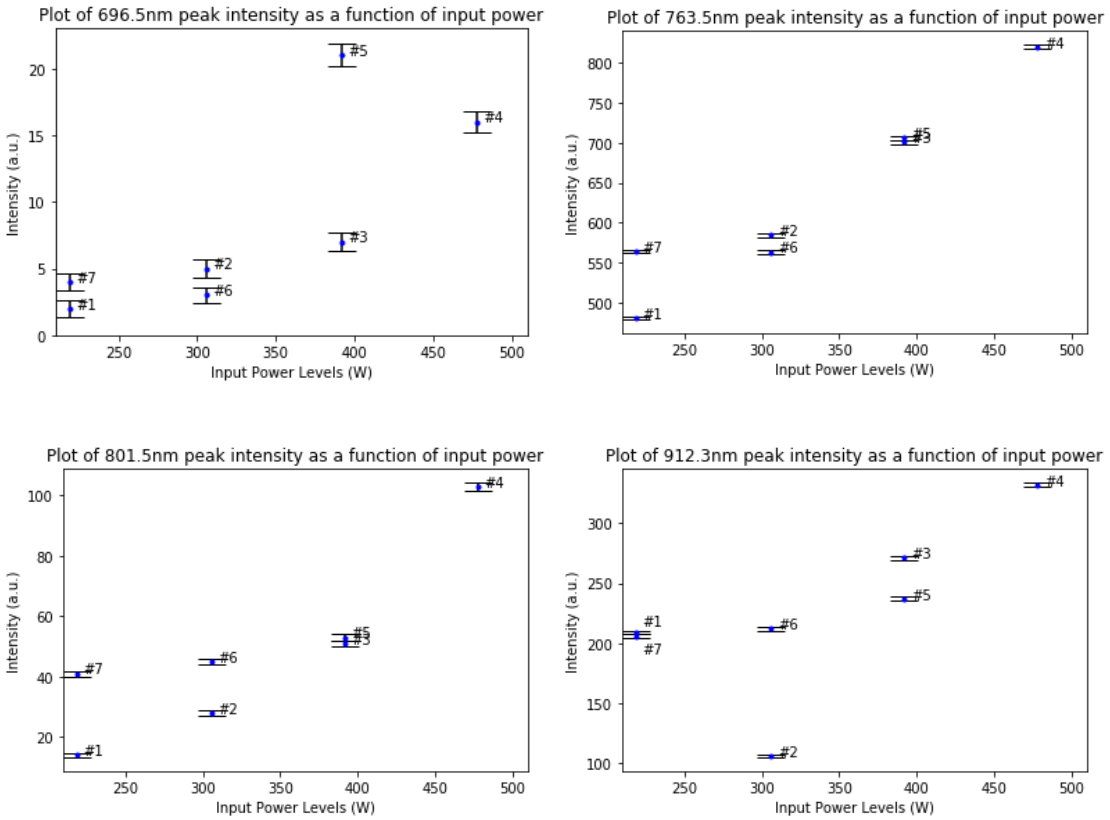

FIGURE 4.9: Line intensities as a function of input power for various emission lines of an argon plasma. All plotted emission lines consist of transitions from excited states to metastable species of argon.

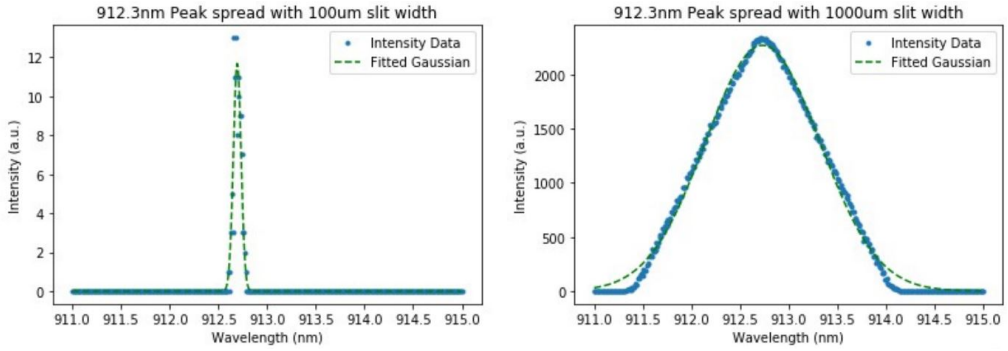

FIGURE 4.10: Sample plots of argon 912.3 nm emission line for 100 µm and 1000 µm slit. Dashed line is a Gaussian fit to the data (for reference) which assumes no source of error.

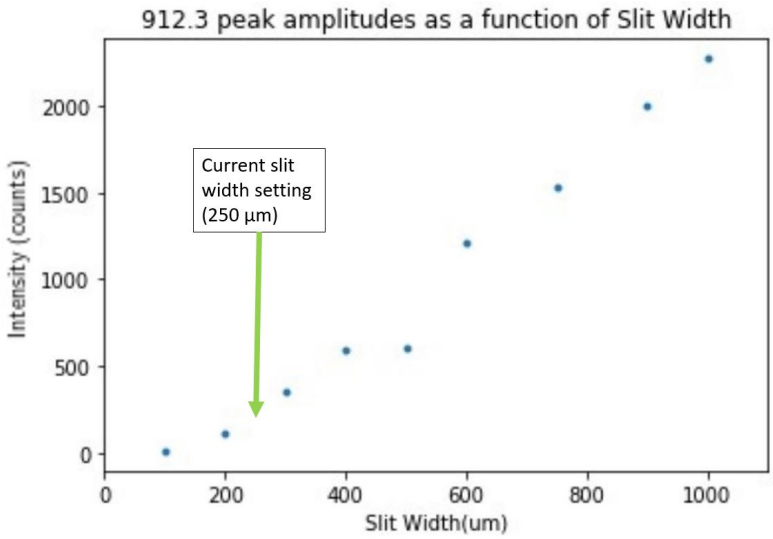

FIGURE 4.11: Plot of argon 912.3 nm peak amplitude as a function of monochromator entrance and exit slit widths.

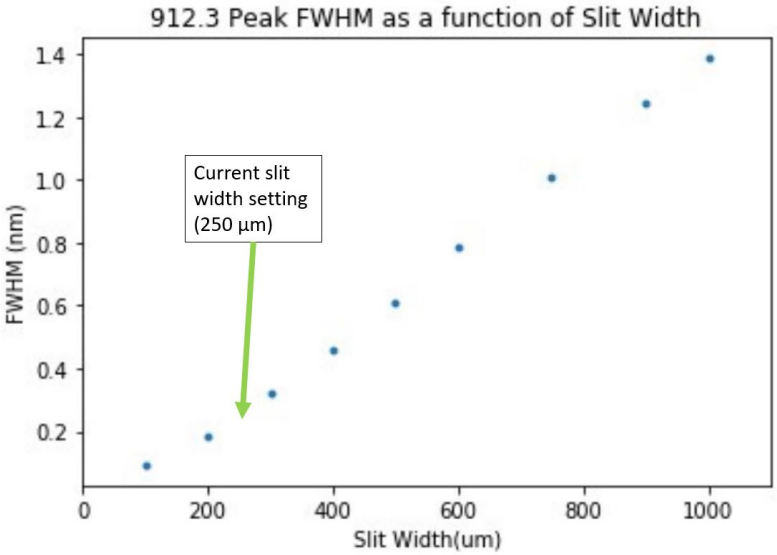

FIGURE 4.12: Plot of argon 912.3 nm emission line FWHM as a function of monochromator entrance and exit slit widths.

4.2.3 Estimation of Microwave Argon Plasma Parameters

Table 4.4 shows parameters in the similar fashion of Table 2.2. The parameters of the microwave argon plasma are estimated assuming a temperature of $2200K$, and STP gas density conditions for density (due to the argon gas being vented to atmosphere before ignition). Ion density was arbitrarily assumed to be 10^{-6} to 10^{-2} times the density of the gas so that an estimation could be made of the Debye Length. The scale length of the argon plasma taken from the inner diameter of the test section, and a typical length of the plasma jet. Consider all values order of magnitude estimates. Some of the argon plasma's parameters lie "in between" that of the "dense" and "diffuse" plasmas: the scale length and Debye length. The density is higher than the two, and has a lower estimated Debye length. The value of $n{\lambda_D}^3$ confirms that the argon plasma is valid to be treated as a plasma. The temperature is lower than both the "dense" and "diffuse" plasmas.

TABLE 4.4: Estimates of this work's argon plasma parameters with laboratory plasmas from Table 2.2 as reference [18, 20].

Symbols	n	T	λ_D	$n{\lambda_D}^3$	l_{mfp}	L
Units	m^{-3}	K	m	unitless	m	m
Dense Bench Plasma	10^{20}	10^4	10^{-6}	10^3	10^{-2}	10^{-1}
Diffuse Bench Plasma	10^{16}	10^4	10^{-4}	10^5	10^1	10^{-1}
Argon Plasma (this work)	10^{24}	10^3	10^{-8}-10^{-6}	10^2-10^7	N/A	10^{-2} & 10^0

4.2.4 Streamers

In the process of producing argon plasma in in the microwave system, filaments were produced that run against the flow of the gas. They are referred to as streamers. There are multiple streamers, and more gradually appear as the power to the plasma is increased. These streamers may also be found moving with the flow of gas as the power is increased. The power increase likely acts to extend their length. The rotation of the tube test section, while the plasma is being produced, does not appear to influence the orientation of the streamers. Figure 4.13 shows the streamers that appear in the plasma.

The streamers differ from the plasma jet in several ways. They appear more opaque than the jet. Secondly, they appear to be repelling one another, suggesting that there are charges contained within them. It is inferred that these streamers are formed by high-speed electrons. Electrons are significantly lighter (in terms of mass) than the gas ions. With enough kinetic energy imparted to them, they should be able to move against the inflow of argon gas. These electrons collide with successive argon gas atoms, exciting them as they deposit kinetic energy. Eventually, the electrons slow down sufficiently to no longer excite the atoms, limiting the length of the glow of the streamer.

4.2.5 Plasma Jet Height

The height of the plasma jet is found to be dependent on the level of microwave power being imparted to the gas. The jet height is also a function of the gas flow rate. This is to be expected. For higher flow rates, the gas travels at a faster velocity. The light from emissions, which make up the jet, have decay lifetimes that are associated with their transition probabilities [34]. These excited states that emit light are carried farther away with a higher gas velocity and so effectively extend the height of the jet as they decay farther away from the region where they were initially excited. This could introduce a bias in temperature measurements if spectroscopic data is taken further away from the the point of excitation.

A higher microwave power increases the number of exited states (and de-excitations) as the plasma absorbs more microwave energy. More excited states means that the jet will effectively be extended in size in a similar manner. This is numerically demonstrated in Figure 4.14, which outlines the results of an experiment which modified input power and gas flow rate and observed the changes in plasma height.

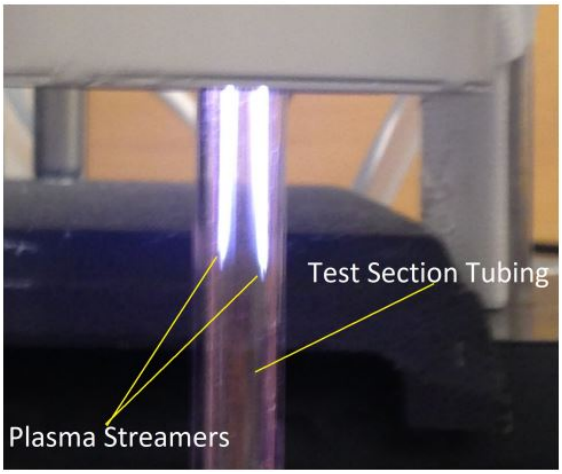

FIGURE 4.13: Streamers produced by plasma. Note that they appear against the flow of argon gas.

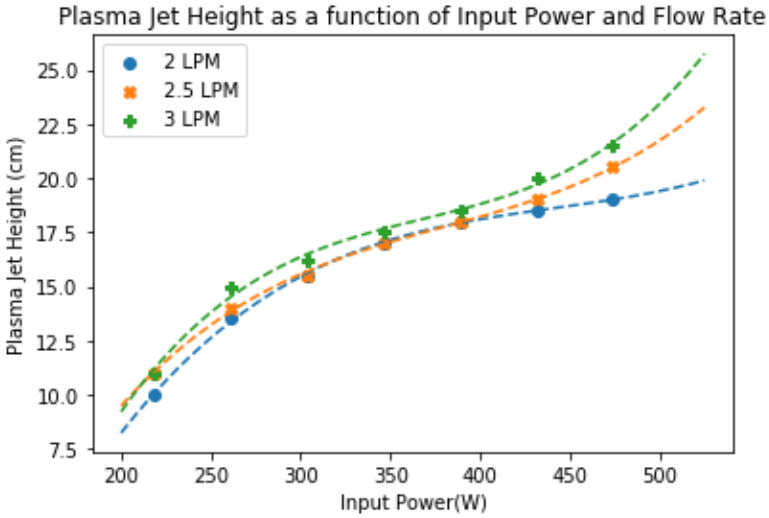

FIGURE 4.14: Argon plasma jet height plot as a function of power and flow rate. Third order polynomial fit lines were performed for each set of height vs power datapoints for a given flow rate. Height steadily increases as a function of both. For higher input powers, the difference in jet heights for a given flow rate (as a function of input power) appears to grow.

In general, the jet height fluctuates above and below its mean value by about half a centimeter. This may be due to the magnetron not producing microwaves at a completely stable rate. The measured forward power, for high output microwave values, has been observed to fluctuate both on the display and the control by about 10 W. What is noted in Figure 4.14 is that the trends of the lines (height vs input power) at power levels above 400W appear to differ based flow rate.

4.2.6 Effects of Tuning Settings

This section focuses on the effects that the stub tuners have on the plasma as it is being generated. Tuning was an important factor to maintaining an argon plasma for a long enough time to perform spectroscopic measurements with the monochromator. A high resolution scan with the monochromator in the wavelength range where emission lines are detectable cannot be completed if the plasma is not sustainable for over 2-3 minutes. A consistent tuning setting was used for most experiments of this work, but the effects of changing them are described in this section.

Figures 4.15 to 4.17 summarize observations made about various quantitative values relating to the plasma as tuning settings were changed from the set value of (7 mm, 9 mm, 9 mm). The plots are grouped based on similarities to one another. The first set in Figure 4.15 shows the plasma height and the measured reflected power change with the insertion length of a single tuning stub, while holding the others constant.

The relationship between jet height and measured reflected power is that as one grows, the other decreases. This is to be expected for similar reasons discussed earlier: if the plasma is absorbing more energy, less power is being reflected and, therefore, the jet height increases. Other behaviour is observed in Figure 4.16. The 696.5431 nm and 763.7208 nm lines are correlated. They were chosen as they have strong intensities. Note that there are different effects for each stub tuner as well.

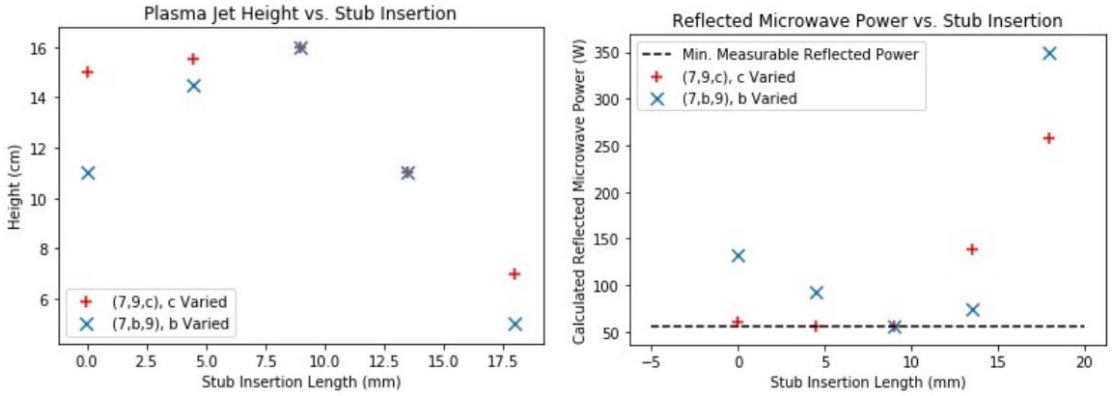

FIGURE 4.15: Plots of plasma jet height and reflected power as a function of individual stub insertions. Legend indicates which tuner is being varied and which tuner is being held constant. Note the different effects based on the different stub tuner used.

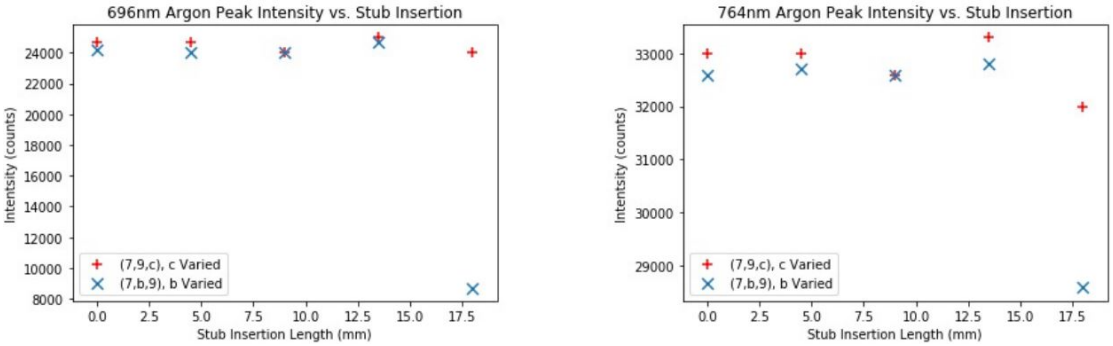

FIGURE 4.16: Plots of 696.74 nm and 763.7208 nm peaks as a function of individual stub insertions. Legend indicates which tuner is being varied and which tuner is being held constant.

In comparison to the peaks outlined in Figure 4.16, the carbon peak behaves differently as it maximized at a different stub tuner setting. This is observed in Figure 4.17.

4.2.7 Gas Flow Regime

The regime of argon gas flow before ignition can be determined by calculating the Reynolds number as it flows through the tubes. In terms of flow rate $\dot{V}$, density ρ, tube inner diameter D, and dynamic viscosity μ, the Reynolds number Re is expressed in equation 4.1

$$Re = \frac{4\dot{V}\rho}{\pi D\mu} \tag{4.1}$$

All values are known. The flow rate is $4.1 \times 10^{-5}\,\mathrm{m^3\,s^{-1}}$ after conversions, the density is $1.784\,\mathrm{kg\,m^{-3}}$, the inner tube diameter is $5 \times 10^{-3}\,\mathrm{m}$, and the dynamic viscosity is $2.23 \times 10^{-5}\,\mathrm{Pa\,s}$. This calculation assumes an argon gas at room temperature, as it enters into the test section. This results in a range of Reynolds number of 1040, which is in the laminar flow regime. The jet produced by the plasma can reflects the fact that the argon gas is undergoing laminar flow. The layers of flow towards the center of the tube flow at a faster velocity, extending the tip of the jet farther than at the edges, where the flow is slower.

4.2.8 Yellow-Coloured Plasma

In some experiments, the typical purple-white glow of the plasma abruptly transitioned to a brighter yellow-orange glow that surrounds the jet, which is also observed in the region of the plasma seed. One instance of a yellow plasma produced in the system is featured in Figure 4.18.

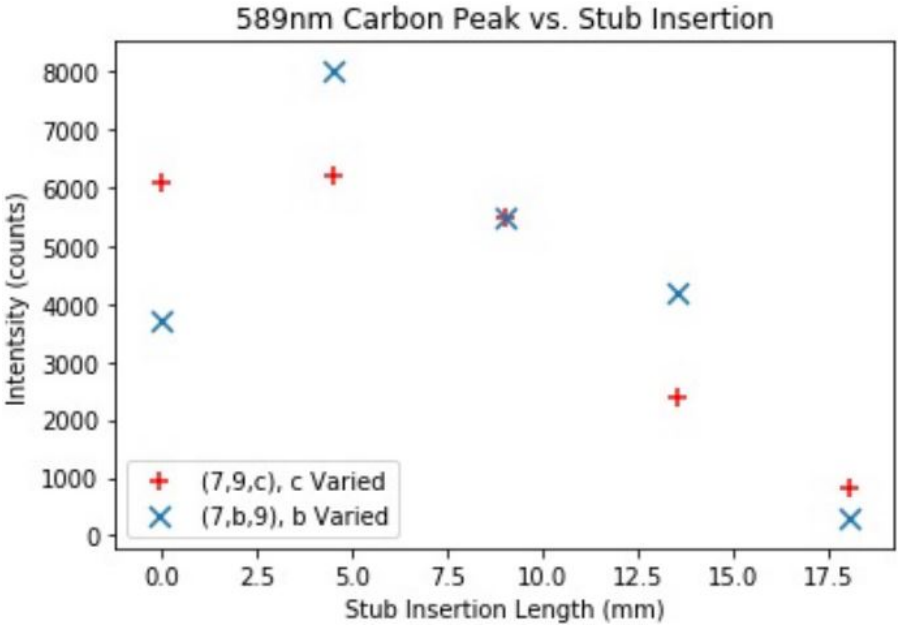

FIGURE 4.17: Plot of the 590.0 nm peak (associated with carbon in plasma seed) as a function of individual stub insertions. The carbon peak achieves its highest value at a different stub setting than typical experiments outlined in this thesis..

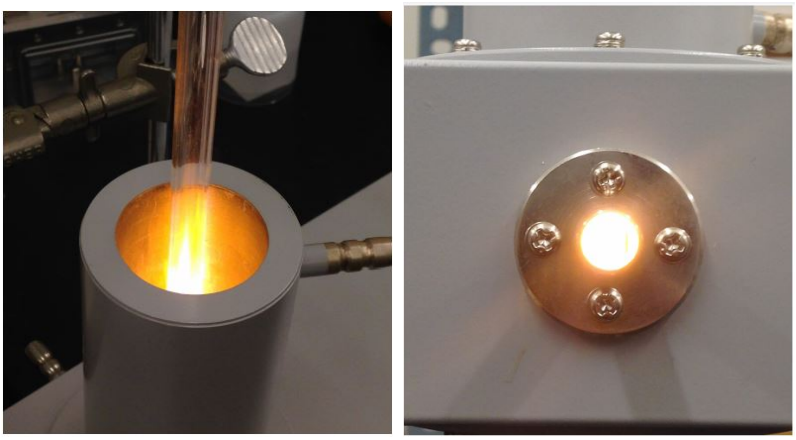

FIGURE 4.18: Glow produced by yellow-coloured plasma as viewed from above and viewport. Note that the glow is much more intense than the typical argon plasma seen in these experiments.

After these experiments were terminated, the glass wool, which is supposed to hold the plasma seed in place and seal the gap between the inner tube pieces, was observed to be melted. This is shown in Figure 4.19. This suggests that gaps between the inner and outer tubes of the test section formed and allowed air to enter the inner tube of the test section, which typically should be only argon gas. An improper seal can allow for air to be siphoned in through the test section. Gases from the air may have become excited and, in the process, changed the colour of the plasma. This nuisance has been resolved by reducing the amount of carbon seed and quartz wool used and better sealing the test section with electrical tape.

4.2.9 Comments on Plasma Seed

The plasma seed, as discussed in the materials and methods section, was required for this experimental setup, as it acts as a source of electrons to start the argon plasma inside the test section. Some attempts were made to produce argon plasma without the introduction of the plasma seed into the test section, but no ignition took place.

A single carbon peak is occasionally observed with the DK-480 monochromator: a 589 nm peak associated with an excited state of the first ionization state of carbon. This is seen in Figure 4.20, which plots the spectrum observed by the monochromator in the 589 nm region for various input powers. The scale is logarithmic to facilitate the viewing of the peaks, as the intensities change over orders of magnitude. The carbon cation emission line suggests that that carbon ions are being formed. The electrons from the originally neutral carbon atoms are inside the plasma, which confirms that the seed is a source of electrons. The carbon peak intensity increases with input power. The emission line also suggests the presence of carbon inside the plasma. In short, the plasma seed is likely degrading as the lines are associated wtih liberated atoms and ions from the plasma seed itself. This is verified in Figure 4.21. It shows before and after photos of carbon seed after being used in experiment. The ends of the seed that are pointing in the direction of gas flow that are those that are observed to be degraded. The end that points with the flow of the gas is also the end closest to the geometric center of the field applicator's cavity.

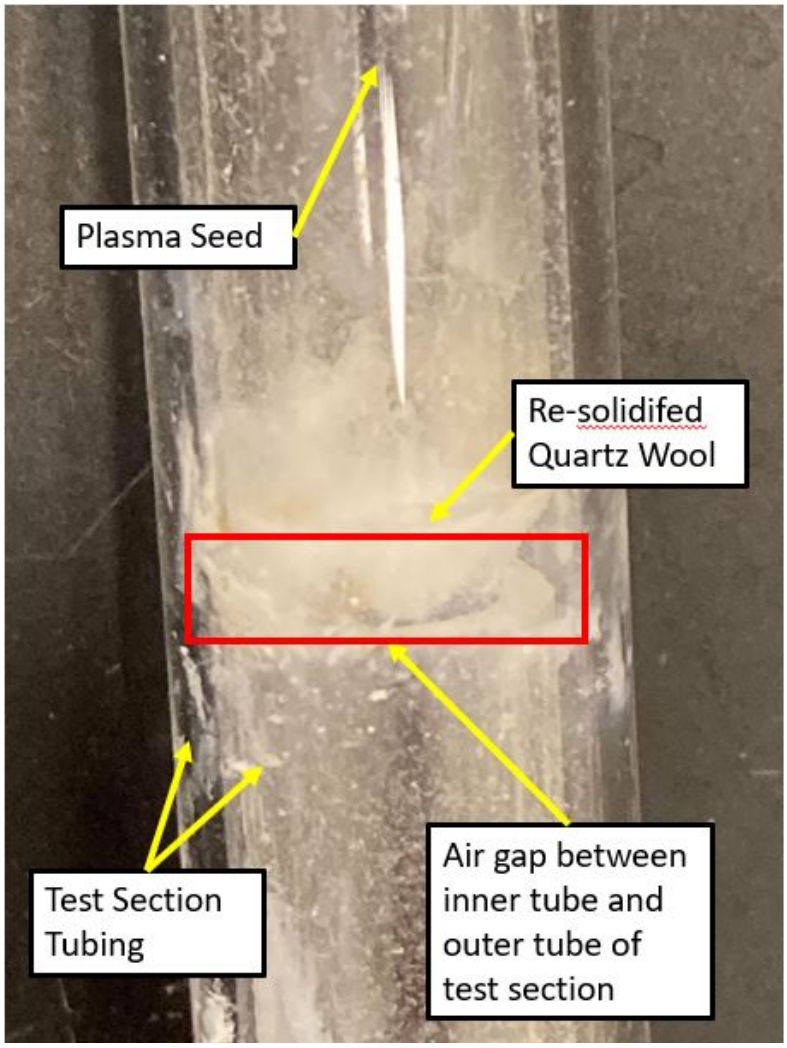

FIGURE 4.19: Image of gap in plasma seed region of test section between the inner and outer tube. Melted quartz wool also visible.

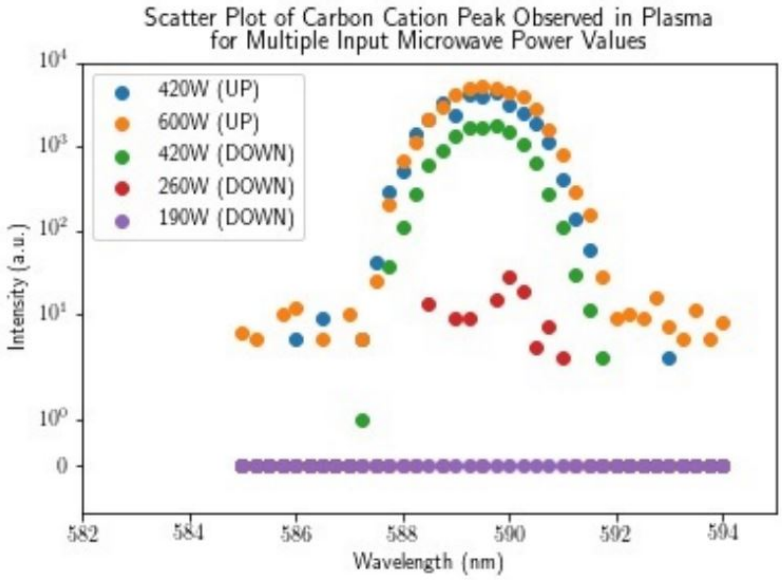

FIGURE 4.20: Log-scale of 589 nm peak spectra. The peak is associated with Carbon cation for various input powers. The "UP" and "DOWN" labels indicate whether measurements were taken while ramping microwave power up or down and taking measurements during the process.

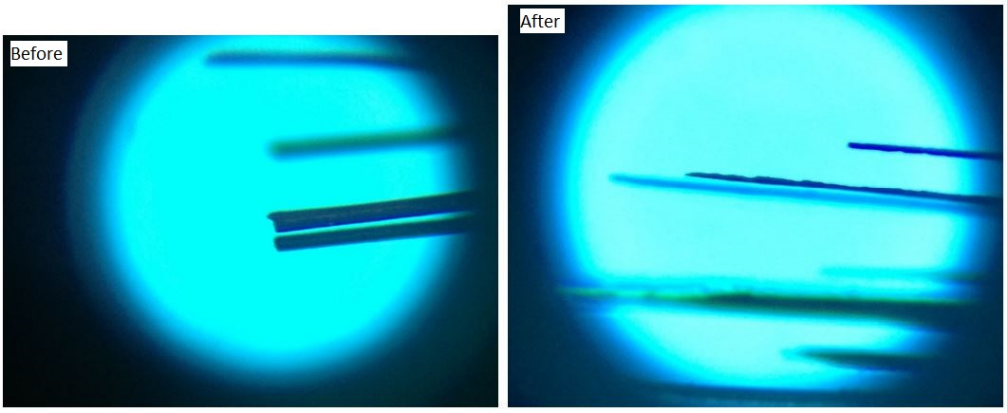

FIGURE 4.21: Image plasma seed strand tips before (left) and after (right) usage in plasma production. Note the degradation at the tip regions. As a note, the strand tip thicknesses are on the order of a tenth of a millimetre.

4.2.10 Devitrification

Devitrification is the phenomenon of amorphous glass that recrystallizes due to changes in temperature. This typically occurs due to temperature differences, and the presence of impurities in and on its surfaces. After some plasma test sections were finished being used, it was observed that opaque films form around region of where the plasma jet were formed, even though no melting of the glass had occurred. The manufacturer of the glass tubing (ChemGlass) suggested that devitrification occured. The film is far more brittle than the tube surface, and can be scraped off with a knife or sharp object. In Figure 4.22, two glass fragments are shown. One that was unused, and one devitrified glass fragment from a used test section.

The devtrified fragment is opaque and irregular at its surface. This indicates that the surface of the outside of the test section tubes have devitrified. Some test sections have undergone devitrification after being subjected to thermal stresses, such as multiple start ups and shutdowns of plasma production without allowing the tubing to fully cool down. Devitrification may also occur if plasma is generated for an extended amount of time.

Length of Plasma Generation Experiments

The duration of argon plasma production using the current limitations on input power (maximum of 600 W) and test section construction procedure has not been well-defined. The longest experimental run was on the order of fifteen minutes (at various input powers up to 480 W). The run ended not due to any failure of the test section but was shut off manually. Experiments verifying the endurance of the setup may be completed at a later date. It has not been verified whether devtrification, another phenomenon that could be treated as a failure mode (due to the potential blockage/distortion of spectroscopic data) occurs while the plasma is produced and the tubing is at an elevated temperature, or after the tubing cools down to room temperature.

For higher input powers the test section eventually does begin to soften and melt in the region where the plasma is produced. Figure 4.23 showcases a test section held at an input microwave power of ∼600 W for five minutes.

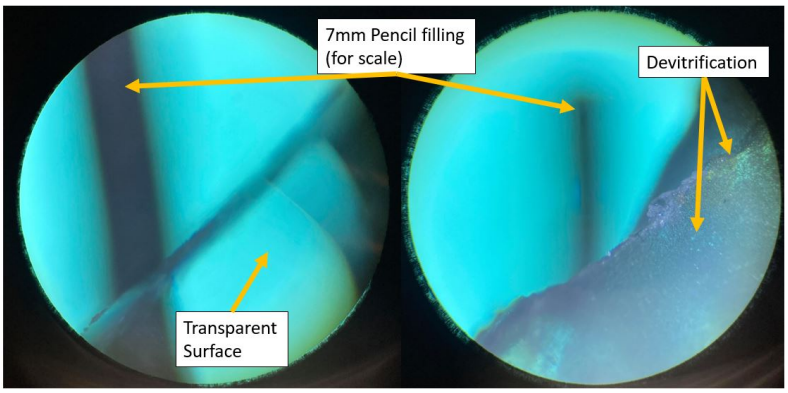

FIGURE 4.22: Fragments from a unused (left) de-vitrified (right) tube under microscope. A 7mm pencil filling sits in the background to provide a sense of scale.

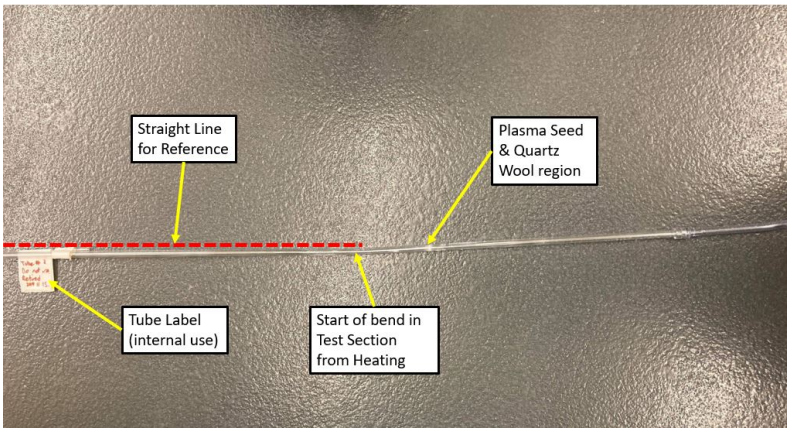

FIGURE 4.23: Bent test section after argon plasma produced at high input power within. Total test section length is on the order of 1.25 m.

The tube bend is located above the plasma seed region. It is here where the plasma was likely at its hottest, or is sufficiently well-formed that it can heat the edges of the test section, softening them. The test sections were clamped from above, which means the tubing below the softened region was could bend from the weight of the gas tubing below.

4.3 Contaminant Introduction into Argon Plasma

This section reports the observations made during experiments where samples of contaminants were introduced into the test section before producing plasma following typical procedures.

4.3.1 Qualitative Behaviour

The introduction of cesium iodide into the argon plasma test section resulted in a change in plasma behavior when plasma production was first initiated. This is shown in two images in Figure 4.24. Note the opacity of the plasma, as well as the colour. A white substance begins to coat the edges over time. The image on the right features a "piece" of plasma glow that appears to detach from the jet. This is behaviour not observed with the pure argon plasma.

Other behaviour is demonstrated in Figure 4.25, which features images of the plasma running for roughly a minute after ignition. The is an opaque purple glow, along with a mildly visible plasma jet in the right-most photo. The deposits are visible on the edges of the test section and now are thick enough that the test section ceases to be transparent in those regions. The opaque glow is due to introduction of new species into the plasma. As the experiments progressed, a gradual build-up of a white substance and a yellow substance were observed on the walls of the test section. Based on previous work, these material buildups are determined to be deposits of cesium and iodine, respectively [17].

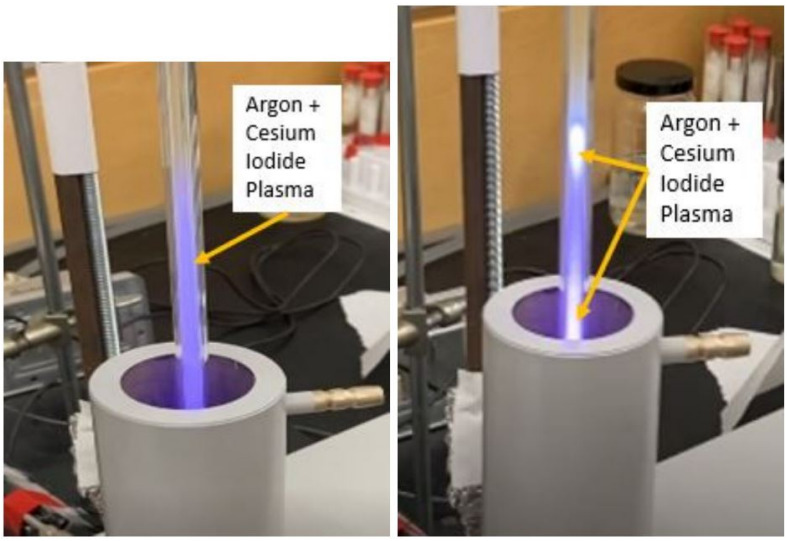

FIGURE 4.24: Photos of argon plasma with cesium iodide contaminants introduced.

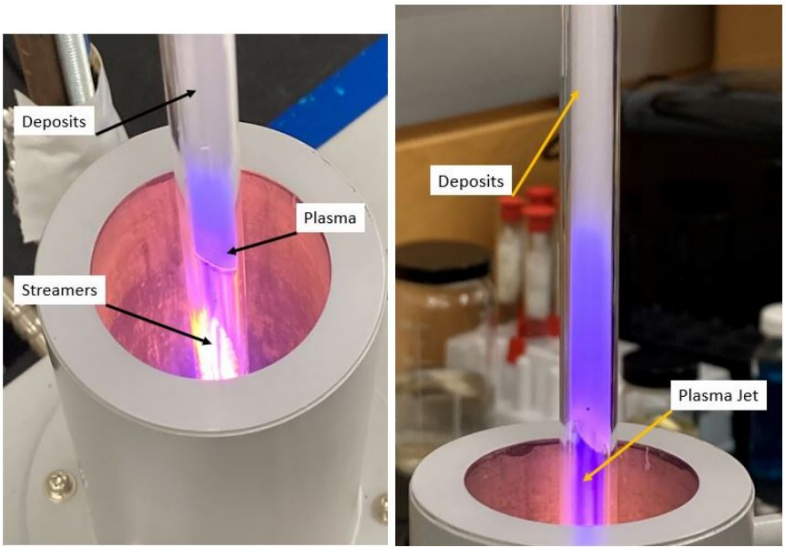

FIGURE 4.25: Various photos of argon plasma with cesium iodide contaminants produced a minute after ignition.

A time evolution of these depositions (from different trial run) are visualized in Figure 4.26. Input power was held constant at $190W$, and argon flow rate was held at $2.5\frac{L}{min}$. The snapshots were taken 3, 9, 26 and 41 seconds after microwave output was started and ignition occurred. The dividing line between both colours is highlighted in a pink box to demonstrate that the separation shifts over time.

4.3.2 Spectroscopic Measurements

For these experiments, spectral measurements were performed using the Black Comet. The Black Comet's ability to take continuous snapshots proved valuable for these experiments, which allowed for the observation of the time-evolution of the plasma spectrum. Figures 4.27 and 4.28 feature spectra from the "pure" argon plasma and argon plasma "contaminated" with cesium iodide. In the 450 nm to 600 nm range, a set of new peaks are found in the spectra when cesium iodide is introduced. These are peaks of interest as they are likely associated with the contaminants introduced into the plasma.

Based on the previous experiments, argon's emission lines were typically measured in the 700-900 nm range as well as in the region of 450 nm and below, making the 450-700 nm region more suitable to search for cesium and iodine lines. Various wavelength windows were analyzed for differences in identified peaks and emission lines in that region. Figures 4.29 through 4.32 show the identification of cesium and iodine peaks from differences between the argon plasma spectra (left) and the "contaminated" spectra (right). In many cases, the lines appear to "stack" on one-another, making a larger peak. For this work, it does not particularly matter which line "dominates" in terms of the intensity that it contributes.

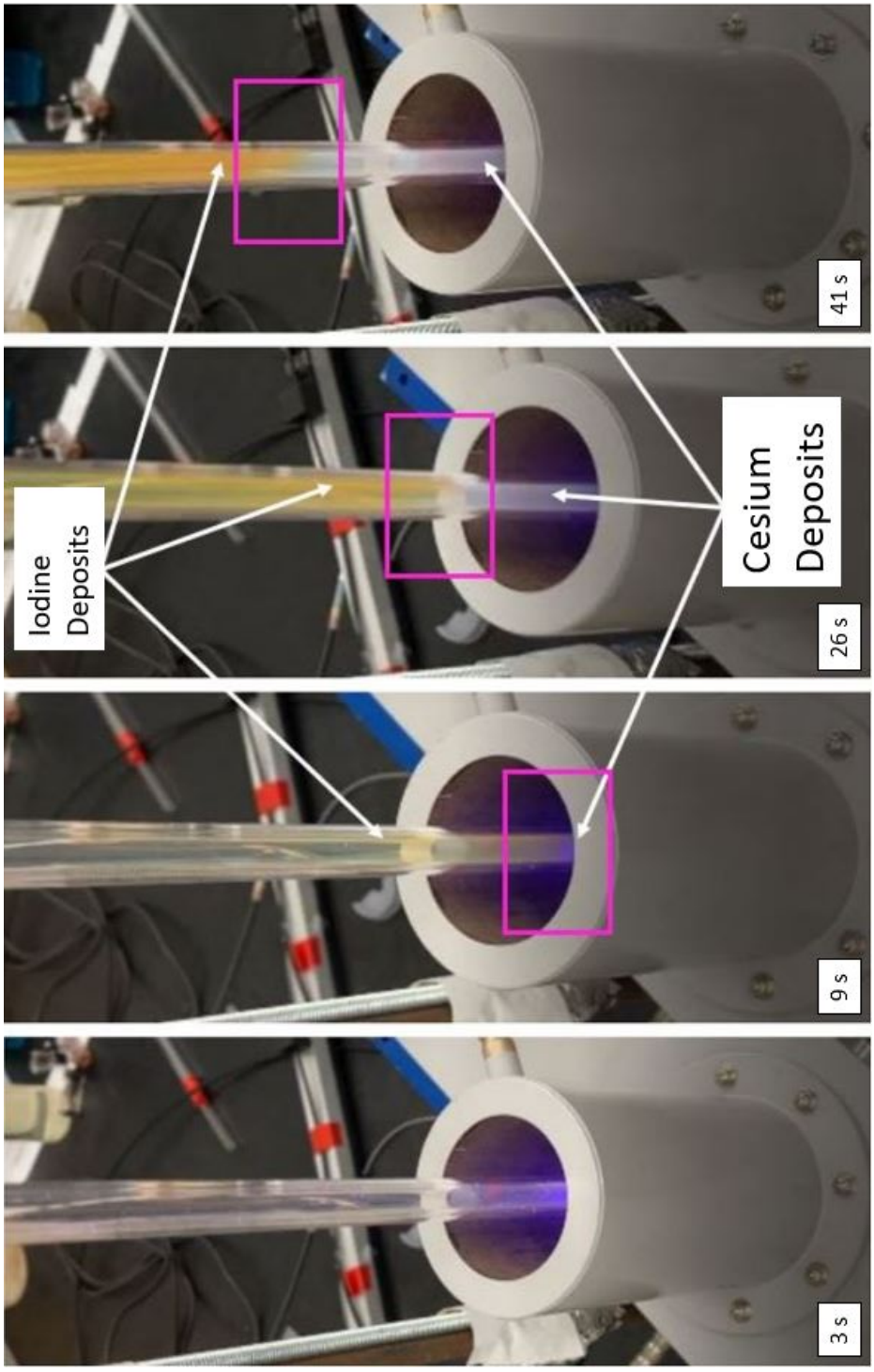

FIGURE 4.26: Time-evolution of iodine (yellow) and cesium (white) depositions on the side of the test section inner tube.

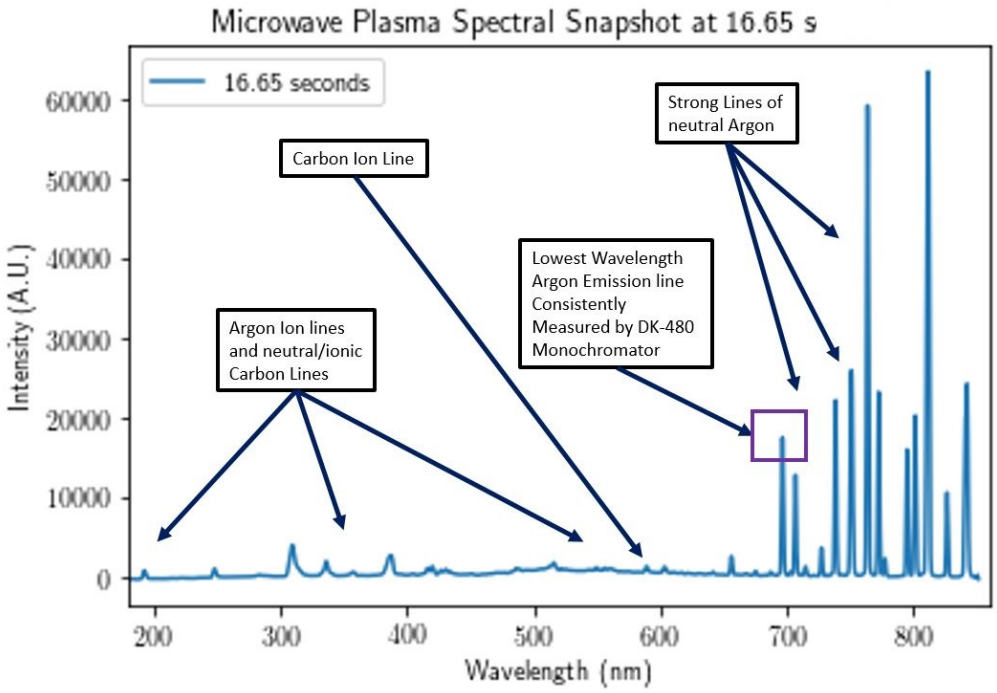

FIGURE 4.27: Full-scale argon plasma spectrum produced by Black Comet: input power of $\sim$ 219W.

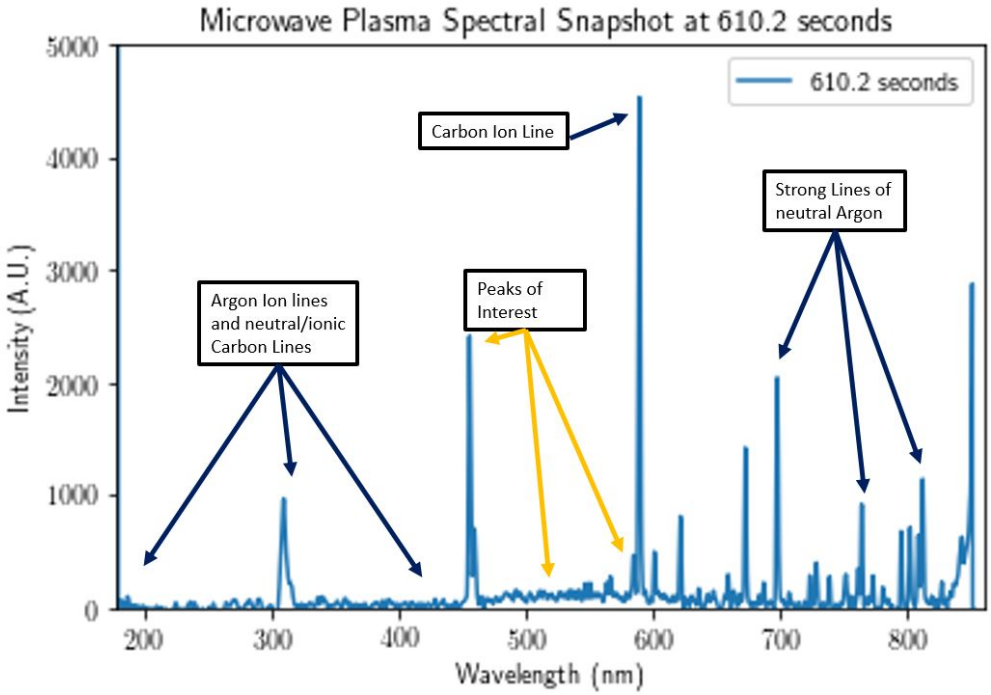

FIGURE 4.28: Full-scale argon plasma spectrum produced by Black Comet with cesium iodide contaminants introduced: input power of $\sim$ 219W.

What does matter is that the lines are identified. These sets of spectra are taken from two separate trial runs, so the scales and spectral baselines may be different. Figure 4.29 shows several undetermined peaks. They essentially disappear in the "contaminated" spectrum. Two lines are identified: a Cs I 455.5 nm line and a Cs II 460.4 nm line.

Figure 4.30 features many undetermined peaks and an identifiable carbon emission line. The contaminated spectrum features many of the same peaks, but with the addition of a peak associated with cesium and iodine emission lines that are clustered in the same wavelength region of 534 nm, and a cesium line at 556.3 nm.

Figure 4.31 shows many carbon peaks with a generally high "baseline" intensity. In the case of the contaminated plasma, there are well-defined peaks associated with cesium: Cs II at 562.8 nm, Cs III at 566.9 nm, Cs II at 583.1 nm, and the 590 nm Carbon peak remains present.

Figure 4.32 features multiple carbon lines as well as an Ar II and Ar I line. On the right, the 696.5 nm and 687.1 nm argon lines remain present, but the carbon peaks are dwarfed by the presence of multiple cesium and iodine lines: a cluster of Cs III lines at 660 nm, an iodine peak at 662.0 nm, a stack of a Cs I and a Cs II line at 672.3 nm and 672.4 nm, and finally a stack of an I II line and a Cs I line at 681.3 nm and 682.5 nm.

Table 4.5 tabulates all cesium and iodine emission lines found in figures 4.29 to 4.32. For cesium, neutral, first ionization and second ionization state lines were detected. For iodine, the neutral and first ionization state lines were detected.

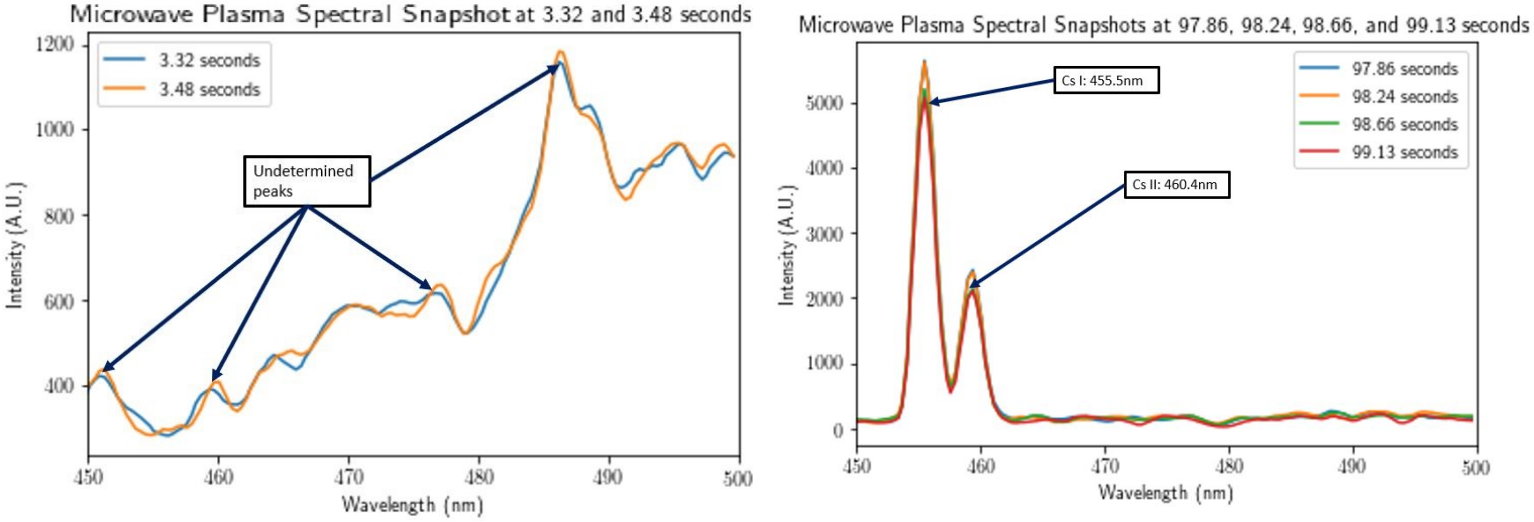

FIGURE 4.29: Comparison of non-contaminated and cesium iodide-contaminated argon plasmas for the 450 to 500nm wavelength range.

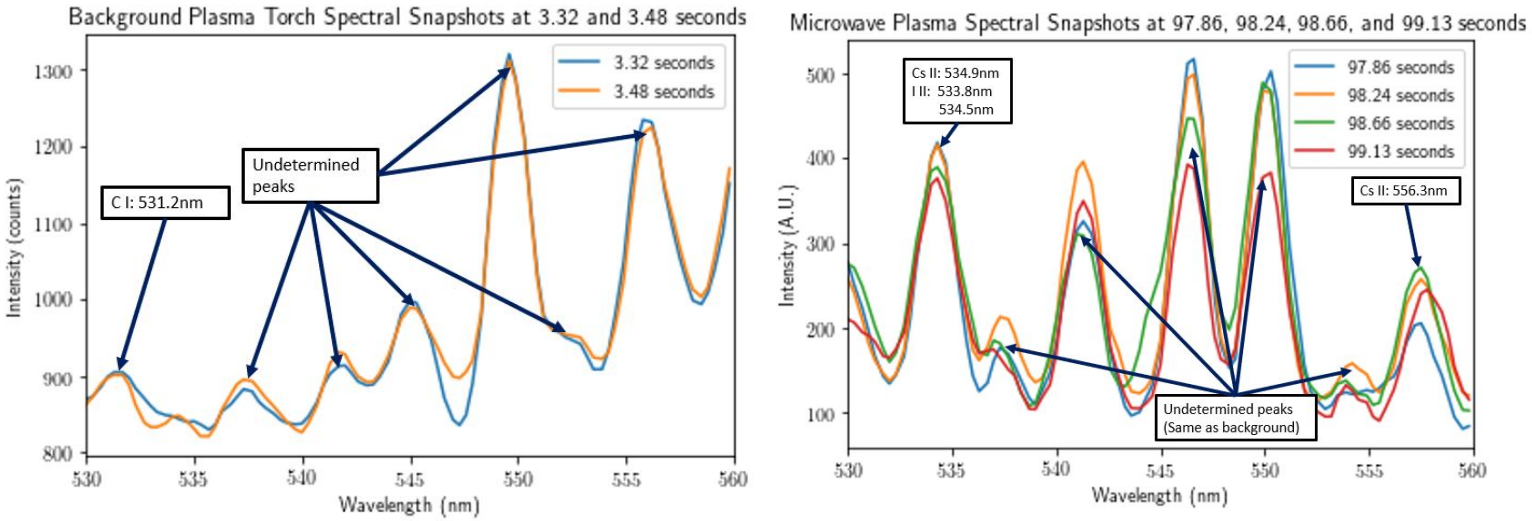

FIGURE 4.30: Comparison of non-cotaminated and cesium iodide-contaminated argon plasmas for the 530 to 560nm wavelength range.

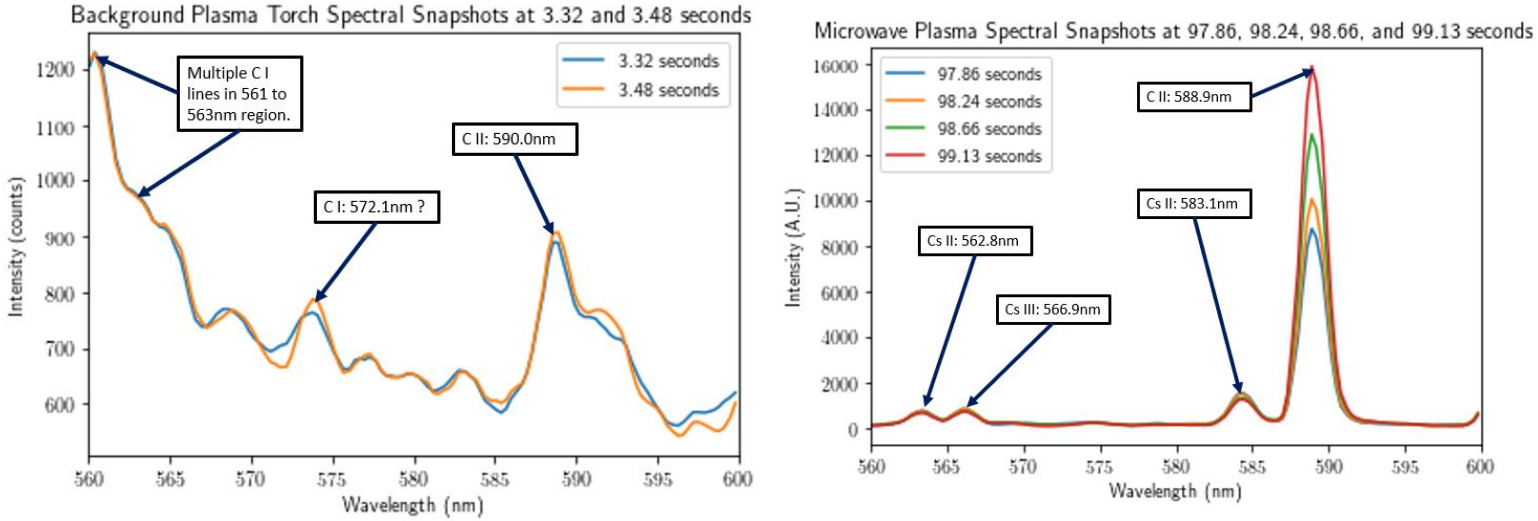

FIGURE 4.31: Comparison of argon plasma and cesium iodide-contaminated argon plasma for the 560 to 600nm wavelength range.

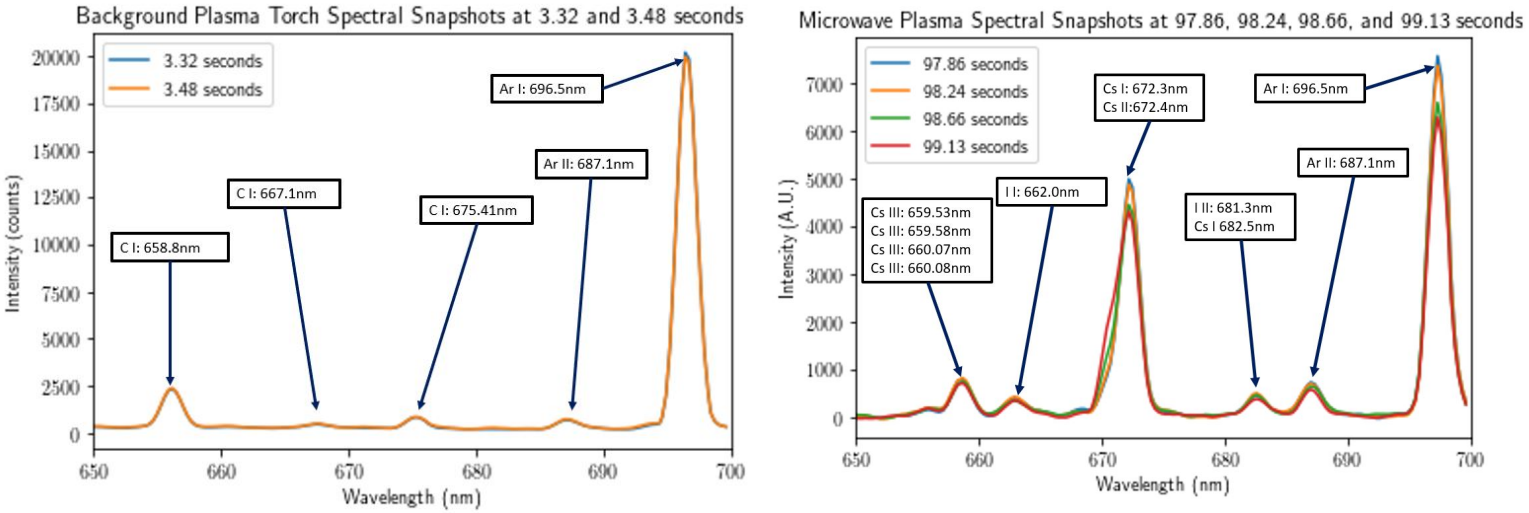

FIGURE 4.32: Comparison of argon plasma and cesium iodide-contaminated argon plasma for the 650 to 700nm wavelength range.

TABLE 4.5: Tabulation of cesium and iodine lines from experiments when cesium iodide introduced into argon plasma column in microwave system.

Cesium Species	Wavelength	Iodine Species	Wavelength
Cesium I	455.5 nm	Iodine II	533.8 nm
Cesium II	460.4 nm	Iodine II	534.5 nm
Cesium II	534.9 nm	Iodine I	662.0 nm
Cesium II	566.3 nm	Iodine II	681.3 nm
Cesium II	562.8 nm		
Cesium III	566.9 nm		
Cesium II	583.1 nm		
Cesium III	659.53 nm		
Cesium III	659.58 nm		
Cesium III	660.07 nm		
Cesium III	660.08 nm		
Cesium I	672.3 nm		
Cesium II	672.4 nm		
Cesium I	682.5 nm		

4.3.3 Time Series Measurements

The Black Comet's ability to take rapid time snapshots allowed to measure the time-evolution of a trial run of argon plasma with 0.15 g of cesium iodide introduced into the test section before ignition. This trial run initially ignited the plasma at $190W$, and increased the input power in steps. Figure 4.33 shows a time series plotting of the relative intensity of emission lines associated with neutral argon, metastable neutral argon, iodine, and cesium species as a function of time.

Each line in Figure 4.33 is associated with the emission that indicates the presence of an excited state. "Ar I" indicates neutral argon, "Ar I*" indicates metastable argon, "I I" indicates neutral iodine, "Cs I" indicates neutral cesium, and "Cs II" indicates excited singly-ionized cesium. The intensities of each line in the time series is measured in its relative intensity (intensity value divided by its maximum value in the series) to demonstrate their relative growth/decay in intensity over the trial. This facilitates the observation of all lines in one plot. Figure 4.33 also has plot of the measured forward microwave power as a function of time.

After ignition or an increase in input power, the intensity values tended to temporarily increase for some amount of time. This suggests the plasma as well

as the contaminants undergo excitation reactions as more of the contaminants are liberated from their salt form when the power is increased. These liberated contaminant species, the cesium and the iodine, were then deposited on the walls of the test section and were partially removed from the plasma as they deposited. Some excited species remained, as demonstrated by the regions between the spikes not dropping to zero relative intensity. Each time the power is increased, a spike in all intensities is observed.

The Ar I line drops to a low relative intensity (~ 0.02) between the spikes, while all the other lines do not. The growth and decay of the Ar I* line lines up with the growth and decay of the cesium and iodine lines. This is expected to some extent, as metastable reactions with salt along with the Penning ionization reaction are the mechanisms expected to liberate and ionize the cesium (and iodine) species. Overall, as time passes, even between changes of input microwave power, the intensity of the cesium and iodine lines tend to increase: the contaminant salt was gradually being consumed by the plasma, as verified in Figure 4.26. The iodine levels appear high due the changes in absolute intensities being small. Note the size of the fluctuations in comparison to the rest. After the trial, some of the cesium iodide remained in the carbon fibre bundle, so it was not all consumed.

4.4 Arc Plasma Torch Experiments

This section describes the qualitative and quantitative observations made during the the cutting of contaminated and non-contaminated samples. Firstly, qualitative observations observed throughout both sets of experiments are described, and then a discussion of the spectroscopic measurements made during the different experiments will be made. Finally, emission lines associated with the cesium and iodine contaminants will be identified using a finite wavelength region of the spectra produced.

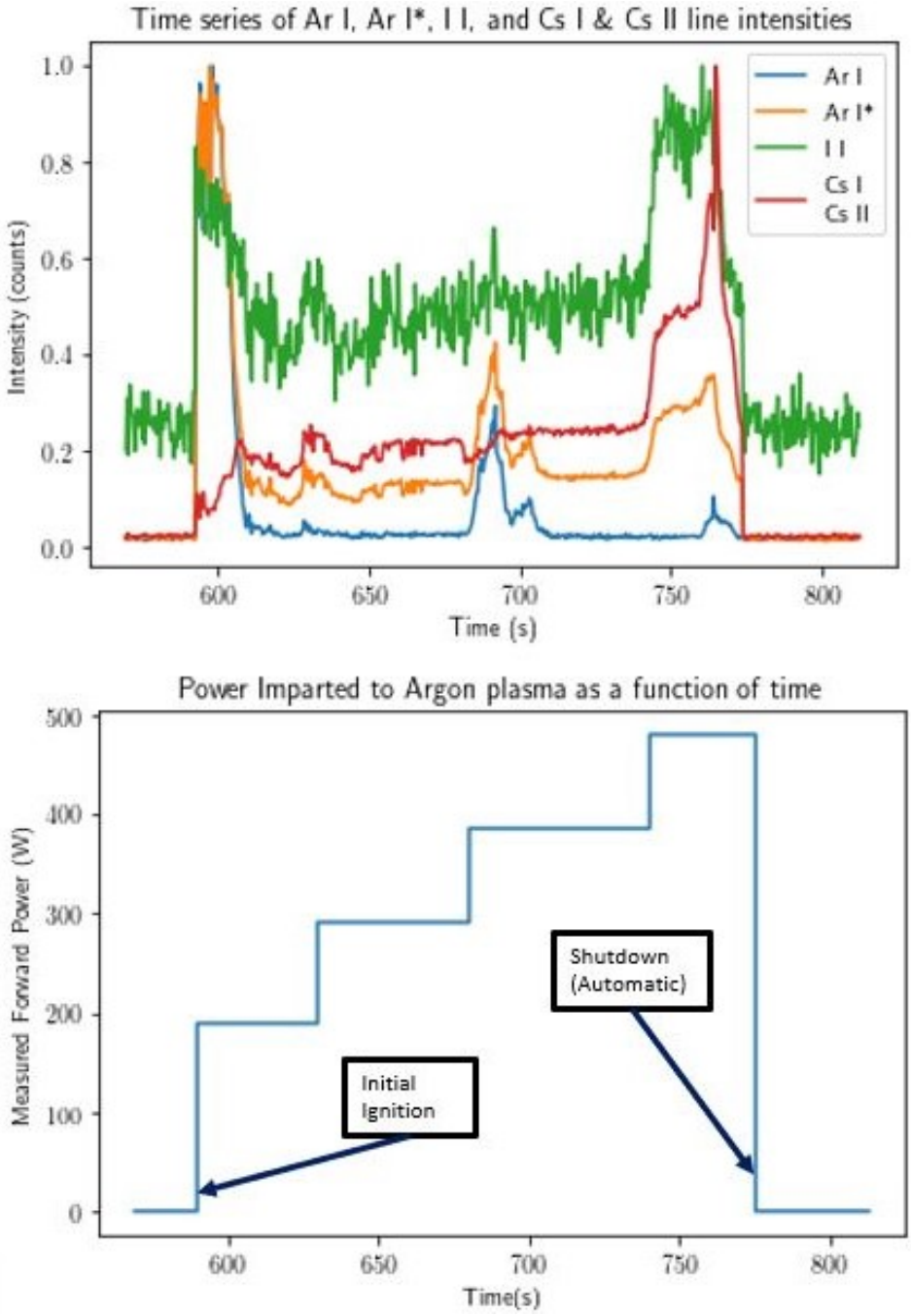

FIGURE 4.33: Time series of emission lines for neutral argon, metastable neutral argon, and cesium emission lines.

4.4.1 Observations

The baseline spectrum of the plasma torch was obtained by cutting bare metal samples with the torch and observing the spectra. Though not directly observable to the naked eye for safety reasons, the cutting torch plasma took on a blue colour when photographs are taken with cameras. Protective glasses were used when cutting with the torch. This is seen in Figure 4.34 and 4.35 where the cutting torch cuts metal samples from above and below.

The cutting of metallic components created various by-products. The metal melted and vaporized, along with the paint coating. Sparks would fly in all directions, but primarily in the direction of the gas flow. Recall that the air pressure provided by the torch's compressor is 345 kPa. Metal particulates, that often ricocheted off of surfaces, were found in the vicinity of the enclosure where the cut takes place. The metal sample tended to melt in the regions around where the cut takes place. This melted metal congealed in small droplets or clumps, which then rapidly cooled off and solidified. These experiments demonstrate that if the metal samples were to be contaminated, the spread of contaminants would reach into the general environment in many forms. The enclosure used in these experiments helped contain some of the spread of large particulates such as metal particulates.

Cutting Contaminated Metal Samples The cuting of the contaminated components resulted in some additional behaviour. If not cut quickly, the plasma would heat up the contaminant-glue clump to the point where it would glow, weaken its binding to the surface, and then escape into the enclosure due to the air pressure from the plasma torch. These glowing clumps likely contributed to "lumps" and high baseline of the measured spectra, caused by blackbody radiation.

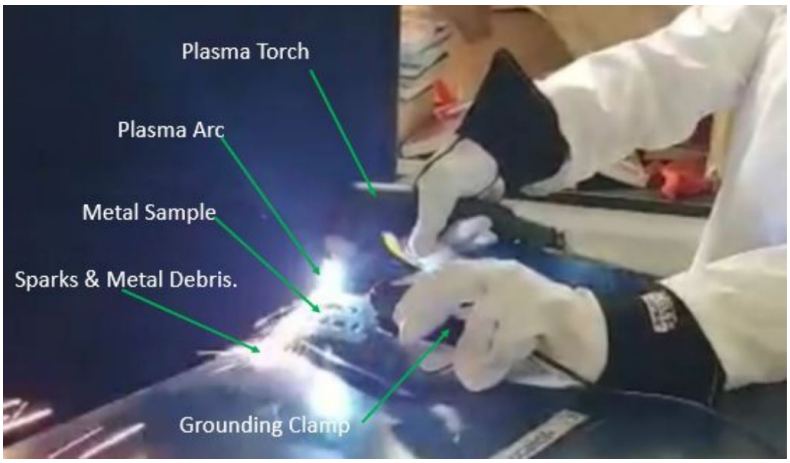

FIGURE 4.34: Plasma torch in use. Component is being cut from above.

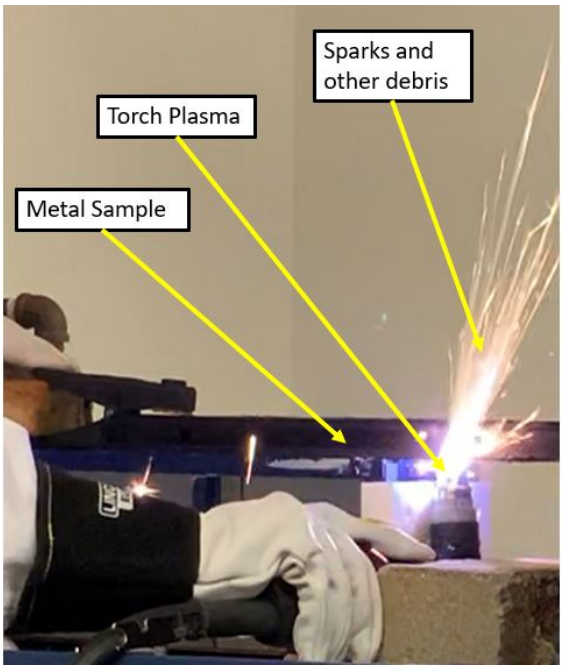

FIGURE 4.35: Plasma torch in use. Component being cut from below.

4.4.2 Spectroscopic Measurements

A partial spectrum of the plasma torch was recorded using the DK-480 monochromator and the fibre optic cable attachment to the torch handle. Figure 4.36 displays the measured spectrum taken in the 650 to 800 nm range. One notable feature is a large spike in the 777 nm range. There are three strong oxygen peaks that are found at that wavelength value. This indicates that part of the plasma being produced by the torch is one that involves atomic oxygen. Due to the poor resolution of the lines in the spectrum in Figure 4.36, the spectrum could not be analyzed (identification of precise emission lines and Saha plots) in a similar manner to those obtained from the argon plasma experiments. Many of the peaks in the 660 to 750 nanometer range are generally associated with first ionization states of nitrogen and oxygen based on the lines found in the NIST atomic database [37]. The peaks tend to meld into one another due to the lower resolution. This makes lines difficult to identify due to the high numbers of emission lines may be produced in this region. Air consists of several chemical species, all with their own sets of emission lines, so it is not unexpected to observe so many peaks on the spectra measured by either spectrometer system.

Figure 4.37 shows the full-scale torch spectrum as measured by the Black Comet for two different time instances. There are generally two types of spectra observed in the plasma torch experiments. There is a baseline spectra that is observed, associated with the metal and some of the strong air lines, and an uplifted spectrum, likely more associated with the air plasma itself. These are the spectra at 9.03 s and 13.71 s, respectively. These different types may also be associated with the changing of the plasma's position. The fibre optic cable, which relays the light to the spectrometer, was always held in the same position. The plasma, as the cut takes place, moved from one position to another over time.

Figures 4.38 through 4.40 feature of the plasma torch's baseline spectrum as measured by the Black Comet. Most of the peaks consist of "stacks" of emission lines: multiple emission lines with wavelengths that are very similar. As a result, many of these emission lines blur into one another and are indistinguishable. There are several nitrogen peaks that stand alone, those at 742.364 nm, 744.229 nm, 746.831 nm, and 824.239 nm.

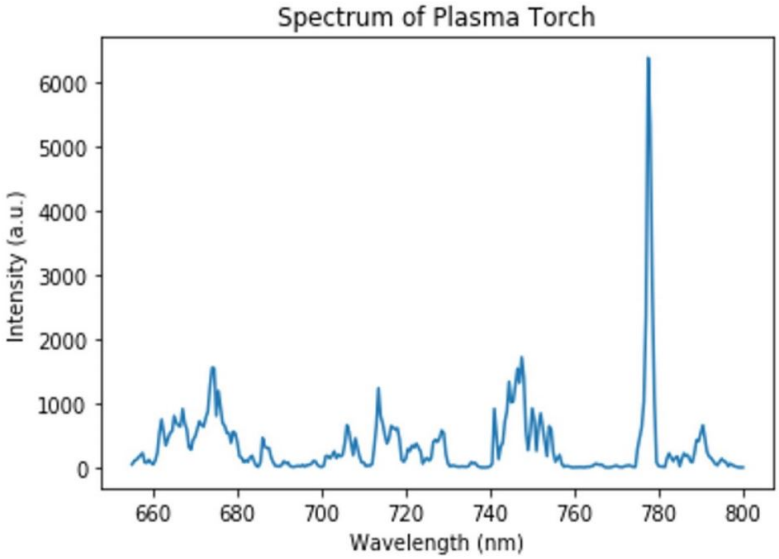

FIGURE 4.36: Partial Spectrum of arc plasma torch using DK-480 monochromator. A larger slit width (600 µm) was used to deliver more light to the monochromator's CCD. This larger slit width reduced wavelength resolution.

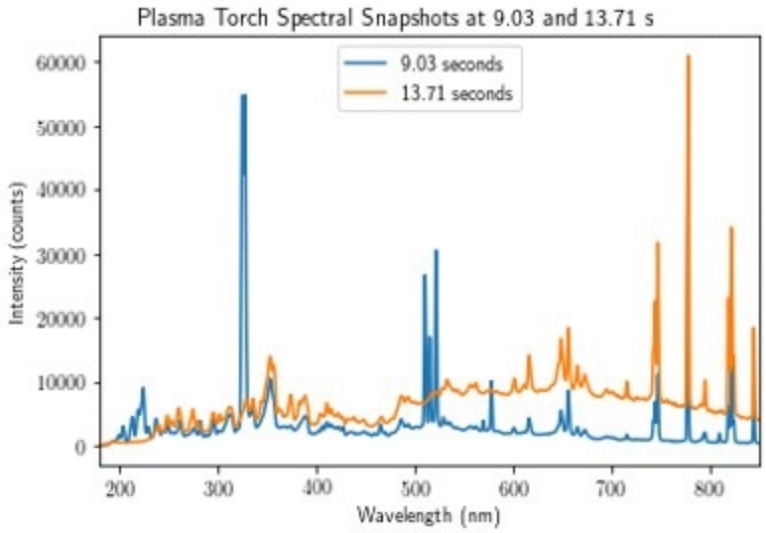

FIGURE 4.37: Baseline spectra of plasma torch using Black Comet.

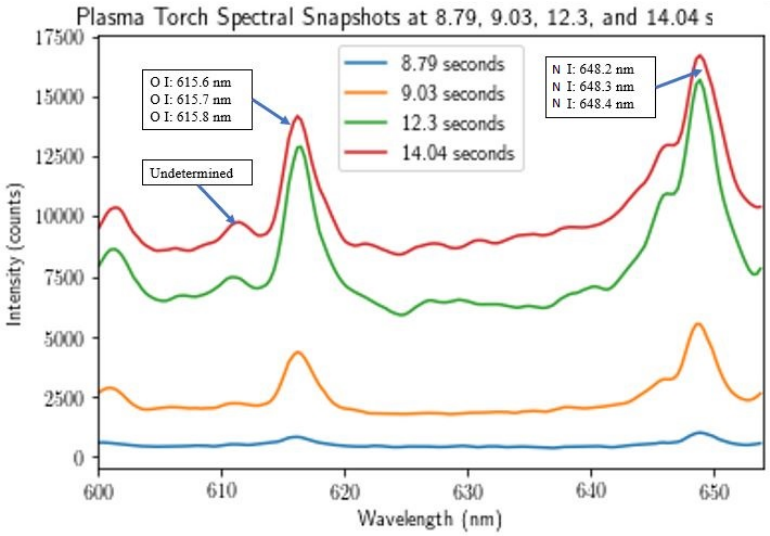

FIGURE 4.38: Air plasma torch spectrum from 600 nm to 655 nm for multiple time stamps.

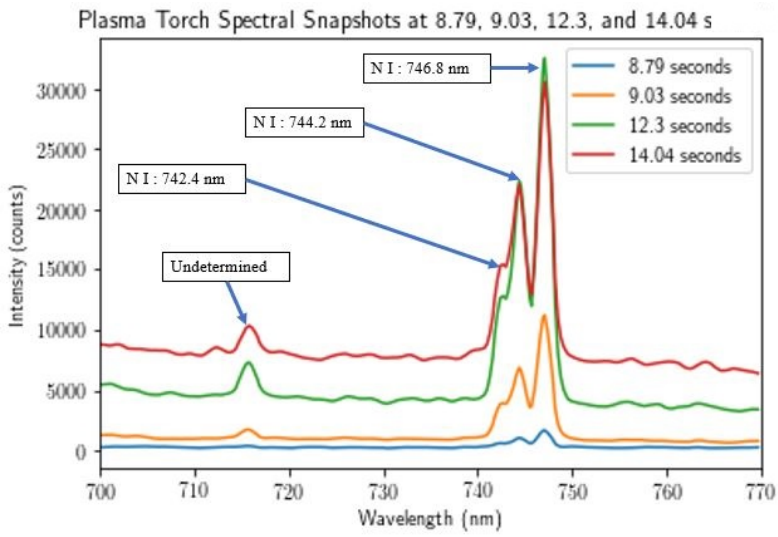

FIGURE 4.39: Air plasma torch spectrum from 700 nm to 770 nm for multiple time stamps.

Table 4.6 lists all of the nitrogen and oxygen peaks found in Figures 4.38 through 4.40.

TABLE 4.6: Tablulation of nitrogen and oxygen lines found from plasma torch spectra.

Nitrogen Species	Wavelength	Oxygen Species	Wavelength
Nitrogen I	648.1706	Oxygen I	615.598 nm
Nitrogen I	648.2699	Oxygen I	615.677 nm
Nitrogen I	648.3573	Oxygen I	615.818 nm
Nitrogen I	742.364	Oxygen I	715.670 nm
Nitrogen I	744.229	Oxygen I	777.1944 nm
Nitrogen I	746.831	Oxygen I	777.4166 nm
Nitrogen I	818.487	Oxygen I	777.5388 nm
Nitrogen I	818.802	Oxygen I	822.182 nm
Nitrogen I	821.634	Oxygen I	844.6247 nm
Nitrogen I	822.314	Oxygen I	844.6359 nm
Nitrogen I	824.239	Oxygen I	844.6758 nm

From the four lone nitrogen peaks found in the torch spectra, a Saha plot was generated in Figure 4.41. As usual, the most accurate values for wavelength and transition probability were obtained from the NIST atomic database [37]. The positive slope of the Saha plot suggests an "unphysical" negative temperature. No lone oxygen peaks were found out of the wavelength intervals investigated so a Saha plot could not be generated with the oxygen lines.

4.4.3 Identification of Contaminant Emission Lines from Experimental Spectra

The addition of contaminants to a metal sample is expected to add additional emission lines and peaks to the baseline spectrum. Recall that three sets of data were obtained:

1. Baseline: the bare metal sample with no additional contaminants.
2. Potassium iodide: the metal sample with potassium iodide salt grains glued to the sample using Foam Glue produced by Bob Smith Industries.
3. Cesium iodide: the metal sample with cesium iodide salt grains glued to the sample using Foam Glue produced by Bob Smith Industries.

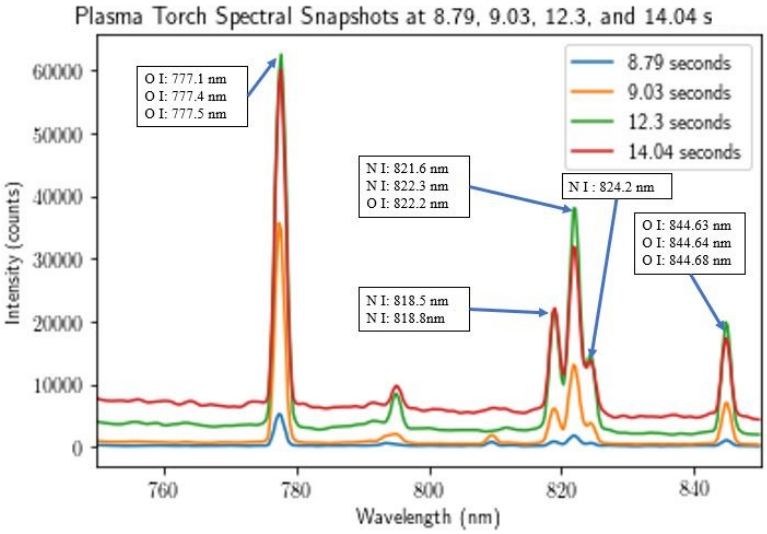

FIGURE 4.40: Air plasma torch spectrum from 750 nm to 845 nm for multiple time stamps.

Wavelength (nm)	Intensity (Counts	Transition Probability (s^-1)	Excited state Energy (eV)	LN (unitless)
742.364	30000	2.26E+07	11.9955753	-0.014668115
744.229	22000	4.76E+07	11.9955753	-1.067196804
746.831	15000	7.84E+07	11.9955753	-1.945690084
824.239	15000	5.24E+07	11.8397086	-1.444151133

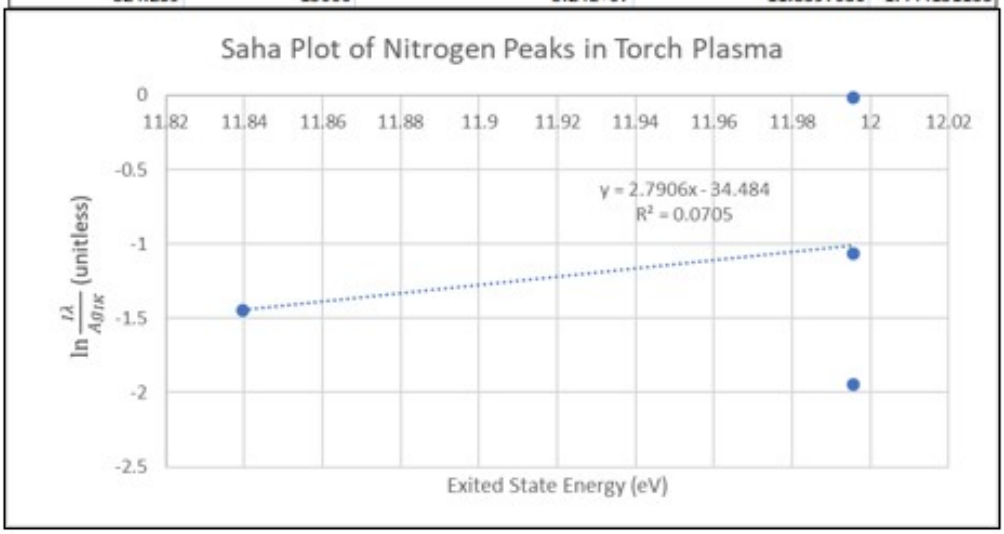

FIGURE 4.41: Saha plot estimating cutting torch plasma temperature from nitrogen emission lines.

Comparing spectra from the same wavelength region from all three sets of experiments allowed for contaminant emission lines to be identified. The spectra from the three data sets had many peaks, but differences that appeared between them are what was relevant. Figure 4.37 acts as a "control". Any additional elements added in the form of contaminants may be deduced by searching for additional peaks. Those additional peaks may be associated with one or more emission lines. These lines may come from a mix of elements, or from a single element whose emission lines may happen to fall in a similar wavelength region. The ability to distinguish between lines depends on the instrumentation. The Black Comet, which was used for the majority of these experiments has a more limited resolution, but is capable of capturing multiple spectra over a short length of time. In many of the spectra shown in this section, multiple time instances will be displayed for each data set. If peaks appear in the spectra over multiple time instances, this adds confidence that those peaks actually are being measured, rather than being associated with instrument error.

T properly deduce cesium and iodine lines from the data sets, the chemical elements associated with each line must be determined, as the torch plasma will consist of many chemical elements in comparison to the argon plasma. Table 4.7 describes the elemental contents of each sample type. The composition of glue used to glue on the contaminants is roughly known. According to the manufacturer, it is silicon-based, and contains traces of organic alcohols (elements C,H and O). With the possible elements known for each data set, the list of possible elements is reduced. Figures 4.44 through 4.49 compare the same wavelength intervals as those explored for the cesium iodide-contaminated argon plasma experiments. This was done in order to be able to determine the cesium and iodine emission lines in common for the contaminated experiments.

Spectra from cutting KI and CsI-contaminated metal.

Figures 4.42 and 4.43 show the full-scale spectral measurements when the cutting of the mock-contaminated metal took place. Note the elevated baselines in some cases.

TABLE 4.7: Table that compares the contents of the plasma torch experimental data sets.

Sets	Steel (Fe, etc)	Air Plasma (N, O, etc.)	Glue: (Mostly Si + C,H,O)	Potassium: K	Cesium: Cs	Iodine I
Baseline: Steel	X	X				
KI + Glue + Steel	X	X	X	X		X
CsI + Glue + Steel	X	X	X		X	X

Figures 4.44 to 4.46 compare snapshots of emission spectra measured from the plasma torch in a finite wavelength range. It should be noted here that the absolute intensities of the spectra vary from one snapshot to another. This is due to the variable positioning of the fibre optic cable with respect to the plasma formed by the torch. As a result, it was recommended to pay attention to the relative intensity of lines when identifying the peaks and emission lines.

There are several notable peaks in Figure 4.44. These will be referred to as the "background peaks". Two additional peaks were observable, and are associated with potassium in Figure 4.45. In Figure 4.46, a box is drawn over in the region where one of the background peaks appears, but it is at a small intensity. Multiple lines associated with iodine and cesium, both neutral and ionic, could be identified.

Figures 4.47 through 4.49 compare the baseline, potassium iodide and cesium iodide torch spectra for the other wavelength intervals for the cesium iodide-contaminated argon plasma experiments. Transparent shapes are drawn around the visible peaks to mark them. Additional peaks from the KI or CsI experiments in those figures were not found. This is attributed to the baseline being elevated in some wavelength regions, which may mask emission lines from the contaminants.

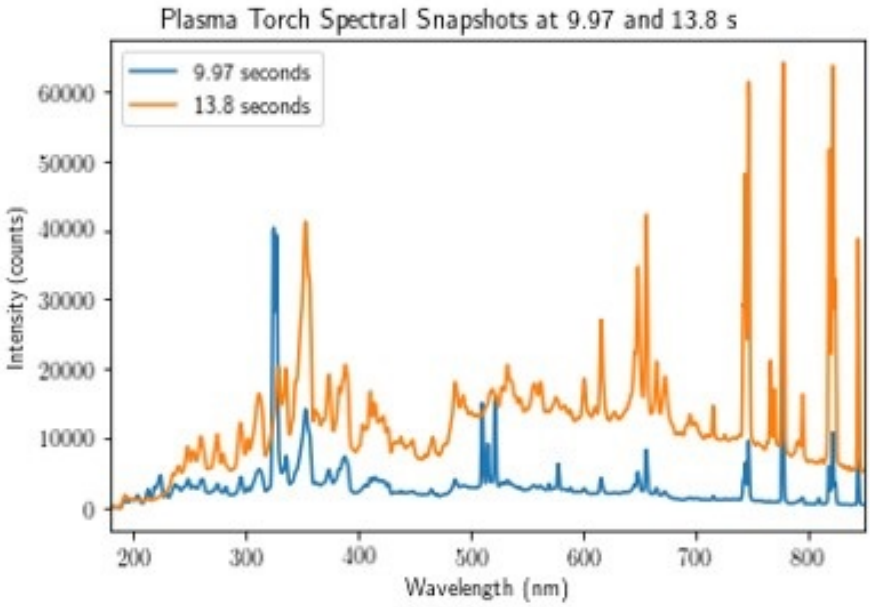

FIGURE 4.42: Full-scale spectrum measured from the experiment where KI-contaminated metal sample is cut.

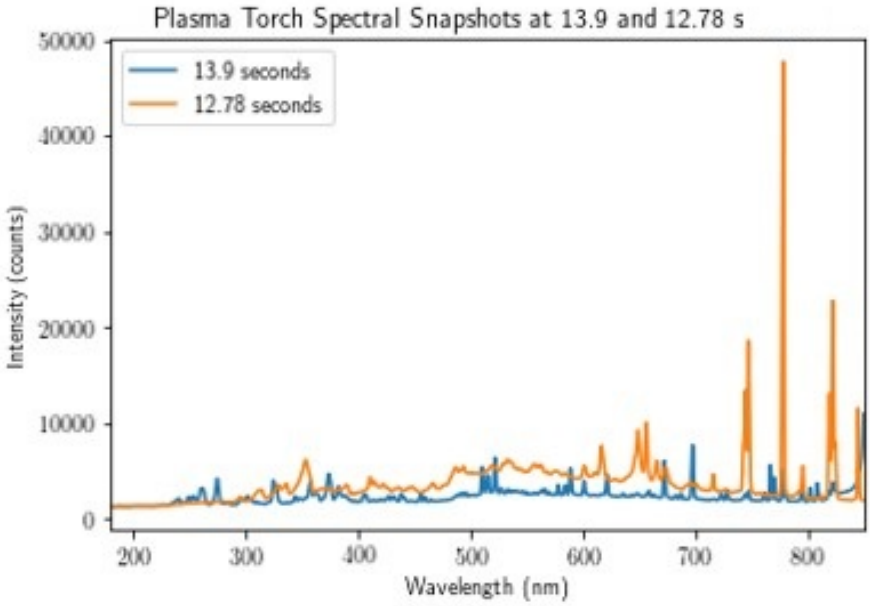

FIGURE 4.43: Full-scale spectrum measured from the experiment where CsI-contaminated metal sample is cut.

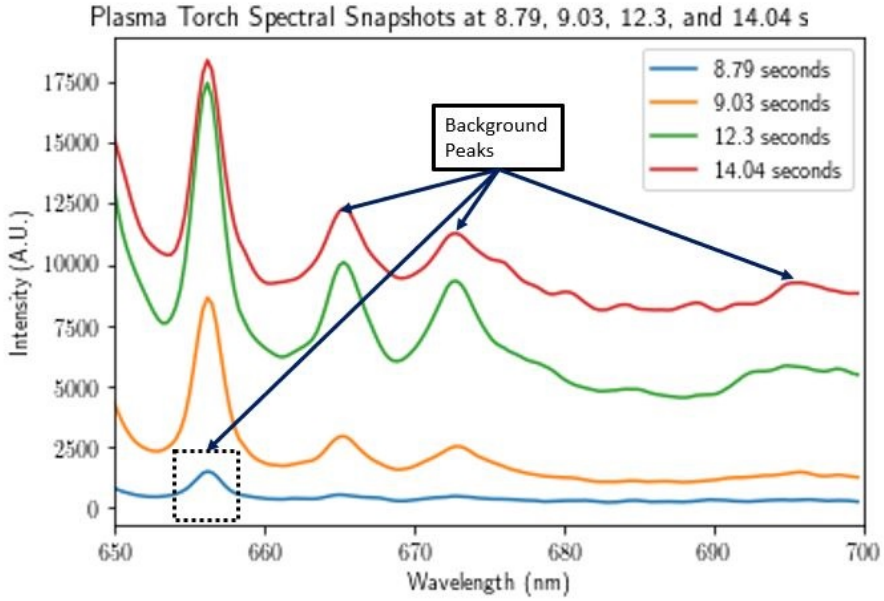

FIGURE 4.44: Plasma torch baseline spectrum from 650 nm to 700 nm.

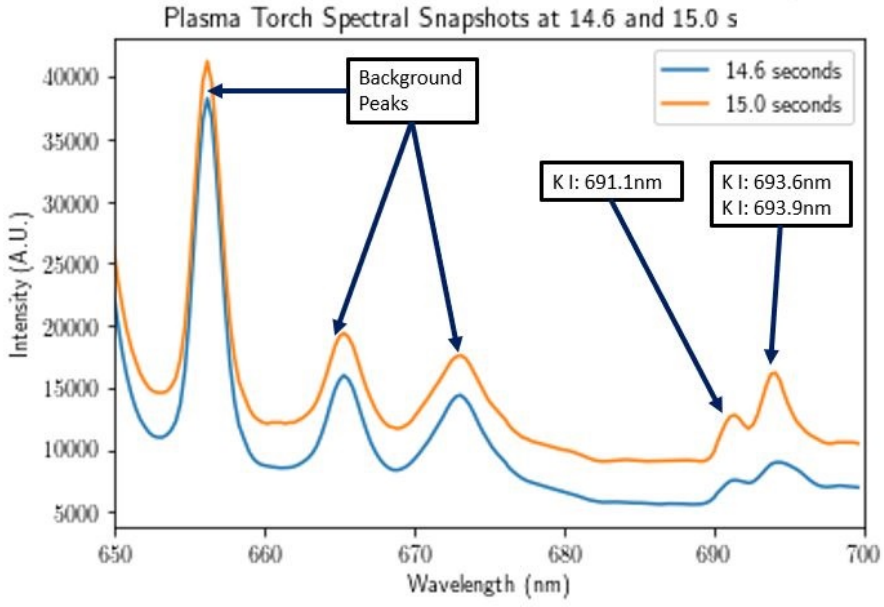

FIGURE 4.45: Spectrum produced by cutting metal contaminated with potassium iodide, from 650 nm to 700 nm.

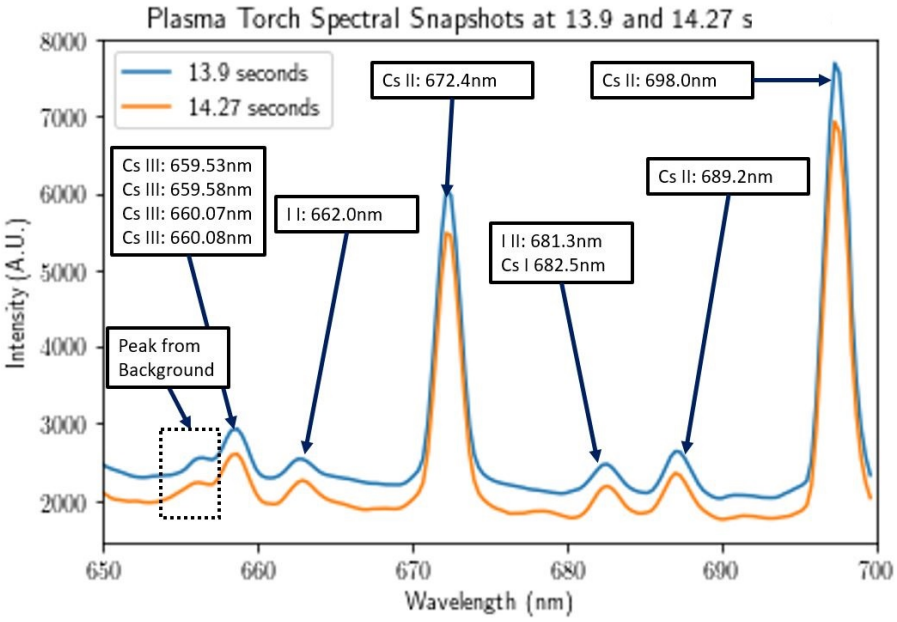

FIGURE 4.46: Spectrum produced by cutting metal contaminated with cesium iodide, from 650 nm to 700 nm.

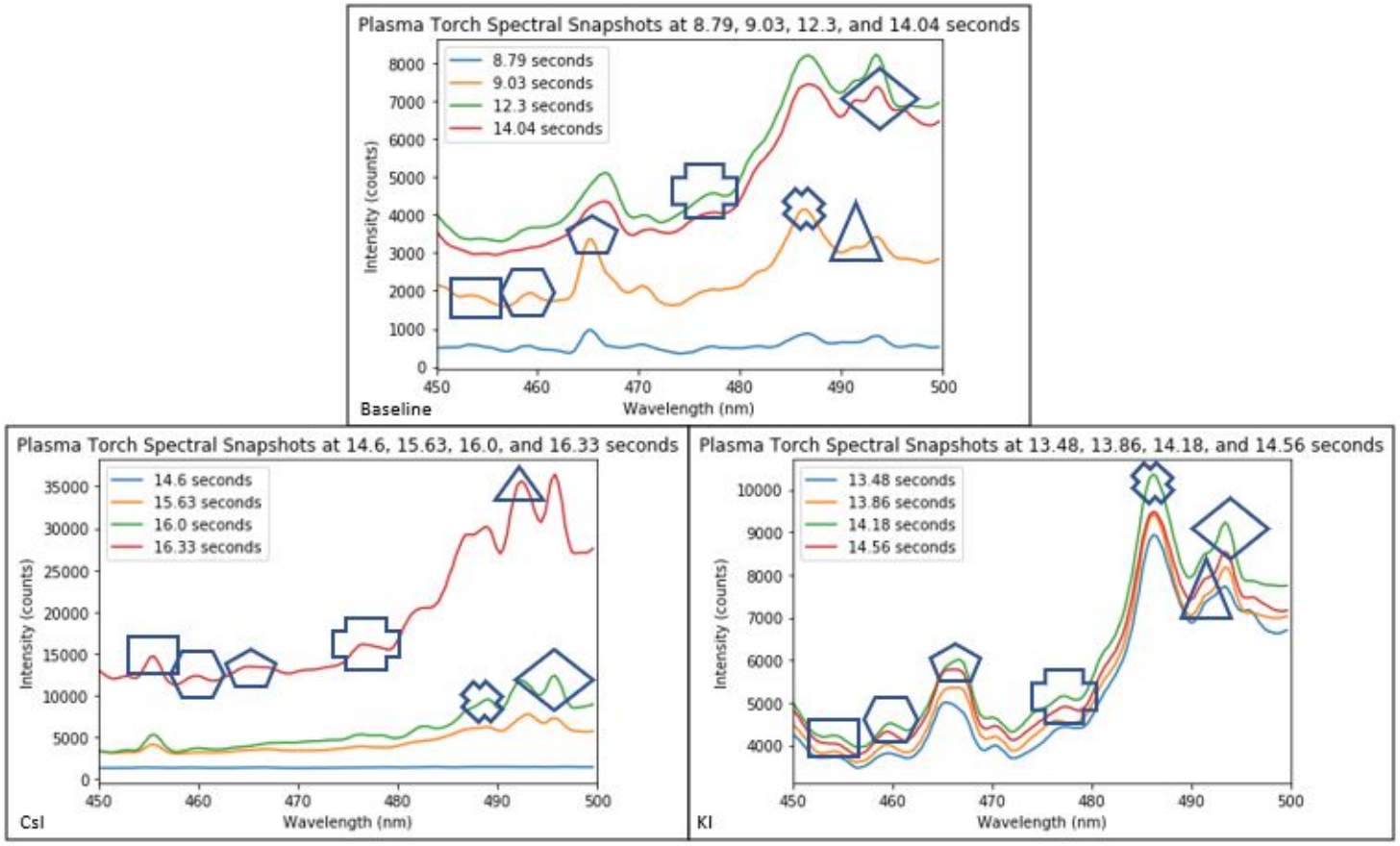

FIGURE 4.47: Comparison of baseline, KI-contaminated sample cuts and CsI-contaminated sample cuts from 450 nm to 500 nm.

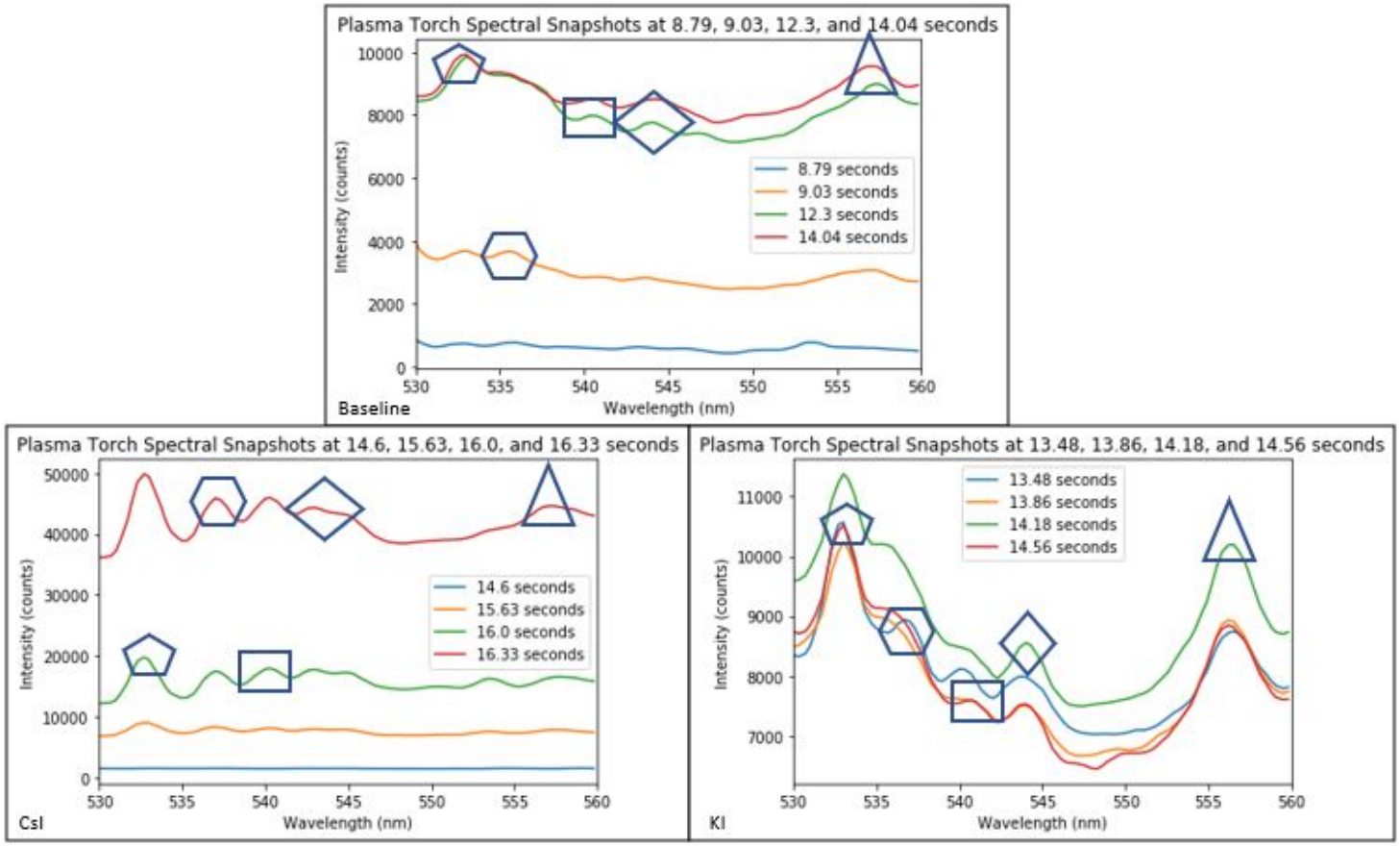

FIGURE 4.48: Comparison of baseline, KI-contaminated sample cuts and CsI-contaminated sample cuts from 530 nm to 560 nm.

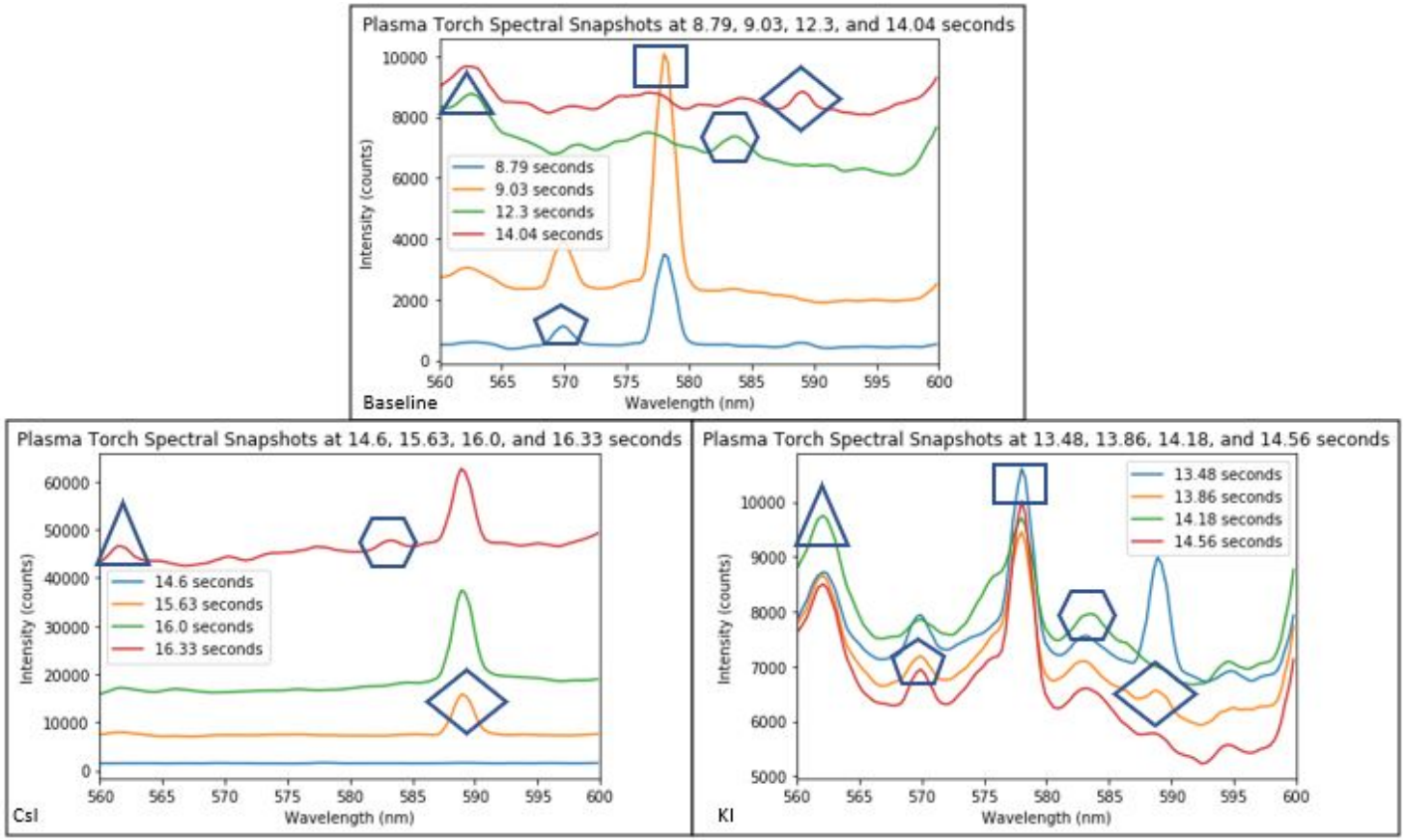

FIGURE 4.49: Comparison of baseline, KI-contaminated sample cuts and CsI-contaminated sample cuts measured by Black Comet from 560 nm to 600 nm.

Table 4.8 tabulates all of the emission lines observed in the cesium iodide-plasma torch experiments. There are neutral and first ionization species of iodine that are present in the plasma, as well as neutral, first ionization state, and second ionization state species of cesium that are present.

TABLE 4.8: Tablulation of cesium and iodine lines measured from CsI-contaminated sample cuts measured by Black Comet.

Cesium Species	**Wavelength**	**Iodine Species**	**Wavelength**
Cesium III	659.53 nm	Iodine I	662.0 nm
Cesium III	659.58 nm	Iodine II	681.3 nm
Cesium III	660.07 nm		
Cesium III	660.08 nm		
Cesium I	672.3 nm		
Cesium II	672.4 nm		
Cesium I	682.5 nm		
Cesium II	689.2 nm		

This chapter has described the observations, characterizations, and spectroscopic measurements from the microwave argon plasma experiments and plasma torch experiments. Emission lines associated with the plasma species have been identified, along with emission lines from cesium iodide contaminants introduced into each respective system.

Chapter 5

Discussion

5.1 Relevant Physical Reactions in Argon Plasma Experiments

This section outlines the process of how the argon plasma was produced using the microwave system. Equations 5.1 through 5.7 outline a process of argon plasma production in the microwave system, and how the cesium iodide salt is broken apart when introduced in some experiments. The equations here are based on past experimental work by Harvel et. al. [17] and theoretical work by Beuthe [20]. Most of these reactions are expected to occur at various rates and amounts based on experimental parameters such as temperature. The sets of reactions that follow should not be assumed to be a complete set of reactions that occur within the apparatus. They are there to help explain what is expected to occur in plasma production, and what is expected to occur when cesium iodide contamiannts are introduced into the plasma.

When the argon gas flow was started through the test section, the magnetron was prompted to produce microwaves which heats up the plasma seed. The plasma seed would then release energetic electrons in the heating process as a result (not ionization). It should be noted too that the electrons themselves would also be affected by the microwaves and would have had increased kinetic energy and momentum as they interacted with microwaves.

$$\begin{aligned} C \text{ (microwave heating)} &\rightarrow C^{+} + e^{-} \\ e^{-} + microwave &\rightarrow e^{-} \text{ (Momentum imparted to } e^{-}) \end{aligned} \tag{5.1}$$

These electrons then collided with the argon gas which transfered momentum to argon such as in equation 5.2.

$$e^{-} + Ar \rightarrow e^{-} + Ar \text{ (Momentum imparted to Ar)} \tag{5.2}$$

These collisions caused electronic excitations such as in equation 5.3. As a note, Ar^{*} and Ar^{**} denote excited and metastable states, respectively.

$$\begin{aligned} e^{-} + Ar &\rightarrow Ar^{*} + e^{-} \\ e^{-} + Ar &\rightarrow Ar^{**} + e^{-} \end{aligned} \tag{5.3}$$

Collisions between argon atoms also caused electronic excitations such as in 5.4

$$Ar + Ar \rightarrow Ar + Ar^{*}/Ar^{**} \tag{5.4}$$

These excited states then gradually de-excited over time based on their transition probability (lifetimes), which resulted in the release of a photon. It is these photons that were measured by the spectroscopy systems.

$$\begin{aligned} Ar^{*}/Ar^{**} &\rightarrow Ar + h\nu(photon) \\ Ar^{+*} &\rightarrow Ar^{+} + h\nu(photon) \\ Ar^{+} + e^{-} &\rightarrow Ar + h\nu(photon) \end{aligned} \tag{5.5}$$

When contaminants were introduced into the setups, there were other reactions that occured. For this work, cesium iodide was introduced. Excited states that interacted with the cesium iodide solids imparted their energy to the salt and broke the ionic bond, releasing atomic cesium and iodine.

$$Ar^*/Ar^{**} + CsI \rightarrow Ar + Cs + I \tag{5.6}$$

The interaction of the cesium and iodide atoms with excited states of argon can result the ionization of the iodine and cesium atoms, ionizing them. These are Penning ionization reactions that are expected to have caused ionizations of the cesium and iodine atoms, as they are atomized into the plasma. Similarly, excitated states of cesium and iodine would have been produced with collisions such as with the argon in the plasma.

$$\begin{aligned} Ar^*/Ar^{**} + I &\rightarrow Ar + I^+ + e^- \\ Ar^*/Ar^{**} + Cs &\rightarrow Ar + Cs^+ + e^- \end{aligned} \tag{5.7}$$

5.2 Interpretation of Argon Plasma Experimental Results

This section serves to interpret the main takeaways from the experiments pertaining to the characterization of the pure argon plasma.

The Saha plot temperature characterization method functions but results in large uncertainties that prevent the distinguishing between temperature values when input microwave power is increased or decreased. These uncertainties are associated with the uncertainties in the lines of fit, which are a result of (relative) uncertainties in the intensity measured by the monochromator, and the uncertainty in the transition probability A_{ki}. The former is an uncertainty that may be decreased with changes in experimental parameters. The latter is one that cannot be decreased as it is independent of experimental parameters. The fact that the Saha plots produce a temperature value within a reasonable relative uncertainty (i.e. the relative uncertainty is less than one) does suggest that the plasma produced is in thermal equilibrium.

5.2.1 Emission Line Intensities

A hysteresis effect is visible in the argon plasma as microwaves are produced. The plot of peak intensity as a function of input power as in (Figure 4.9) shows a hysteresis effect in plasma, relative to input power. The intensity values when transitioning to a higher microwave power, from a lower input power, and back down to the original, are generally not the same at either end. One experiment with these experimental parameters was conducted, so repeatability will need verification.

It should also be noted that a general increase in peak intensities were observed with the increase in input microwave power, in Figure 4.8 and 4.9. While the temperature of the plasma may not be shown to increase as a function of power (Figure 4.7), the energy imparted to the plasma is known to be moving elsewhere, such as into producing more excited electronic states. This is desirable, as these electronic states will propel Penning ionization reactions and reactions that break apart the cesium iodide salt bonds.

Many of the argon emission lines identified result in metastable states. The presence of these species, and the fact that their population increases with input power, is seen in Figure 4.9. This suggests that Penning ionization reactions, which were expected to drive the ionization of the cesium iodide salts, may also increase with input power when contaminants are introduced.

5.2.2 Breakdown of contaminants

As seen in Chapter 2, the enthalpy of formation for a single molecule of cesium iodide is $3.59eV$, according to the Chemical Rubber Company handbook [41]. In short, the metastable states of argon have more than sufficient energy to break a cesium iodide bond if they are to interact with it. Recall that all excited states of argon above the ground state are above $3.59eV$ according to the NIST Atomic Spectra Database. [36].

In Figure 4.33, the correlation between the metastable emission line and the iodine and cesium lines may imply that Penning ionization (and metastable state

interactions) are mechanisms for breaking apart the cesium iodide salt and for producing cesium and iodine atoms/ions.

The changes in plasma jet height with different flow rates will likely be relevant to the number of Penning ionizations that take place: the longer the jet, then there may be a higher probability for freed contaminants to interact with the excited species that make up the jet. The control over the jet height using flow rates and input powers will allow for the simulation of different torch flame sizes as well. This can be investigated further, such as measuring emission line intensity as a function of flow rate, and measuring the line intensity at other regions of the plasma, rather than just through the viewports.

5.2.3 Contaminant deposition

The transparency of the test sections for the microwave argon plasma experiments allowed for the observation of deposition patterns of cesium and iodine that clearly evolve over time such as in Figure 4.26. These deposition patterns are attributed to thermophoresis: the plasma jet is expected to have a temperature gradient. This temperature gradient is expected to roughly decrease from the microwave focal point as the gas travels away from the microwave focal point. The temperature gradient is also expected to decrease radially: higher in the center and lower at the edges due to the flow of the gas.

The separation of the iodine and cesium one another may be attributed to the differences in the size and mass of the elements. Natural iodine has an attributed atomic mass of $126.9\,\mathrm{g\,mol^{-1}}$ whereas naturally occurring cesium has an atomic mass of $132.9\,\mathrm{g\,mol^{-1}}$. It is also known that cesium atoms have a lower atomic radius than iodine, therefore (with all else being equal) would be expected to diffuse differently to some extent. For example, collisions with a species of lower atomic radii (therefore lower collision cross-section) occur at a lower probability.

5.2.4 Behaviour of contaminated Argon Plasma

The contaminated argon plasma had different behaviour. Relative to the pure plasma, the contaminated plasma appeared more opaque and appears less bright

(Figures 4.24 and 4.25). There's concentrations of other species within the plasma that are absorbing some of the light produced by the plasma. This suggests that the plasma is not an argon plasma that has a "small" contamination of cesium and iodine, but that the concentration of contaminants is large enough to alter the characteristics of the plasma. This suggests that the plasma could be considered a dusty plasma. There are additional contents to the plasma. These contents deposit and solidify on the edges of the experimental appratus and are mixed in with the plasma. There is known to be different behavior between generic single-species plasmas, and therefore requires more investigation: the assumption of thermal equilibrium that was used to characterize the temperature of the pure argon plasma may not hold, as if the plasma now produced is a dusty plasma, then those types of plasmas typically are not at thermal equilibrium and other assumptions may not hold. This dusty plasma is similar to the environment that will be produced by the torch with the addition of metal and contaminant species.

5.3 Interpretation of Torch Plasma Results

5.3.1 Emission lines from the air

The torch plasma is confirmed to be an air plasma, based on the nitrogen and oxygen lines found. The temperature estimation using nitrogen emission lines to produce a Saha plot temperature produced a non-physical temperature value. This is likely due to the torch plasma not being in thermal equilibrium, but also can be attributed to the baseline of the spectra being uplifted due various effects such as thermal radiation (Figure 4.37).

5.3.2 Emission lines from contaminants

The experiments involving the plasma torch cutting of contaminated metal samples produced evidence of atomic cesium and iodine species in the plasma. Additionally, the presence of ionic species, first and second ionization states, suggests that the torch plasma is sufficiently energetic to ionize cesium not once, but twice.

5.3.3 Elevation of baseline spectra

There are multiple causes that can be attributed to the lumps in the spectra. Firstly, the large number of possible emission lines due to air multiple elements. Each element will have many emission lines. These emissions may crowd the spectral measurements. As seen with the argon plasma spectra produced by the Black Comet (Figure 4.4), the high intensity lines that have similar wavelengths may bleed into each other. Another possibility is that the positioning of the cable relative to the plasma may also vary between experiment, and even over time. This is illustrated in Figure 3.35, which sketches how the fibre optic cable measures the spectra produced by the plasma. A small shift in the plasma position may cause part of the glow from the plasma to shift out of view of the fibre optic cable's thin window, or for the intensity to increase if the plasma moves closer to the cable.

5.4 Comparison of results

Both plasma experiments provide some insight into the release of radionuclides during the cutting process through the observation of atomized forms of the mock-contaminants, as well as their movement. The microwave argon plasma setup shows clear deposition patterns for the separated cesium and iodine. The cutting experiments demonstrate the production of sparks and other debris that can spread.

5.4.1 Emission lines in common

Table 5.1 shows the common emission lines of the cesium and iodine contaminants between both setups. There are some lines in common that are detected but not all. This may be due to the elevation of the baseline spectra as discussed earlier. The lack of lines in common does not suggest that the torch is not atomizing and ionizing iodine and cesium to the same degree that the argon plasma does. One set of emission lines that are in common are the second ionization state lines of cesium. This suggests that the torch plasma is capable of atomizing and ionizing cesium

iodide and its constituent atoms in the same way, and that other interference can be attributed to reasons why other lines in common are not observed.

TABLE 5.1: Table of common cesium and iodine emission lines found between argon and torch plasma experiments.

Cesium Species	Wavelength	Iodine Species	Wavelength
Cesium III	659.53 nm	Iodine I	662.0 nm
Cesium III	659.58 nm	Iodine II	681.3 nm
Cesium III	660.07 nm		
Cesium III	660.08 nm		
Cesium I	672.3 nm		
Cesium II	672.4 nm		
Cesium I	682.5 nm		

5.4.2 Contaminant spread

In both experiments, the presence of atomic and ionic iodine and cesium were observed in the spectral measurements. In the case of the argon plasma, the physical separation of the cesium and iodine was also observed as they deposited on the edges of the test section farther up from where the plasma was produced. In short, both plasmas were effectively atomizing the cesium iodide salt into its chemical constituents, and these atomized constituents are released and are spreading: depositions on the side of the argon plasma test sections, and through sparks and debris as produced by the plasma torch. Understanding the spread pattern of the contaminants in the argon plasma setup will allow for capture techniques to be tested on that system first, rather than considering capture techniques from the torch experimental setup.

5.5 Simulation of torch plasma with Argon plasma setup

The presence of ionic cesium and iodide were observed in the spectral measurements of both plasma experiments. This carries some significance as there exists technologies like electrostatic filtration that exploit the charged nature of the contaminants to efficiently capture them than if they were neutrally

charged. In combination with the deposition patterns in the argon plasma test section, and the fact that they simulate torch conditions in the sense that the same contaminant ion species are produced and that the microwave plasma produces a dusty plasma, a focus can be made on developing capture techniques with the microwave plasma system, which is a system that has higher degrees of control over conditions.

5.6 Fulfillment of Thesis Goals

All of the objectives of this thesis, as outlined in the introduction chapter, can be said to have been fulfilled.

1. Produce a controlled argon plasma as generated by a microwave system.
2. Characterize an uncontrolled plasma as generated by a plasma torch system.
3. Characterize the argon plasma, and explore methods of characterizing its temperature.
4. Introduce non-radioactive equivalents of cesium and iodide into the controlled plasma, and to observe the outcomes.
5. Explore methods on how to simulate the dismantlement of a contaminated component using an off-the shelf plasma torch.

Objectives 1, 3 and 4 were completed using the microwave plasma system. A stable argon plasma was produced. Qualities such as jet height and temperature were explored as a function of input power, and input gas flow rate in some instances. Plasma jet height increased with input power and flow rate. Input power had an effect on plasma temperature, although statistical uncertainty made any trends unclear. The sensitivity of the plasma to waveguide system tuning was also explored in terms of how settings affected plasma the jet height and the intensity of certain peaks. cesium iodide contaminants introduced into the plasma were detected using emission spectroscopy, and were directly observable as spatially-dependent depositions on the edges of the test sections. It

was verified that the argon plasma is capable of readily breaking atomizing and ionizing cesium iodide solids. The plasma is stablely formed, and has many controllable parameters such as input power.

Objectives 2 and 5 were successfully completed using the plasma torch mock setup. The torch plasma, while cutting contaminated and non-contaminated samples had their spectra measured spectroscopically. When cutting a mock-contaminated sample, the presence of contaminants in the plasma was measured by detecting emission lines in the resultant plasma: neutral forms of cesium and iodide, first ionization states of cesium and iodide, and third ionization states of cesium.

Chapter 6

Concluding Remarks

This work has completed a study of microwave-generated plasmas and plasma torch experiments using spectroscopic methods with the purpose of applications towards nuclear decommissioning. As a result of this work, the following concluding remarks are made:

- The argon plasma produced in the microwave waveguide system has been characterized by its temperature and scale. The intensity of emission lines were measured as a function of effects of system parameters such as tuning and input microwave power.

- When cesium iodide was introduced to the argon plasma, a dusty plasma was produced: a mix of the Argon plasma and the contaminants. This a type of plasma that would be expected to be produced in decommissioning scenarios: a dusty plasma that consists of the torch plasma, airborne forms of the contaminants and metal components. This shows that the setup using the argon plasma can simulate decommissioning processes.

- The presence of atomic and ionic cesium and iodide is determined using spectroscopic techniques. The setup demonstrates deposition of cesium and iodine products on the edges of the glass tubing.

- A commercial plasma torch was used to simulate dismantlement processes, where a metal sample contaminated with cesium iodide contaminants is cut. Spectroscopic techniques used prove that concentrations of cesium and iodide are being atomized and ionized by the torch plasma, and that this

method of measuring presence of contaminants can be repeated with other contaminants.

- This work has demonstrated a proof of concept, developing a method to produce a plasma with large degree of control and is capable of simulating plasma environments in decommissioning scenarios.

6.1 Future Work

With the long-term objective of developing capture techniques for different types of plasmas in mind, the setups used here can be extended in several ways:

- The plasma torch as well as the microwave system can use different working gasses used. For instance, an argon supply may be connected to the commercial plasma torch instead of an air supply.
- The types of contaminants introduced can be extended to a larger selection: those that are expected to be encountered in decommissioning scenarios, such as Cobalt and Iron.
- With different contaminants introduced, the study of their capture using a selection of filtration techniques can be done.

Appendix A

NIST Database Emission Line Information

With a simplified materials and methods section, the tables of emission lines consulted in this work are extracted from the NIST atomic spectra database[37] . The emission line tables are divided by the experiments performed.

A.1 Argon Plasma Experiments

A.1.1 Relevant Details of Argon Emission Lines Observed in this Work

All of the emission lines detected in experiments and used in the argon plasma Saha Plots were in the 696 nm to 978 nm range. Figures A.1 and A.2 provide a compilation of emission line information: their wavelength λ, an intensity estimate, excited and relaxed state energy E_i and E_k (respectively), and transition probability Ag_{ki} for argon emission lines in the wavelength range. This also features the estimate of uncertainty for Ag_{ki} in a letter grade.

The ionic species of argon are described with a Roman numeral. Neutral species are denoted as "argon I", first ionization states of argon are denoted as "argon II", and so on.

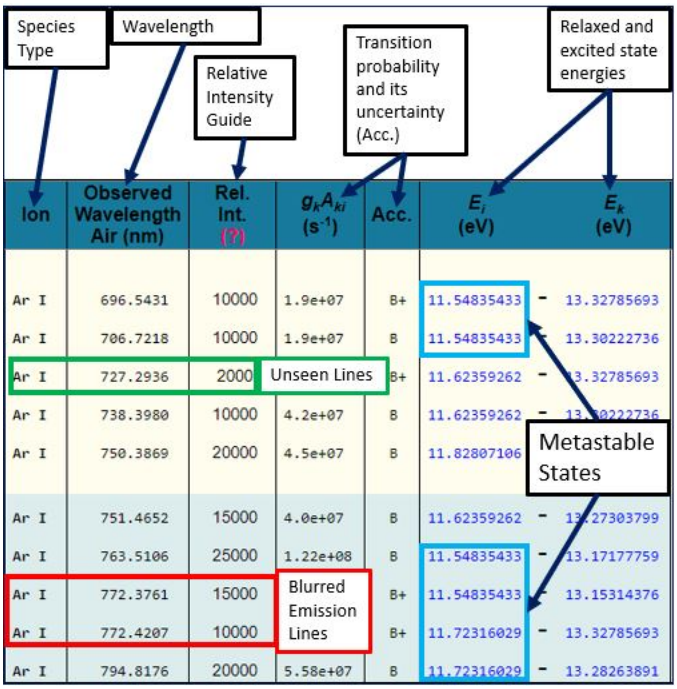

Ion	Observed Wavelength Air (nm)	Rel. Int. (?)	g_kA_{ki} (s^{-1})	Acc.	E_i (eV)	E_k (eV)
Ar I	696.5431	10000	1.9e+07	B+	11.54835433	13.32785693
Ar I	706.7218	10000	1.9e+07	B	11.54835433	13.30222736
Ar I	727.2936	2000	1.9e+07	B+	11.62359262	13.32785693
Ar I	738.3980	10000	4.2e+07	B	11.62359262	13.30222736
Ar I	750.3869	20000	4.5e+07	B	11.82807106	13.47303799
Ar I	751.4652	15000	4.0e+07	B	11.62359262	13.27303799
Ar I	763.5106	25000	1.22e+08	B	11.54835433	13.17177759
Ar I	772.3761	15000	1.1e+08	B+	11.54835433	13.15314376
Ar I	772.4207	10000	1.1e+08	B+	11.72316029	13.32785693
Ar I	794.8176	20000	5.58e+07	B	11.72316029	13.28263891

FIGURE A.1: Detailed list of argon emission lines from 696 nm to 795 nm. Adapted from [37].

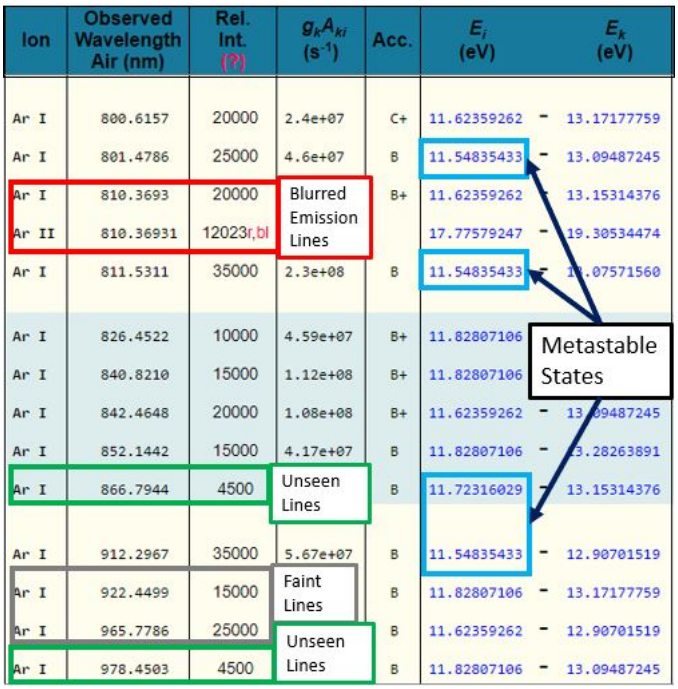

Ion	Observed Wavelength Air (nm)	Rel. Int. (?)	g_kA_{ki} (s^{-1})	Acc.	E_i (eV)	E_k (eV)
Ar I	800.6157	20000	2.4e+07	C+	11.62359262	13.17177759
Ar I	801.4786	25000	4.6e+07	B	11.54835433	13.09487245
Ar I	810.3693	20000	Blurred Emission Lines	B+	11.62359262	13.15314376
Ar II	810.36931	12023r,bl			17.77579247	19.30534474
Ar I	811.5311	35000	2.3e+08	B	11.54835433	13.07571560
Ar I	826.4522	10000	4.59e+07	B+	11.82807106	
Ar I	840.8210	15000	1.12e+08	B+	11.82807106	
Ar I	842.4648	20000	1.08e+08	B+	11.62359262	13.09487245
Ar I	852.1442	15000	4.17e+07	B	11.82807106	13.28263891
Ar I	866.7944	4500	Unseen Lines	B	11.72316029	13.15314376
Ar I	912.2967	35000	5.67e+07	B	11.54835433	12.90701519
Ar I	922.4499	15000	Faint Lines	B	11.82807106	13.17177759
Ar I	965.7786	25000		B	11.62359262	12.90701519
Ar I	978.4503	4500	Unseen Lines	B	11.82807106	13.09487245

FIGURE A.2: Detailed list of argon emission lines from 801 nm to 978 nm. Adapted from [37].

A.1.2 Strong Lines of Carbon Due to Plasma Seed

The NIST database also features lists of "strong" emission lines. These "strong" lines are those that are expected to be measured to have the highest intensity in comparison to other possible emission lines of any given species [37]. The plasma seed that is used as part of the test section contains carbon. Figure A.3 list strong lines produced by carbon that may appear in the spectra.

Intensity	Air Wavelength (Å)	Spectrum
400	2478.561	C I
500	2836.710	C II
400	2837.603	C II
400	2992.618	C II
300	3918.978	C II
400	3920.693	C II
400	4267.003	C II
500	4267.258	C II
300	5145.16	C II
200	5151.09	C II
150	5380.34	C I
300	5889.77	C II
150	6013.22	C I
400	6578.05	C II
300	6582.88	C II
400	7231.32	C II
500	7236.42	C II
250	8335.15	C I

FIGURE A.3: List of strong carbon emission lines. Taken from [37]

A.1.3 Strong Lines of Contaminants and Other Elements

Cesium and iodine were introduced into the test sections in some experiments. Figures A.4 and A.5 feature lists of cesium lines, and Figure A.6 lists strong iodine lines.

Cesium

Intensity	Air Wavelength (Å)	Spectrum
15	2267.65	Cs II
8	2273.84	Cs II
14	2332.46	Cs II
10	2392.86	Cs II
15	2931.08	Cs II
11	3785.44	Cs II
25	3805.12	Cs II
30	3876.15	Cs I
10	3888.61	Cs I
30	3896.99	Cs II
40	3959.51	Cs II
25	3965.20	Cs II
20	3974.25	Cs II
80	4039.85	Cs II
20	4068.78	Cs II
20	4213.14	Cs II
20	4232.20	Cs II
10	4234.41	Cs II
140	4264.70	Cs II
200	4277.13	Cs II
50	4288.38	Cs II
80	4363.30	Cs II
40	4373.04	Cs II
40	4405.26	Cs II
120	4501.55	Cs II
200	4526.74	Cs II
40	4538.97	Cs II

Intensity	Air Wavelength (Å)	Spectrum
15	4555.28	Cs I
8	4593.17	Cs I
1000	4603.79	Cs II
40	4616.17	Cs II
70	4763.64	Cs II
250	4830.19	Cs II
200	4870.04	Cs II
50	4880.05	Cs II
400	4952.85	Cs II
80	4972.60	Cs II
250	5043.80	Cs II
70	5209.58	Cs II
800	5227.04	Cs II
300	5249.38	Cs II
110	5274.05	Cs II
100	5349.13	Cs II
200	5370.99	Cs II
1	5465.94	Cs I
1	5502.88	Cs I
400	5563.02	Cs II
2	5635.21	Cs I
3	5664.02	Cs I
50	5814.16	Cs II
250	5831.14	Cs II
1	5838.83	Cs I
5	5845.14	Cs I
500	5925.63	Cs II
10	6010.49	Cs I
1	6034.09	Cs I
100	6128.61	Cs II
15	6213.10	Cs I

FIGURE A.4: First and second list of strong cesium emission lines. Taken from [37]

Intensity	Air Wavelength (Å)	Spectrum
3	6217.60	Cs I
5	6354.55	Cs I
80	6495.53	Cs II
100	6536.44	Cs II
8	6586.51	Cs I
2	6628.66	Cs I
90	6646.57	Cs II
50	6723.28	Cs I
100	6724.47	Cs II
3	6824.65	Cs I
5	6870.45	Cs I
400	6955.50	Cs II
80	6973.30	Cs I
150	6979.67	Cs II
15	6983.49	Cs I
130	7149.54	Cs II
13	7228.53	Cs I
2	7279.90	Cs I
20	7279.96	Cs I
40	7608.90	Cs I
25	7852.52	Cs II
50	7943.88	Cs I
200	7997.44	Cs II
20	8012.98	Cs II
60	8015.73	Cs I
80	8047.13	Cs II
8	8078.94	Cs I
70	8079.04	Cs I

FIGURE A.5: Third list of strong cesium emission lines. Taken from [37]

Intensity	Air Wavelength (Å)	Spectrum
25	2061.63	I I
100	2582.79	I II
250	3078.75	I II
130	5119.29	I I
150	5161.20	I II
150	5245.71	I II
500	5338.22	I II
250	5345.15	I II
150	5435.83	I II
100	5464.62	I II
500	5625.69	I II
100	5690.91	I II
200	5710.53	I II
250	5950.25	I II
100	6074.98	I II
100	6127.49	I II
70	6619.66	I I
200	6812.57	I II
70	7402.06	I I
70	7468.99	I I
130	8043.74	I I
50	8240.05	I I
130	8393.30	I I

FIGURE A.6: List of strong iodine emission lines. Taken from [37]

A.2 Plasma Torch Experiments

A.2.1 Strong Lines from Baseline

Air primarily consists of oxygen and nitrogen. The steel metal samples consist of carbon and iron. The paint is assumed to have a negligible contribution to the spectrum. The list of strong carbon emission lines is the same as that of Figure A.3. The iron lines are in Figures A.7 through A.11. The oxygen lines are in Figure A.12 and the nitrogen lines are in Figure A.13.

Intensity	Air Wavelength (Å)	Spectrum
30	2178.0808	Fe I
30	2259.5103	Fe I
30	2292.5249	Fe I
60	2298.1689	Fe I
30	2300.1418	Fe I
60	2327.3958	Fe II
60	2331.3084	Fe II
200	2332.7990	Fe II
120	2338.0065	Fe II
400	2343.4951	Fe II
50	2343.9610	Fe II
90	2344.2816	Fe II
120	2348.1159	Fe II
150	2348.3025	Fe II
120	2359.1322	Fe II
90	2359.9997	Fe II
70	2360.2945	Fe II
40	2363.8612	Fe II
120	2364.8281	Fe II
50	2365.7654	Fe II
50	2368.5964	Fe II
50	2369.9534	Fe II
40	2373.6245	Fe I
60	2373.7357	Fe II
40	2375.1940	Fe II
70	2376.4294	Fe II
50	2379.2765	Fe II
70	2380.7616	Fe II
1000	2382.0376	Fe II
40	2383.2452	Fe II
200	2388.6289	Fe II
700	2395.6254	Fe II
200	2399.2413	Fe II
500	2404.8858	Fe II
150	2406.6612	Fe II
50	2406.9761	Fe II
200	2410.5192	Fe II

Intensity	Air Wavelength (Å)	Spectrum
120	2411.0677	Fe II
90	2413.3104	Fe II
50	2417.8707	Fe II
40	2422.6882	Fe II
90	2424.1456	Fe II
70	2428.3638	Fe II
70	2430.0783	Fe II
50	2432.2612	Fe II
40	2432.8732	Fe II
90	2439.3014	Fe II
40	2443.7100	Fe II
60	2444.5154	Fe II
60	2445.5732	Fe II
150	2457.5891	Fe I
90	2458.7838	Fe II
40	2460.4404	Fe II
50	2461.2835	Fe II
60	2461.8610	Fe II
150	2462.6472	Fe I
80	2465.1492	Fe I
40	2466.6713	Fe II
40	2466.8194	Fe II
60	2468.8799	Fe I
40	2469.5147	Fe II
50	2470.6694	Fe II
80	2472.3320	Fe I
100	2472.8713	Fe I
60	2474.8145	Fe I
40	2478.5722	Fe II
120	2479.7764	Fe I
60	2480.1577	Fe II
50	2482.1172	Fe II
60	2482.6577	Fe II
1000	2483.2708	Fe I
30	2483.5334	Fe I

FIGURE A.7: First and second lists of strong iron emission lines. Taken from [37]

Intensity	Air Wavelength (Å)	Spectrum
100	2484.1875	Fe I
40	2484.2446	Fe II
80	2486.3728	Fe I
600	2488.1426	Fe I
50	2489.4833	Fe II
100	2489.7524	Fe I
500	2490.6443	Fe I
40	2490.8584	Fe II
200	2491.1550	Fe I
60	2491.3965	Fe II
60	2493.1846	Fe II
300	2493.2637	Fe II
60	2496.5337	Fe I
100	2501.1318	Fe I
40	2502.3930	Fe II
40	2503.8745	Fe II
50	2506.0935	Fe II
50	2507.9004	Fe I
100	2510.8350	Fe I
70	2511.7603	Fe II
40	2512.3650	Fe I
30	2517.6611	Fe I
80	2518.1018	Fe I
40	2519.0472	Fe II
400	2522.8494	Fe I
50	2524.2925	Fe I
120	2525.3879	Fe II
200	2526.2939	Fe II
200	2527.4351	Fe I
80	2529.1350	Fe I
70	2533.6274	Fe II
60	2534.4186	Fe II
70	2535.4856	Fe II
40	2535.6069	Fe I

Intensity	Air Wavelength (Å)	Spectrum
40	2536.6726	Fe II
120	2536.80	Fe II
60	2538.7987	Fe II
60	2538.9094	Fe II
90	2538.99	Fe II
120	2540.66	Fe II
60	2540.9722	Fe I
50	2541.1010	Fe II
40	2541.8358	Fe II
30	2542.1013	Fe I
40	2543.3781	Fe II
80	2545.9785	Fe I
50	2546.6701	Fe II
60	2548.7442	Fe II
50	2549.0833	Fe II
50	2549.3947	Fe II
40	2549.4616	Fe II
60	2549.6133	Fe I
40	2550.0274	Fe II
30	2550.6832	Fe II
250	2562.5356	Fe II
120	2563.4755	Fe II
40	2566.9126	Fe II
90	2574.3662	Fe II
30	2576.6902	Fe I
40	2577.9219	Fe II
60	2582.5832	Fe II
150	2584.5359	Fe I
300	2585.8758	Fe II
60	2591.5428	Fe II
400	2598.3692	Fe II
700	2599.3956	Fe II
30	2599.5669	Fe I
200	2606.5162	Fe II

FIGURE A.8: Third and fourth lists of strong iron emission lines. Taken from [37]

Intensity	Air Wavelength (Å)	Spectrum
80	2606.8264	Fe I
300	2607.0871	Fe II
400	2611.8736	Fe II
200	2613.8243	Fe II
200	2617.6174	Fe II
60	2620.41	Fe II
40	2623.5339	Fe I
120	2625.6671	Fe II
90	2628.2931	Fe II
150	2631.0471	Fe II
150	2631.3232	Fe II
30	2635.8088	Fe I
40	2664.6638	Fe II
30	2666.8125	Fe I
60	2679.0242	Fe I
300	2684.7536	Fe II
40	2689.2122	Fe I
40	2692.6019	Fe II
40	2703.9891	Fe II
40	2706.5820	Fe I
50	2714.4129	Fe II
400	2719.0273	Fe I
150	2720.9023	Fe I
40	2723.5774	Fe I
50	2727.5392	Fe II
50	2728.90	Fe II
100	2733.5806	Fe I
50	2735.4753	Fe I
50	2737.3091	Fe I
400	2739.5474	Fe II
80	2742.4053	Fe I
120	2743.1969	Fe II
200	2746.4838	Fe II

Intensity	Air Wavelength (Å)	Spectrum
400	2749.3216	Fe II
60	2749.4860	Fe II
120	2750.1406	Fe I
50	2753.2877	Fe II
500	2755.7365	Fe II
100	2761.81	Fe II
30	2772.0740	Fe I
60	2778.2202	Fe I
300	2788.1047	Fe I
40	2804.5203	Fe I
150	2806.9841	Fe I
250	2813.2864	Fe I
30	2823.2756	Fe I
60	2825.5557	Fe I
150	2832.4355	Fe I
20	2838.1194	Fe I
100	2843.9763	Fe I
80	2851.7969	Fe I
120	2936.9033	Fe I
100	2947.8760	Fe I
60	2953.9399	Fe I
150	2966.8982	Fe I
80	2970.0994	Fe I
120	2973.1323	Fe I
50	2973.2354	Fe I
60	2981.4451	Fe I
100	2983.5696	Fe I
100	2994.4268	Fe I
50	2999.5117	Fe I
80	3000.9478	Fe I
50	3008.1382	Fe I
40	3020.01	Fe II
50	3020.4907	Fe I
150	3020.6389	Fe I
60	3021.0728	Fe I

FIGURE A.9: FIfth and sixth lists of strong iron emission lines. Taken from [37]

Intensity	Air Wavelength (Å)	Spectrum
50	3024.0327	Fe I
50	3025.8423	Fe I
80	3037.3887	Fe I
80	3047.6045	Fe I
60	3057.4458	Fe I
100	3059.0857	Fe I
50	3193.2258	Fe I
80	3193.2998	Fe I
30	3222.0591	Fe I
60	3225.7871	Fe I
30	3236.2224	Fe I
40	3355.2278	Fe I
50	3407.4597	Fe I
50	3427.1194	Fe I
400	3440.6060	Fe I
250	3440.9888	Fe I
100	3443.8765	Fe I
120	3465.8606	Fe I
200	3475.4502	Fe I
50	3476.7019	Fe I
250	3490.5740	Fe I
50	3497.8406	Fe I
30	3521.2612	Fe I
40	3526.0408	Fe I
30	3541.0833	Fe I
40	3554.9246	Fe I
40	3558.5151	Fe I
100	3565.3789	Fe I
120	3570.0977	Fe I
80	3570.2542	Fe I
600	3581.1931	Fe I
30	3585.3188	Fe I

Intensity	Air Wavelength (Å)	Spectrum
40	3586.9849	Fe I
50	3606.6794	Fe I
150	3608.8594	Fe I
150	3618.7678	Fe I
120	3631.4631	Fe I
150	3647.8428	Fe I
150	3679.9133	Fe I
50	3687.4568	Fe I
120	3705.5659	Fe I
30	3707.9199	Fe I
60	3709.2463	Fe I
600	3719.9348	Fe I
150	3722.5630	Fe I
50	3727.6189	Fe I
120	3733.3176	Fe I
700	3734.8638	Fe I
600	3737.1316	Fe I
40	3743.3621	Fe I
600	3745.5613	Fe I
120	3745.8994	Fe I
300	3748.2622	Fe I
400	3749.4854	Fe I
300	3758.2329	Fe I
40	3760.0498	Fe I
150	3763.7891	Fe I
40	3765.5388	Fe I
60	3767.1919	Fe I
40	3795.0022	Fe I
40	3799.5476	Fe I
60	3812.9646	Fe I
150	3815.8403	Fe I
500	3820.4253	Fe I
250	3824.4436	Fe I
150	3825.8811	Fe I

FIGURE A.10: Seventh and eighth lists of strong iron emission lines. Taken from [37]

Intensity	Air Wavelength (Å)	Spectrum
120	3827.8225	Fe I
100	3834.2224	Fe I
50	3840.4375	Fe I
80	3841.0481	Fe I
250	3856.3716	Fe I
500	3859.9114	Fe I
150	3878.5732	Fe I
300	3886.2822	Fe I
30	3888.5134	Fe I
80	3895.6565	Fe I
120	3899.7075	Fe I
40	3902.9458	Fe I
60	3920.2581	Fe I
120	3922.9119	Fe I
120	3927.9199	Fe I
200	3930.2966	Fe I
40	4005.2419	Fe I
300	4045.8125	Fe I
150	4063.5942	Fe I
120	4071.7380	Fe I
40	4132.0581	Fe I
80	4143.8682	Fe I
30	4202.0293	Fe I
40	4216.1836	Fe I
30	4250.7871	Fe I
80	4260.4746	Fe I
120	4271.7607	Fe I
120	4282.4028	Fe I
120	4307.9023	Fe I
150	4325.7622	Fe I
80	4375.9302	Fe I
200	4383.5449	Fe I
120	4404.7505	Fe I
30	4415.1226	Fe I
60	4427.2979	Fe I

Intensity	Air Wavelength (Å)	Spectrum
40	4461.6528	Fe I
50	4920.5029	Fe I
150	4957.5967	Fe I
250	5167.4883	Fe I
50	5171.5962	Fe I
100	5227.1509	Fe I
120	5269.5376	Fe I
80	5270.3564	Fe I
80	5328.0386	Fe I
30	5328.5317	Fe I
50	5341.0239	Fe I
40	5371.4897	Fe I
30	5397.1279	Fe I
50	6247.56	Fe II
120	6456.38	Fe II

FIGURE A.11: Ninth and tenth lists of strong iron emission lines. Taken from [37]

Intensity	Air Wavelength (Å)	Spectrum
20	3955.85	N II
50	3995.00	N II
30	4041.31	N II
20	4241.78	N II
30	4447.03	N II
30	4601.48	N II
20	4607.16	N II
20	4621.39	N II
40	4630.54	N II
30	4643.08	N II
20	4803.29	N II
80	4963.98	N I
20	4994.36	N II
30	5001.48	N II
40	5005.15	N II
30	5007.32	N II
20	5010.62	N II
30	5045.10	N II
30	5666.63	N II
30	5676.02	N II
40	5679.56	N II
20	5686.21	N II
20	5710.77	N II
150	5752.50	N I
30	5931.78	N II
30	5941.65	N II
40	6482.05	N II
90	6482.70	N I
40	6610.56	N II
150	7423.64	N I
200	7442.29	N I
200	7468.31	N I
90	8184.87	N I
90	8188.02	N I
140	8216.34	N I
90	8223.14	N I
90	8242.39	N I
30	8438.74	N II

FIGURE A.12: List of strong nitrogen emission lines. Taken from [37]

Intensity	Air Wavelength (Å)	Spectrum
250	2445.538	O II
250	2733.289	O II
90	2972.29	O I
400	3134.720	O II
250	3138.335	O II
300	3287.472	O II
250	3390.209	O II
250	3470.676	O II
250	3727.320	O II
300	3749.486	O II
400	3911.957	O II
60	3947.29	O I
50	3947.48	O I
50	3947.59	O I
400	3973.2562	O II
200	3982.7140	O II
250	4072.157	O II
400	4075.862	O II
250	4119.215	O II
250	4185.449	O II
400	4189.789	O II
250	4317.138	O II
250	4349.426	O II
400	4414.905	O II
250	4416.974	O II
300	4590.972	O II
250	4596.175	O II
300	4641.810	O II
400	4649.135	O II
300	4661.633	O II
250	4676.235	O II
250	4705.352	O II

FIGURE A.13: List of strong oxygen emission lines. Taken from [37]

A.2.2 Strong Lines from Contaminants and Glue

The selection of possible contaminants that are glued to the metal surface consist of cesium, potassium, and iodine. The lists of strong cesium emission lines are the same as those of Figures A.4 and A.5. The list of strong iodine emission lines are in Figure A.6. The hydrogen lines are in Figure A.14, the potassium lines are in Figure A.15, and the silicon lines are in Figure A.16.

Intensity	Air Wavelength (Å)	Spectrum
5	3835.384	H I
6	3889.049	H I
8	3970.072	H I
15	4101.74	H I
30	4340.462	H I
30	4861.2786	H I
10	4861.2870	H I
60	4861.3615	H I

FIGURE A.14: Strong lines of hydrogen that may appear in the spectrum. hydrogen is contained in the glue. Taken from [37]

Intensity	Air Wavelength (Å)	Spectrum	Reference
200	2190.00	K II	D26
200	2550.02	K II	D26
	2992.12	K I	R56
	2992.22	K I	R56
	3034.76	K I	R56
	3034.92	K I	R56
150	3101.79	K I	R56
120	3102.04	K I	R56
200	3105.00	K II	D26
300	3217.16	K I	R56
250	3217.62	K I	R56
250	3440.05	K II	D26
400	3446.37	K I	R56
400	3447.38	K I	R56
250	3530.75	K II	D26
200	3618.49	K II	D26
120	3648.84	K I	R56
150	3648.98	K I	R56
200	3681.54	K II	D26
200	3816.56	K II	D26
250	3817.50	K II	D26
250	3897.92	K II	D26
250	4001.24	K II	D26
700	4044.14	K I	R56
700	4047.21	K I	R56
250	4134.72	K II	D26
250	4149.19	K II	D26
250	4186.24	K II	D26
250	4222.97	K II	D26
250	4225.67	K II	D26
250	4263.40	K II	D26
250	4305.00	K II	D26
250	4309.10	K II	D26
250	4388.16	K II	D26
250	4608.45	K II	D26
400	4641.88	K I	R56
400	4642.37	K I	R56
150	4740.91	K I	R56
250	4744.35	K I	R56
200	4753.93	K I	R56
300	4757.39	K I	R56
200	4786.49	K I	R56
300	4791.05	K I	R56
250	4799.75	K I	R56
300	4804.35	K I	R56
300	4829.23	K II	D26
300	4849.86	K I	R56
300	4856.09	K I	R56
300	4863.48	K I	R56
400	4869.76	K I	R56
300	4942.02	K I	R56
400	4950.82	K I	R56
400	4956.15	K I	R56
400	4965.03	K I	R56
250	5005.60	K II	D26
250	5056.27	K II	D26
400	5084.23	K I	R56
400	5097.17	K I	R56
400	5099.20	K I	R56
500	5112.25	K I	R56
500	5323.28	K I	R56
500	5339.69	K I	R56
500	5342.97	K I	R56
600	5359.57	K I	R56

FIGURE A.15: Strong lines of potassium that may appear in the spectrum produced by some plasma torch experiments. Taken from [37]

Intensity	Air Wavelength (Å)	Spectrum
600	2058.1323	Si I
20	2072.016	Si II
30	2072.701	Si II
400	2207.978	Si I
500	2210.894	Si I
300	2211.744	Si I
500	2216.669	Si I
400	2218.057	Si I
300	2435.154	Si I
400	2506.897	Si I
400	2514.316	Si I
500	2516.112	Si I
400	2519.202	Si I
400	2524.108	Si I
400	2528.509	Si I
200	2631.282	Si I
1000	2881.5771	Si I
50	2904.283	Si II
80	2905.692	Si II
150	2987.645	Si I
15	3053.184	Si II
15	3188.97	Si II
15	3193.09	Si II
7	3199.514	Si II
20	3203.872	Si II
30	3210.020	Si II
20	3333.139	Si II
30	3339.819	Si II
100	3856.017	Si II
40	3862.595	Si II
200	3905.523	Si I
50	4128.067	Si II
70	4130.893	Si II
20	4621.721	Si II
130	5041.026	Si II
130	5055.981	Si II
25	5192.86	Si II
70	5202.41	Si II
70	5466.432	Si II
70	5466.868	Si II

FIGURE A.16: Strong lines of silicon that may appear in the spectrum. Silicon is contained in the glue. Taken from [37]

Appendix B

Sample Construction of Saha Plot

This section focuses on the construction of a Saha Plot along with its uncertianty analysis. From the Materials and Methods chapter,

$$\ln\left(\frac{I_{ki}\lambda}{Ag_{ki}}\right) = -\frac{E_i}{k_B T} + b \tag{B.1}$$

where I_{ki} is the intensity of emission line from state i to state k, λ is the emission wavelength, Ag_{ki} is the transition probability, E_i is the excited state temperature, k_B is Boltzmann's constant, and T is the temperature. The intercept b is expressed in equation B.2. Plotting $\ln\left(\frac{I_{ki}\lambda}{Ag_{ki}}\right)$ vs E_i produces a Saha plot [69].

The expected intercept b of the Saha plot is expressed in Equation B.2.

$$b = \log\left(\frac{hcLn}{4\pi Z(T)}\right) \tag{B.2}$$

Constants $\frac{4\pi}{hc}$ are known, L is the width of the emission source, N is the density of the plasma, and $Z(T)$ is a function of temperature which is approximately equal to 1. The value of the intercept b can be used to estimate the density of the plasma.

B.1 Identification of Emission lines from Spectral Data

Peaks are identified from the raw spectral data as pairs of wavelength and intensity values. The intensity values are always positive integers. Figure B.1 is a scatter

plot of the data. Intensity is reported interchangeably in arbitrary units (A.U.) or counts, because of the averaging and subsequent rounding performed before the intensity values are recorded.

Peak emission line intensity values are the maximum intensity value found in the spectral peak. For instance, in Figure B.1, for the peak plotted between 751.1 nm to 752.3 nm, the peak intensitiy is given a value of 46 at wavelength value 751.7 nm.

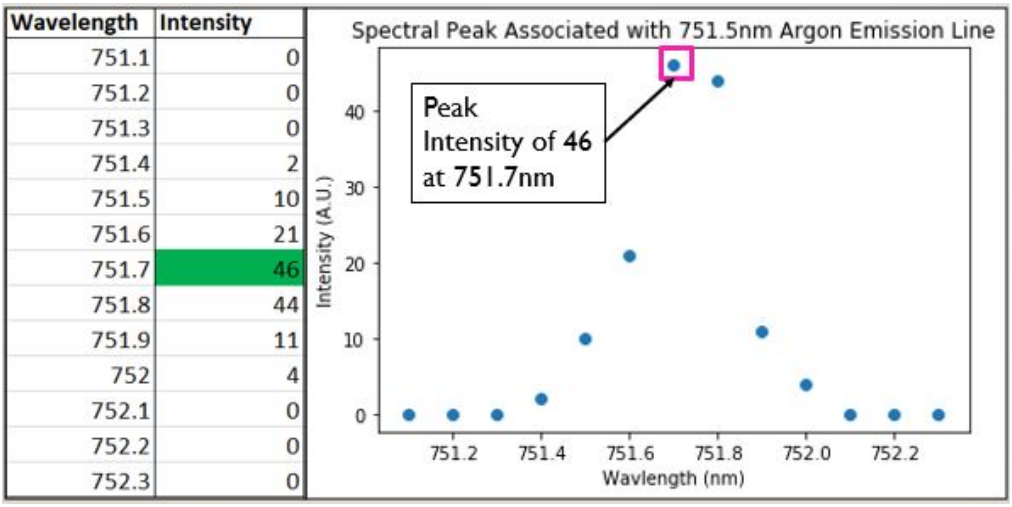

Wavelength	Intensity
751.1	0
751.2	0
751.3	0
751.4	2
751.5	10
751.6	21
751.7	46
751.8	44
751.9	11
752	4
752.1	0
752.2	0
752.3	0

FIGURE B.1: Identification of peak wavelength and intensity from scatter plot. Scatter plot produced from monochromator spectral data.

Using the knowledge that the monochromator has a shift in wavelength, the emission lines are identified by matching peak intensity and wavelength pairs to a list of argon emission lines such as those in Appendix A. The predicted "relative intensity" of lines provided by the NIST database [37] help identify the correct emission line as well. If there are many emission lines in the same wavelength region, but one has a predicted intensity much larger than the others, then that line is chosen.

If multiple emission lines match the peak and habe similar wavelengths (within ~ 0.3 nm, then those lines are not used in the Saha plot.

For an entire spectral data set, this process of identifying and rejecting emission lines is repeated.

Spectral datasets are scans of intensity as a function of wavelength for wavelength ranges of $\sim 695\,\text{nm}$ to $\sim 969\,\text{nm}$ as those are the regions where the monochromator setup is capable of measuring argon emission lines.

B.2 Data Tabulation

In order to produce Saha plots, the emission lines were placed in a table of their wavelength, emission probability (and respective uncertainty), and excited state energy value. Emission line information is accessible via the NIST database[37].

Table B.1 features the table of identified emission lines and their relevant information for Saha plots. In this example, two entries in the table were rejected due to there being multiple strong emission lines in the wavelength region of the peak.

Intensity of Peak (a.u.)	Monochromator Wavelength (nm)	Associated Argon Line Wavelength (nm)	Emission Probability (s-1)	Emission Probability Uncertainty grade	Emission Probability Relative Uncertainty	Excited State Energy (eV)
16	696.9	696.5431	19000000	B+	7%	13.32785693
5	707.1	706.7218	19000000	B	10%	13.30222736
53	738.7	738.398	42000000	B	10%	13.30222736
33	750.6	750.3869	45000000	B	10%	13.4798867
46	751.7	751.4652	40000000	B	10%	13.27303799
820	763.9	763.5106	122000000	B	10%	13.17177759
146	772.8	Multiple	Multiple	Multiple		
77	795.1	794.8176	55800000	B	10%	13.28263891
15	800.8	800.6157	24000000	C+	18%	13.17177759
103	801.7	801.4786	46000000	B	10%	13.09487245
235	810.7	Multiple	Multiple	Multiple		
1444	811.9	811.5311	230000000	B	10%	13.0757156
24	826.8	826.4522	45900000	B+	7%	13.32785693
215	841.1	840.821	112000000	B+	7%	13.30222736
401	842.8	842.4648	108000000	B+	7%	13.09487245
16	852.4	852.1442	41700000	B	10%	13.28263891
332	912.7	912.2967	56700000	B	10%	12.90701519
4	922.8	922.4499	25000000	B	10%	13.17177759
1	966.1	965.7786	16000000	B	10%	12.90701519

TABLE B.1: Table of Intensity and emission line data from pure argon plasma experiment (480 W input power) used to build Saha plot.

B.3 Uncertainty Analyses

The Saha plots were created using weighted linear fits. Weighted linear fits (Least Squares Method using Curve Fitting package from Python) take into account the

uncertainty of data points when calculating the optimal fit function. To perform a weighted linear fit, an uncertainty analysis needs to be performed for equation B.1. For the sake of brevity, let the left-hand-side of Equation B.1 be referred to as Y:

$$Y = \ln\left(\frac{I_{ki}\lambda}{Ag_{ki}}\right) \tag{B.3}$$

There are three possible sources of uncertainty in Y: uncertainties in intensity I_{ki}, emission line wavelength λ, and uncertainty in the transition probability Ag_{ki}.

B.3.1 Uncertainties in Intensity

A single measurement of peak intensity I performed by the DK-480 monochromator, $\sigma_{I_{ki},1}$ is expressed in Equation B.4.

$$\sigma_{I_{ki},1} = \sqrt{I_{ki}} \tag{B.4}$$

The monochromator is set to average over 200 measurements, after which it rounds to the nearest integer of counts. For n measurements, the error in intensity value is expressed in Equation B.5.

$$\sigma_{I_{ki},n} = \sigma_{I_{ki}} = \frac{\sigma_{I_{ki},1}}{\sqrt{n}} + 0.5 \tag{B.5}$$

The additional 0.5 to the error term is due to monochromator intensity data being rounded to the nearest integer.

B.3.2 Uncertainty in Wavelength

The relative uncertainties in λ, is on the order of one part per million for the emission lines used. These uncertainties are negligible in comparison to those uncertainties in intensity and emission probability. As a result, the uncertainty in emission line wavelength is omitted from the analysis.

B.3.3 Uncertainty in Transition Probability

The relative uncertainties for the emission probability Ag_{ki} are directly obtained from the letter grades associated with each emission line. This guide is shown in Table B.2.

Uncertainties in A_{ki}	
AAA	≤ 0.3%
AA	≤ 1%
A+	≤ 2%
A	≤ 3%
B+	≤ 7%
B	≤ 10%
C+	≤ 18%
C	≤ 25%
D+	≤ 40%
D	≤ 50%
E	> 50%.

TABLE B.2: Letter grade chart associated with uncertainty in emission line transition probability Ag_{ki}.

The letter grades provide an upper bound for the uncertainty. The upper bound is always used, so the uncertainty in Y will always be over-estimated to some extent.

B.3.4 Uncertainties in Excited State Energy

The uncertainties in excited state energy E_i (right hand side of Equation B.1 are described by the NIST database [37] to be the last decimal place of the recorded value. In many cases, the excited state energies are known to six or seven decimal places, making their relative uncertainty negligible in comparison to the other

sources of uncertainty. As a result, the uncertainty in Excited State Energy is omitted from the analysis. As a note, Boltzmann's constant k_B is defined to have an exact value and therefore has no uncertainty.

B.3.5 Total Uncertainty

The total uncertainty in Y can be expressed as the following:

$$\sigma_Y = \sqrt{\left(\frac{\partial Y}{\partial I_{ki}}\sigma_{I_{ki}}\right)^2 + \left(\frac{\partial Y}{\partial \lambda}\sigma_\lambda\right)^2 + \left(\frac{\partial Y}{\partial (Ag_{ki})}\sigma_{Ag_{ki}}\right)^2} \tag{B.6}$$

where $\sigma_{I_{ki}}$, σ_λ and $\sigma_{Ag_{ki}}$ are the respective uncertainties in intensity, wavelength, and transition probability.

Solving, and performing some simplifications, the expression for σ_Y is obtained in equation B.7.

$$\sigma_Y = \sqrt{\left(\frac{\sigma_{I_{ki}}}{I_{ki}}\right)^2 + \left(\frac{\sigma_\lambda}{\lambda}\right)^2 + \left(\frac{\sigma_{Ag_{ki}}}{Ag_{ki}}\right)^2} \tag{B.7}$$

All three terms in the radical are the relative uncertainties of each of I_{ki}, λ, and Ag_{ki} respectively.

B.4 Saha Plot with Trendline

Calculating $\ln\left(\frac{I_{ki}\lambda}{Ag_{ki}}\right)$ and E_i from the values from Figure B.1, a Saha Plot can be produced by plotting the former as a function of the latter. Using a weighted linear fit from the Python "Curve Fitting" package, a trend line can be generated that provides a slope and intercept with uncertainties for each. A Saha plot with trend-line is shown in Figure B.2. Note how the outlier boxed in pink is not strongly counted towards the trend line.

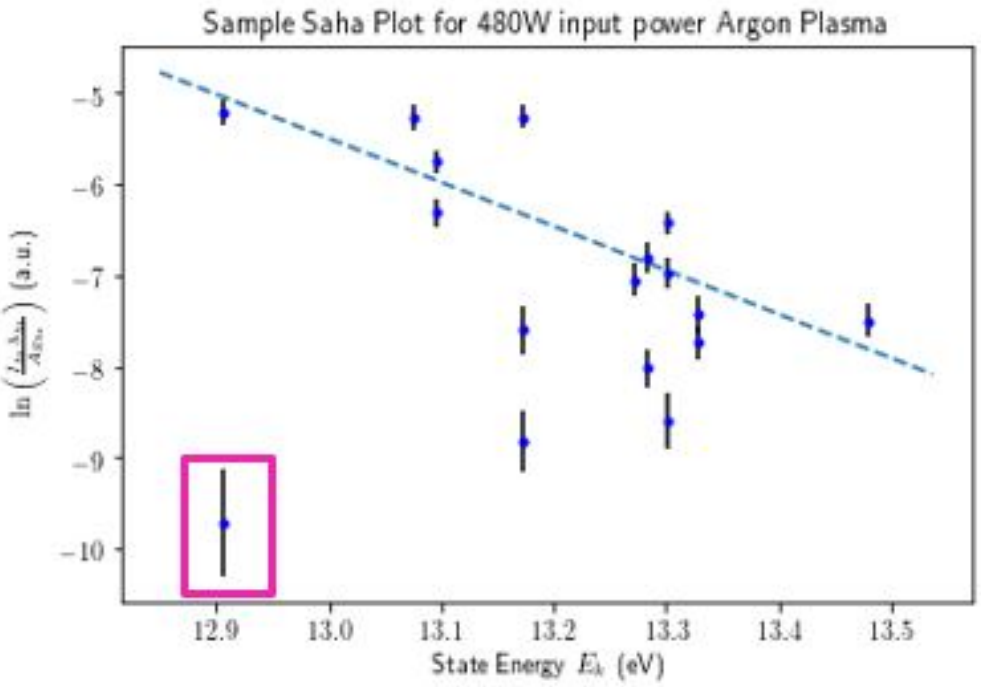

FIGURE B.2: Sample Saha plot with fitted line.

B.5 Solving for Temperature

The temperature can be found from the parameters provided from the trend line. The slope m of the trendline is a function of the temperature:

$$m = -\frac{1}{k_B T}, \tag{B.8}$$

The temperature can be solved for by rearranging:

$$T = -\frac{1}{k_B m}. \tag{B.9}$$

From this, the uncertainty in Temperature may be calculated:

$$\sigma_T = \sqrt{\left(\frac{\partial T}{\partial m}\sigma_m\right)^2} = \frac{\sigma_m}{m^2 k_B}. \tag{B.10}$$

The uncertainty in temperature is directly calculable from the error in slope m, σ_m. The weighted fit provides a value for σ_m.

B.6 Estimation of Plasma Density

The density of the plasma can be estimated by solving equation B.2 for the density:

$$N = \frac{4\pi}{hcl} \exp b \tag{B.11}$$

If the intercept b is known to have some uncertainty σ_b from the trendline, then the uncertainty in the density can be solved for:

$$\sigma_N = \frac{4\pi \exp(b)}{hcl} \sigma_b = N\sigma_b \tag{B.12}$$

This value is an estimation as the uncertainty in N.

Appendix C

Analysis of Coolant Flow

C.1 Outline

As discussed in the Materials and Methods section, there are three microwave components that receive coolant: the microwave head, the chilled water load, and the isolator heat sink. The flow rates of coolant to the isolator heat sink and chilled water load are monitored. The microwave head must have some minimum amount of coolant flow in order to ensure that its temperature stays above its maximum specified temperature of 40 °C, as the magnetron continuously produces waste heat. The flow rate to the magnetron is not monitored by flow meters, but an internal sensor inside the magnetron head will halt microwave output if coolant flow is insufficient.

The minimum flow rate of the coolant may now be estimated pending certain other knowns and assumptions:

- The coolant density and heat capacity are equivalent to those of water
- The coolant heat capacity does not change significantly over the temperature range used.
- All reflected microwave power is transferred to the isolator heat sink.
- The isolator outlet temperature reaches a maximum value of 40 °C.

The coolant is a nitrite solution, according to University Facilities. Solutions in water tend to change the heat capacity, but the first assumption is reasonable

for this analysis. Similar reasoning applies to the second assumption. The third assumption is non-conservative, but if the estimated minimum flow rate is exceeded by a large margin, this assumption may be treated as reasonable for this work. The fourth assumption simply constrains that the coolant cannot exceed the maximum temperature of the magnetron. This assumption is conservative.

Based on these assumptions, the heat transfer calculations to verify the minimum required coolant for the magnetron can be based on the following knowns:

- The maximum output of the magnetron is 2000 W. This is stated in the magnetron manual.
- The coolant inlet temperature of the magnetron is 9 °C. The coolant at its source has consistently been measured to be 9 °C without significant (10%) deviations.

With a constant inlet temperature, the heat transferred from the magnetron to the coolant will result in a change in temperature of the coolant channel outlet. The outlet channel coolant velocity is not expected to vary significantly due to the coolant system being under pressure. There are two other methods of possible heat transfer: conduction of heat from the chilled water load to other components, and thermal radiation. These are assumed to be negligible.

With these assumptions and knowns, the heat transfer rate from the magnetron component to the coolant can be estimated by Equation C.1

$$\dot{Q} = \rho \dot{V} C \Delta T \tag{C.1}$$

In this case, the $\dot{V}$ term would be the minimum value of the flow rate needed to carry the maximum possible microwave output value of $\dot{Q} = 2000W$ while staying at or below 40 C. This would suggest a temperature difference $\Delta T = 40 - 9 = 31C$.

Solving for $\dot{V}$ in Equation C.2

$$\dot{V} = \frac{\dot{Q}}{\rho C \Delta T} \tag{C.2}$$

Where ρ is the density of the coolant, and C is its heat capacity. Solving for $\dot{V}$ using the density and heat capacity of water at 20 °C, a value of $0.92\frac{L}{min}$ is obtained. The coolant system outputs a flow rate of around $1.5\frac{L}{min}$ litres per minute to the magnetron, giving a margin of around 60%.

Appendix D

Outline of Power Coupler Calibration Methods

This Appendix describes the methods used to re-calibrate the microwave power couplers as seen in Chapter 3.

D.1 Motivation

The microwave systems display and monitor values for the input power were inaccurate. The monitors function by having a voltage signal sent to them by the power measurement box. The power measurement box interprets the signals sent to it by the power coupler. The voltage signal which the monitors display is specified to be proportional to the magnitude of microwave power that the couplers measure.

To re-calibrate the power couplers, an understanding of the physical power value represented by the voltage was needed.

When the chilled water load is heated, the outlet temperature of the coolant increases proportionately to the microwave power that is imparted the coolant channels ($P_{imparted}$) based on heat transfer calculations like those completed in Appendix C:

$$P_{imparted} = \rho \dot{V} C \Delta T, \tag{D.1}$$

where ρ is the density of the coolant, $\dot{V}$ is the volumetric flow rate of the coolant, and ΔT is the temperature increase between the inlet and the outlet of the chilled water load. In this case, the imparted power would be the difference between the forward ($P_{forward}$) and reflected power ($P_{reflected}$).

$$P_{imparted} = P_{forward} - P_{reflected}. \tag{D.2}$$

This assumes no losses due to conduction or radiation. Based on preliminary tests, it was found that the reflected power reported on the display was consistently displaying its minimum value: in this case, $3W$. As such, it was assumed that the reflected power was zero. With this assumption, it could then be assumed that the forward power $P_{forward}$ was equal to the microwave power produced by the magnetron.

This allows for each configuration to be calibrated by measuring different values of $P_{forward}$ by adjusting the input microwave power, keeping all the other connections the same. An increase in the input microwave power proportionately increases $P_{forward}$, which increases V. This relationship between the power represented by a monitor P and the monitor voltage V is linear according to the Power Supply manual. It is known that the monitors do not have sufficient input impedance, so this relationship may not be true.

The mapping of V to P for each connection configuration (Monitor 1 or Monitor 2) was done in two steps. Firstly the power on the display $P_{display}$ was mapped to monitor voltage V for input powers. This would demonstrate the relation between $P_{display}$ was mapped to monitor voltage V remained linear. Then, a mapping from true microwave power P to $P_{fwd,display}$ would be made. This is expected to be linear.

D.1.1 Mapping $P_{display}$ to V

The mapping of $P_{display}$ to V was done by following the following method:

1. Produce microwaves at multiplemicrowave power levels.
2. Record monitor voltage V and $P_{display}$ simultaneously

3. Plot points produced by $P_{fwd,display}$ and monitor voltage V.

The relation between $P_{display}$ and V was found to be linear, even though the input impedances of the voltmeters did not meet specification.

D.1.2 Mapping estimate of P to $P_{fwd,display}$

The mapping of the estimate of P to $P_{fwd,display}$ was not straightforward. The surface temperature of the chilled water inlet was taken as a proxy temperature for the temperature of the coolant that sits *inside the channel*. Recall that the coolant system remains under pressure. Initial trials involved the attempt to introduce a thermocouple inside the channel, but this caused unwanted coolant spills. The surface temperature of the chilled water load outlet pipe was used instead. The surface's temperature was measured with a thermocouple. This is shown in Figure D.1.

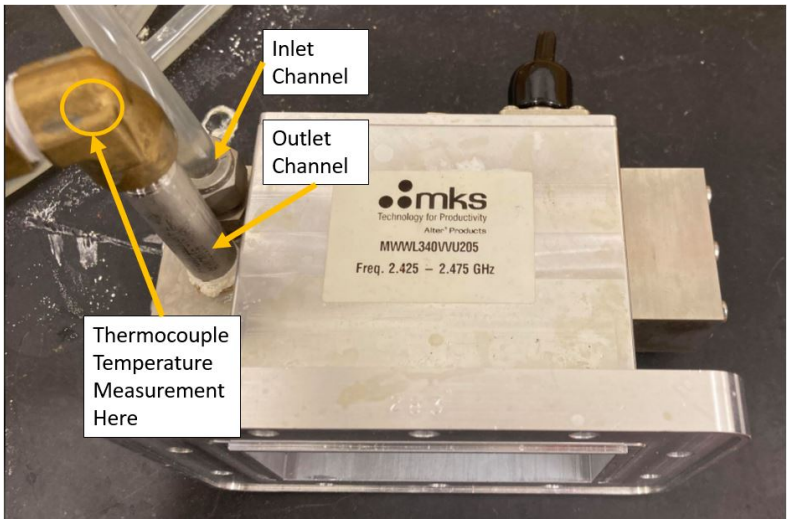

FIGURE D.1: Chilled water load. Inlet and outlet channels identified. Temperature measurement with thermocouple made at the bend of the outlet channel.

Using surface temperatures requires sufficient time has passed for steady state to be achieved with the channels/rubber hose that holds the coolant, and the coolant itself. For these calculations, the microwave power was left running for five

minutes. Once temperature measurement was started, tap water was added to the thermocouple tips in order to provide more thermal conductivity to the the region where temperature was being measured.

Thermocouples function by achieving the same temperature as the object whose temperature they measure so the addition of tap water would allow for equilibrium to be achieved at a faster rate. Ideally, thermal paste should have been used.

The mapping of P to $P_{fwd,display}$ was estimated in the following way:

1. Turn on and hold output microwave power constant for several minutes in order to allow outlet channel temperatures to stabilize.

2. Record the forward power and input microwave power.

3. Measure the surface temperature of the outlet channel of the chilled water load. Measure the average value over several minutes of continuous recording.

4. Calculate the true input power value using heat transfer method outlined in Appendix C: $\dot{Q} = P = \rho \dot{V} C \Delta T$

The mapping from P to $P_{fwd,display}$ was also found to be linear. Since the mappings of P to $P_{fwd,display}$ and $P_{fwd,display}$ to V are found to both be linear, the mappings can be combined to produce a linear relation between "true" microwave power P and monitor voltage V. The linear relation was determined using a least squared linear fit using the Python curve fitting package.

Bibliography

[1] Canadian Nuclear Safety Commission, *REGDOC 2.11.2 - Waste Management: Decommissioning*. 280 Slater St., Ottawa, Ontario, Canada: Canadian Nuclear Safety Commission, 2019.

[2] S. I. Kim, H. Y. Lee, and J. S. Song, "A study on characteristics and internal exposure evaluation of radioactive aerosols during pipe cutting in decommissioning of nuclear power plant," eng, *Nuclear engineering and technology*, vol. 50, no. 7, pp. 1088–1098, 2018, ISSN: 1738-5733.

[3] *Decommissioning of Nuclear Facilities*, Presentation, International Atomic Energy Agency, 2006.

[4] Shimada, Taro and Tanaka, Tadao, "Characterization on the radioactive aerosols dispersed during plasma arc cutting of radioactive metal piping," eng, *Journal of radioanalytical and nuclear chemistry*, vol. 303, no. 2, pp. 1345–1349, 2015, ISSN: 0236-5731.

[5] Nuclear Energy Agency, "Decontamination and Dismantling of Radioactive Concrete Structures," *NEA News*, vol. 42, 2011, ISSN: 1605-9581.

[6] Khurmi, R. and Carlisle, R. and Harvel, G., "Development of a Selection Tool for Choosing Decontamination Technology for Canadian Applications," International Conference on Nuclear Engineering 28, Aug. 2020, V003T12A043.

[7] J.L. Nelson and J.R. Divine, *Decontamination Processes for Restorative Operations and as a Precursor to Decommissioning: A Literature Review*. Pacific Northwest Laboratory, May 1981.

[8] *Radiological Characterization of Shut Down Nuclear Reactors for Decommissioning Purposes*, ser. Technical Reports Series 389. Vienna: International Atomic Energy Agency, 1998, ISBN: 92-0-103198-X.

[9] Personal correspondence with OPG Decommissioning Team. Summer of 2018.

[10] C. Grupen, *Introduction to radiation protection practical knowledge for handling radioactive sources*, eng. Berlin ; Springer, 2010, ISBN: 9783642025860.

[11] P. Kularni, "Aerosol measurement; principles, techniques, and applications, 3d ed," vol. 26, no. 4, 2011, ISSN: 0887-3763.

[12] S. D. Schery, *Understanding radioactive aerosols and their measurement*, ser. Environmental science and technology library ; v. 19. Dordrecht ; Kluwer Academic Publishers, 2001, ISBN: 0792370686.

[13] M. M. R. Williams, *Aerosol science : theory and practice : with special applications to the nuclear industry*, eng, 1st ed. -. Oxford: Pergamon Press, 1991, ISBN: 0080372090.

[14] N. Chae, M.-H. Lee, S. Choi, B. G. Park, and J.-S. Song, "Aerodynamic diameter and radioactivity distributions of radioactive aerosols from activated metals cutting for nuclear power plant decommissioning," *Journal of Hazardous Materials*, vol. 369, pp. 727 –745, 2019, ISSN: 0304-3894.

[15] M.-H. Lee, W. Yang, N. Chae, and S. Choi, "Performance assessment of HEPA filter against radioactive aerosols from metal cutting during nuclear decommissioning," eng, *Nuclear engineering and technology*, vol. 52, no. 5, pp. 1043–1050, 2020, ISSN: 1738-5733.

[16] H Leibold and J. Wilhelm, "Investigations into the penetration and pressure drop of HEPA filter media during loading with submicron particle aerosols at high concentrations," eng, *Journal of aerosol science*, vol. 22, S773–S776, 1991, ISSN: 0021-8502.

[17] G. Harvel, T. Sunagawa, and K. Yamamoto, "Recovery of radioactive iodine from nuclear power plants using a microwave based plasma technique," *International Journal of Plasma Environmental Science and Technology*, vol. 11, 122–127, 2018.

[18] P. M. Bellan, *Fundamentals of plasma physics*, eng. Cambridge, UK ; Cambridge University Press, 2006, ISBN: 0521821169.

[19] J. A. Bittencourt, *Fundamentals of plasma physics*, eng, 3rd ed. New York: Springer, 2004, ISBN: 0387209751.

[20] T. Beuthe, "Modelling of Ar-CO2 Thermal Plasma," Ph.D. dissertation, McMaster University, 1280 Main St W, Hamilton, Ontario, Canada, 1992.

[21] T. Kaneda, T. Kubota, and J.-S. Chang, "Plasma parameters in noble-gas narrow-tube and capillary-tube discharge, positive column plasmas," eng, *Journal of Physics D: Applied Physics*, vol. 23, no. 5, pp. 500–503, 1990, ISSN: 0022-3727.

[22] D. V. Schroeder, *An introduction to thermal physics*, eng. San Francisco, Calif: Addison-Wesley, 2000, ISBN: 0201380277.

[23] H Kikuchi, "EHD in dusty and dirty plasmas and in unconventional plasmas particularly involving discharge and ionization distinct from HD and MHD," eng, IEEE, 2003, p. 162, ISBN: 9780780379114.

[24] O. Niculescu, M. Agop, P. Nica, and D. G. Dimitriu, "Experimental investigations and theoretical study of the negative differential resistance in a discharge plasma," eng, IEEE, 2012, 1P–41–1P–41, ISBN: 9781457721274.

[25] *Tomahawk 375 Air*, User Manual for Tomahawk 375 Air, Lincoln Electric, 2012.

[26] R. Miotk, B. Hrycak, M. Jasinski, and J. Mizeraczyk, "Characterization of an atmospheric-pressure argon plasma generated by 915 mhz microwaves using optical emission spectroscopy," *Journal of spectroscopy (Hindawi)*, vol. 2017, pp. 1–6, 2017, ISSN: 2314-4920.

[27] V. Lisovskiy, V. Koval, E. Artushenko, and V. Yegorenkov, "Validating the Goldstein–Wehner law for the stratified positive column of dc discharge in an undergraduate laboratory," *European Journal of Physics*, vol. 33, pp. 1537–1545, Nov. 2012.

[28] G. G. Lister, "Low-pressure gas discharge modelling," eng, *Journal of Physics D: Applied Physics*, vol. 25, no. 12, pp. 1649–1680, 1992, ISSN: 0022-3727.

[29] V. Kolikov, *Powerful pulsed plasma generators : research and application*, eng, ser. Springer series on atomic, optical, and plasma physics, volume 101. Cham, Switzerland: Springer, 2018, ISBN: 9783319952499.

[30] S. Mohsenian, S. Sheth, S. Bhatta, D. Nagassou, D. Sullivan, and J. P. Trelles, "Design and characterization of an electromagnetic-resonant cavity microwave plasma reactor for atmospheric pressure carbon dioxide decomposition," *Plasma processes and polymers*, vol. 16, 2019, ISSN: 1612-8850.

[31] P. Brault and E. C. Neyts, "Cheminform abstract: Molecular dynamics simulations of supported metal nanocatalyst formation by plasma sputtering," eng, *ChemInform*, vol. 46, no. 40, no–no, 2015, ISSN: 0931-7597.

[32] J. P Trelles, C Chazelas, A Vardelle, and J. V. R Heberlein, "Arc plasma torch modeling," eng, *Journal of thermal spray technology*, vol. 18, no. 5-6, pp. 728–752, 2009, ISSN: 1544-1016.

[33] T. Engel, *Quantum chemistry and spectroscopy*, eng, 2nd ed. New York: Prentice Hall, 2010, ISBN: 0321615042.

[34] K. A. Rubinson, *Contemporary instrumental analysis*, eng. Upper Saddle River, NJ: Prentice Hall, 2000, ISBN: 0137907265.

[35] K. E. Evdokimov, M. E. Konischev, V. F. Pichugin, and Z. Sun, "Study of argon ions density and electron temperature and density in magnetron plasma by optical emission spectroscopy and collisional-radiative model," *Resource-Efficient Technologies*, vol. 3, no. 2, pp. 187 –193, 2017, ISSN: 2405-6537.

[36] M Nikolic, J Newton, C. I Sukenik, L Vuskovic, and S Popovic, "Measurements of population densities of metastable and resonant levels of argon using laser induced fluorescence," eng, *Journal of applied physics*, vol. 117, no. 2, pp. 23 304–, 2015, ISSN: 0021-8979.

[37] A. Kramida, Yu. Ralchenko, J. Reader, and NIST ASD Team, NIST Atomic Spectra Database (ver. 5.7.1), [Online]. National Institute of Standards and Technology, Gaithersburg, MD. 2019.

[38] D. D. Fitts, *Principles of quantum mechanics as applied to chemistry and chemical physics*, eng. New York: Cambridge University Press, 1999, ISBN: 0521651247.

[39] *Digikrom User Manual*, Spectral Products, 2009.

[40] S. Falcinelli, P. Candori, M. Bettoni, F. Pirani, and F. Vecchiocattivi, "Penning ionization electron spectroscopy of hydrogen sulfide by metastable helium and neon atoms," eng, *The journal of physical chemistry.*, vol. 118, no. 33, pp. 6501–6506, 2014, ISSN: 1089-5639.

[41] *CRC Handbook of Chemistry and Physics (Online)*, eng, Accessed Online, Boca Raton, Fla.

[42] T. Burghelea and V. Bertola, *Transport Phenomena in Complex Fluids*, eng, ser. CISM International Centre for Mechanical Sciences. Cham: Springer International Publishing AG, 2020, vol. 598, ISBN: 3030355578.

[43] S. Duhr and D. Braun, "Why molecules move along a temperature gradient," eng, *Proceedings of the National Academy of Sciences - PNAS*, vol. 103, no. 52, pp. 19 678–19 682, 2006, ISSN: 1091-6490.

[44] *SM845 Switching Power Supply With PFC Stage For 2KW Magnetron*, SM845, Manual of Magnetron Power Supply, MKS Instruments, 2017.

[45] *TMO-TMA 2,45GHz Magnetron Heads Closed Frame*, SM845, Manual for Magnetron, MKS Instruments, 2017.

[46] *F-400N Variable Area Flow Meters*, F-40377LN-6, Blue-White Flow Meter Specification Sheet, Blue-White Industries, Ltd., 2017.

[47] *Variable Area Flow Meter for Liquid Flow FL-10 Series*, FL-10G, Omega Flow Meter Specification Sheet. No dates given for specification sheet., OMEGA Engineering.

[48] J. D. Kim, S. H. Kim, H. J. Kim, S. W. Shin, J. J. Choi, and Y. H. Na, "Impedance measurement system for a microwave-induced plasma," eng, *Journal of the Korean Physical Society*, vol. 60, no. 6, pp. 907–911, 2012, ISSN: 0374-4884.

[49] *AG340 Manual 3 Stubs Tunerr*, AG340M3, Specification Sheet of Stub Tuner for Microwave System, MKS Instruments, 2015.

[50] R. Miotk, M. Jasinski, and J. Mizeraczyk, "Analysis of the tuning characteristics of microwave plasma source," *Physics of Plasmas*, vol. 23, no. 4, p. 043 507, 2016.

[51] Gerling Applied Engineering Inc., *GA2006-7 Brocure*, Online, Specification Sheet for GA2017 Tapered Microwave Adapter, 2012.

[52] *DC 2340 DC 1340 Directional Couplers*, DC 2340, Power Coupler Specification Sheet, MKS Instruments, 2014.

[53] *Alter RD8400 Linear Power Sensor*, RD8400, Specification Sheet of Power Sensor for Microwave System Power Couplers, MKS Instruments, 2015.

[54] N. Somer, *NDL-RCT-MAN-004: Spectroscopy Systems User Manual*, Internal document for Nuclear Design Laboratory, Nuclear Design Laboratory, 2019.

[55] *Wavelength Calibration Light Source*, 1.0, Ocean Optics, 8060 Bryan Dairy Road, Largo, FL 33777 USA, 2018.

[56] StellarNet Inc., *Fiber Optic Cables for UV-VIS-NIR*, Specification Sheet for StellarNet 400 micron cable. No dates given for the specification sheets., StellarNet Inc., 14390 Carlson Circle, Tampa, Florida, United States of America.

[57] *UV-Vis Optical Fibers Patch Cords*, ONLINE, No Specification Sheets Available Online, 2020.

[58] N. Somer, *NDL-RCT-PRO 003: Microwave Plasma System General Startup Procedure*, Internal document for Nuclear Design Laboratory, Nuclear Design Laboratory, 2018.

[59] N. Somer, *NDL-RCT-PRO-004: Microwave Plasma System General Shutdown Procedure*, Internal document for Nuclear Design Laboratory, Nuclear Design Laboratory, 2018.

[60] N. Somer, *NDL-MWP-PRO-005: High Voltage Power Supply Initial Startup Procedure*, Internal document for Nuclear Design Laboratory, Nuclear Design Laboratory, 2019.

[61] N. Somer, *NDL-MWP-PRO-006: Microwave System Low Power Testing Procedure*, Internal document for Nuclear Design Laboratory, Nuclear Design Laboratory, 2019.

[62] N. Somer, *NDL-RCT-PRO-005: Microwave Plasma System Power Coupler Calibration Procedure*, Internal document for Nuclear Design Laboratory, Nuclear Design Laboratory, 2018.

[63] N. Somer, *NDL-MWP-PRO-007: Low Power Plasma Testing Procedure*, Internal document for Nuclear Design Laboratory, Nuclear Design Laboratory, 2019.

[64] N. Somer, *NDL-RCT-PRO-009: Argon Plasma Jet Height Characterization Experiment*, Internal document for Nuclear Design Laboratory, Nuclear Design Laboratory, 2020.

[65] N. Somer, *NDL-RCT-PRO-010: Method of Measuring Argon Plasma Temperature Dependence on Input Power*, Internal document for Nuclear Design Laboratory, Nuclear Design Laboratory, 2020.

[66] N. Somer, *NDL-RCT-PRO-011: Determination of Contaminant Emission Lines when introduced into Argon Plasma*, Internal document for Nuclear Design Laboratory, Nuclear Design Laboratory, 2020.

[67] N. Somer, *NDL-RCT-PRO-013 R2: Arc Plasma Torch Spectral Acquisition Procedure*, Internal document for Nuclear Design Laboratory, Nuclear Design Laboratory, 2020.

[68] N. Somer, *NDL-RCT-PRO-014 R2: Manual Cutting of Mock-Contaminated Metal Sample with Air Plasma Torch*, Internal document for Nuclear Design Laboratory, Nuclear Design Laboratory, 2020.

[69] N. Ohno, M. Razzak, H. Ukai, S. Takamura, and Y. Uesugi, "Validity of electron temperature measurement by using boltzmann plot method in radio frequency inductive discharge in the atmospheric pressure range," *Plasma and Fusion Research*, vol. 1, pp. 28–028, Jan. 2006.

[70] B. N Sismanoglu, K. G Grigorov, R Caetano, M. V. Rezende, and Y. D Hoyer, "Spectroscopic measurements and electrical diagnostics of microhollow cathode discharges in argon flow at atmospheric pressure," *The European physical journal. D, Atomic, molecular, and optical physics*, vol. 60, no. 3, pp. 505–516, 2010, ISSN: 1434-6060.

[71] N. Somer, *NDL-RCT-PRO-008: Small Nested Quartz Glass Tube Construction Procedure*, Internal document for Nuclear Design Laboratory, Nuclear Design Laboratory, 2019.